

**IMAGING SINGLE FUSION EVENTS
AT THE PLASMA MEMBRANE
USING
TOTAL INTERNAL REFLECTION FLUORESCENCE
MICROSCOPY
—
APPLICATIONS IN MEMBRANE TRAFFIC**

Dissertation

zur Erlangung des Doktorgrades (Dr. rer. nat.) am
Fachbereich für Biologie, Chemie und Pharmazie der
Freien Universität Berlin

Durchgeführt im 'Laboratory for Cellular Biophysics'
Rockefeller University, New York

Jan Schmoranzer

New York, February 2002

Die vorliegende Arbeit wurde im "Laboratory for Cellular Biophysics" von Dr. Sanford M. Simon an der "Rockefeller University" in New York durchgeführt.

Große Teile dieser Arbeit sind/werden veröffentlicht:

- 1. Imaging Constitutive Exocytosis with Total Internal Reflection Fluorescence Microscopy**
Jan Schmoranzer, Mark Goulian, Dan Axelrod, Sanford M. Simon
J. Cell Biology 149(1):23-31, April 3, 2000
 - 2. Insulin-regulated Release from the Endosomal Recycling Compartment is Regulated by Budding of Specialized Vesicles**
Michael A. Lampson, Jan Schmoranzer, Anja Zeigerer, Sanford M. Simon, and Timothy E. McGraw
Molecular Biology of the Cell, 12(11):3489-501, Nov. 2001
 - 3. Role of Microtubules in Delivery and Fusion of Post-Golgi Transport Intermediates**
Jan Schmoranzer, Geri Kreitzer, Sanford M. Simon
Submitted (see Chapter 4)
 - 4. Targeted Exocytosis of Apical Proteins and Distribution Syntaxin 3 in Polarized Epithelial Cells Depend on Microtubules**
Geri Kreitzer, Jan Schmoranzer, Yunbo Gan, Seng Hui Low, Zhizhou Zhang, Thomas Weimbs, Sanford M Simon and Enrique Rodriguez-Boulan
In preparation (see Chapter 5)
-

Eingereicht zur Beurteilung am 18. Februar 2002.

1. Gutachter: Prof. Dr. Ralf Erdmann (FU Berlin)
 2. Gutachter: Prof. Dr. Sanford M. Simon (Rockefeller University)
-

Hiermit erkläre ich, daß ich diese Arbeit selbständig verfaßt und keine anderen als die angegebenen Quellen und Hilfsmittel verwendet habe.

New York, Februar 2002

Jan Schmoranzer

Table of Contents

1. INTRODUCTION	3
1.1. Why image constitutive exocytosis?	4
1.2. Total Internal Reflection Fluorescence Microscopy	5
1.3. Applying TIR-FM to study membrane traffic	7
2. TOTAL INTERNAL REFLECTION FLUORESCENCE MICROSCOPY	9
2.1 Theoretical background.....	9
2.2. Comparison of EPI- and TIR-illumination.....	11
2.3. 'Objective-type' versus 'Prism-type' TIR-FM.....	13
2.4. Objective-Type TIR-FM setup	16
2.5. Multi-color TIR-FM.....	17
3. IMAGING CONSTITUTIVE EXOCYTOSIS	25
3.1. Introduction.....	25
3.2. Results	27
4. ROLE OF MICROTUBULES IN POST-GOLGI TRAFFIC OF FIBROBLASTS.....	39
4.1. Introduction.....	39
4.2. Results	43
5. ROLE OF MICROTUBULES IN POST-GOLGI TRAFFIC OF POLARIZED EPITHELIAL CELLS	64
5.1. Introduction.....	64
5.2. Results	68
6. DISCUSSION.....	78
6.1. Quantitative detection of single fusion events during constitutive exocytosis	78
6.2. Structure of post-Golgi carriers	81
6.3. Mechanism of constitutive exocytosis	83
6.4. Domain-specific targeting of post-Golgi membrane cargo.....	90
6.5. Targeted delivery in migrating fibroblasts	91
6.6. Targeted delivery in polarized epithelial cells	93
6.7. Post-Golgi traffic in fibroblasts and epithelial cells – A similar mechanism ?	97
6.8. Imaging components of the fusion machinery	99
7. INSULIN-REGULATED RECYCLING OF THE GLUCOSETRANSPORTER	101

7.1. Introduction.....	101
7.2. Results	103
7.3. Discussion	109
8. MATERIALS AND METHODS	112
8.1. TIR-FM setup	112
8.2. Multi-color TIR-FM.....	115
8.3. Image acquisition	117
8.4. Cell culture	119
8.5. Chapter 3: Detection of single fusion events	119
8.6. Chapter 4: Post-Golgi traffic in fibroblasts	121
8.7. Chapter 5: Post-Golgi traffic in epithelial cells	125
8.8. Chapter 7: Insulin-regulated recycling.....	128
9. LIST OF VIDEOS.....	130
10. SUMMARY.....	135
11. ZUSAMMENFASSUNG	138
12. REFERENCE LIST	141
13. APPENDIX.....	153
13.1. Curriculum Vitae.....	153
13.2. Acknowledgements	155
13.3. Photo of multi-color TIR-FM system	157

1. Introduction

In eukaryotic cells, the biosynthetic secretory pathway enables the delivery of newly synthesized proteins, lipids and carbohydrates to the cell surface. The correct targeting of biosynthetic membrane proteins to the plasma membrane is essential for cell growth and homeostasis. The organelles that constitute this pathway include the endoplasmic reticulum (ER), the Golgi complex and the plasma membrane (Fig. 1.1). Secretory cargo is transported between these organelles in membrane-bounded vesicular or tubular intermediates along organized directional routes through the cytoplasm. The cargo is synthesized in the ER, then transported to the Golgi for further modification and maturation. After passing through the Golgi the cargo is sorted and packaged into post-Golgi transport intermediates (in short, carriers) at the *trans*-Golgi network (TGN). Finally, these carriers are transported to the periphery of the cell where they fuse with the plasma membrane. During fusion, they deliver their luminal content to the outside of the cell and their membrane cargo to the plasma membrane, a process called exocytosis. How proteins are sorted and packaged into transport intermediates at the Golgi/TGN, how they are transported to the plasma membrane and how they are made fusion competent have all been long-standing questions in cell biology.

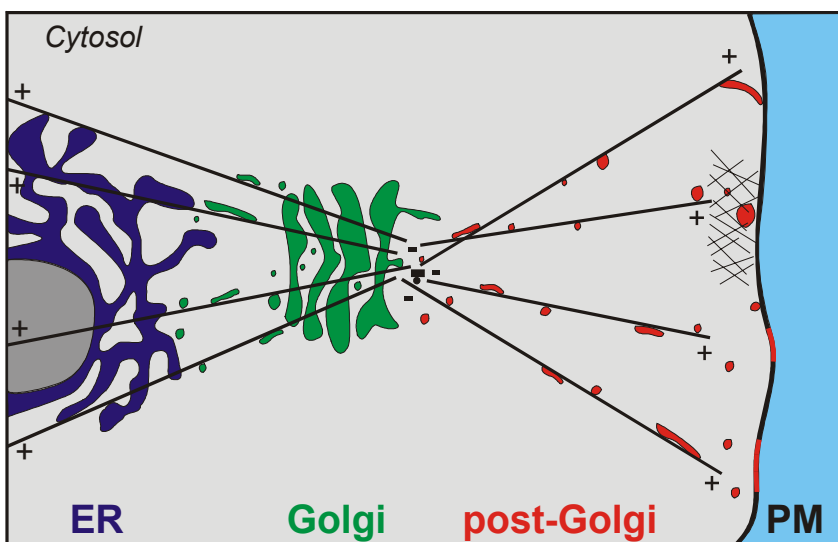


Figure 1.1. Schematic of the secretory pathway. The endoplasmic reticulum (ER, blue), the Golgi complex (green), the oriented microtubules (straight black lines from minus to plus), the post-Golgi carriers (red) and the plasma membrane (PM, black) are indicated.

Early morphological studies on fixed cells have provided a framework for our current understanding of the distribution and organization of the organelles forming the secretory membrane system (Palade, 1975). Further, biochemical and genetic approaches have given insight into the regulatory machinery on the molecular level (Rothman, 1994; Ferro-Novick and Jahn, 1994; Schekman and Orci, 1996; Rothman and Wieland, 1996). More recently, the advent of green fluorescent protein (GFP) (Prasher et al., 1992; Tsien, 1998) combined with modern imaging technologies has made it possible to directly observe secretory membrane traffic in living cells (Gerdes and Kaether, 1996; Lippincott-Schwartz et al., 2000; Lippincott-Schwartz, 2001). Time-lapse imaging of secretory cargo proteins tagged with GFP has provided detailed insight into the temporal and spatial distribution of cargo molecules within the cell, including their origin, transport mechanism and destination (Kaether and Gerdes, 1995; Presley et al., 1997; Hirschberg et al., 1998).

1.1. Why image constitutive exocytosis?

Constitutive secretion, the process that delivers newly synthesized proteins to the plasma membrane and external media, occurs in all eukaryotic cells. In contrast, regulated secretion is a triggered process that is observed in particular cell types, such as neurons, endocrine cells and exocrine cells. The vesicular model of secretion, which states that exocytosis occurs in discrete quanta rather than as a continuous flux, is largely based on data from regulated secretory cells. In early studies on the frog neuromuscular junction, quantal end-plate potentials detected at the postsynaptic muscle cell following a presynaptic nerve impulse were considered the first evidence for this model (Fatt and Katz, 1952; Del Castillo and Katz, 1954). Since then a variety of techniques, specifically amperometry, electrophysiology and microscopy, have been used to detect single exocytic events in regulated secretion (Chapter 3).

The complete machinery involved in mediating either regulated or constitutive exocytosis is far from being determined. However, it is generally accepted that both pathways use a similar mechanism (Palade, 1975). They

share many homologous molecular components, including the SNAREs, the rab-GTPases and the Sec1/Munc-18 related proteins (Schekman and Orci, 1996; Rothman and Wieland, 1996; Jahn and Sudhof, 1999). The inability to trigger constitutive exocytosis, however, has made it difficult to address some of the mechanistic issues. Specifically, it has been difficult to study the end stage of constitutive secretion, the fusion of single post-Golgi carriers with the plasma membrane. Previous imaging studies on the dynamics of secretion were limited to monitoring earlier phases of the secretory pathway. Laser scanning confocal microscopy of a GFP-tagged membrane protein expressed in live cells was first used to visualize ER to Golgi traffic in real time (Presley et al., 1997). Further, quantitative analysis of time-lapse images using the same reporter demonstrated that the rate of secretion through the constitutive secretory pathway follows simple first order kinetics (Hirschberg et al., 1998). It seems now established that microtubules are involved in the long-range transport of membrane cargo to the periphery of the cell, but it remains elusive which cytoskeletal component is necessary for the final targeting step (Hirschberg et al., 1998; Toomre et al., 1999).

In this work we have focused on the final step of constitutive secretion – the fusion of post-Golgi carriers with the plasma membrane. Prior to this work, a quantitative method for the microscopic detection of single fusion events in live cells did not exist. Such a method would supply spatial and temporal information about single fusion events. Quantitative analysis of the localization and kinetics of the fusion process could afford insight into as yet unknown aspects of constitutive exocytosis.

1.2. Total Internal Reflection Fluorescence

Microscopy

Recent technical advances in the methodology of fluorescence microscopy have made it possible to perform quantitative studies on the dynamics of single organelles (Kaether and Gerdes, 1995; Presley et al., 1997; Hirschberg et al., 1998) or even single proteins inside living cells (Goulian and Simon, 2000).

Modern microscopes are extremely efficient in light collection, mostly due to the development of high numerical aperture objectives. The sensitivity of detectors, such as cooled CCD cameras, has been continuously improved over the last decade and the availability of fast computers facilitates the acquisition and processing of large amounts of imaging data. One aim of this work was to apply state-of-the-art technology to perform time-lapse imaging of single post-Golgi carriers fusing with the plasma membrane.

So far the most sensitive method to image events at the cell-substrate interface using fluorescent probes is total internal reflection fluorescence microscopy (TIR-FM, also called 'evanescent wave microscopy'). Hirschfeld first introduced TIR-F in 1965 as a method of selective surface illumination at a solid to liquid interface (Hirschfeld, 1965). TIR-FM (Axelrod, 1989) was first used in cell biology to image cell-substrate contacts (Axelrod, 1981; Gingell, 1981). Over the past two decades, TIR-FM has been used to image various surface events in cell biology. For instance, the contact region between leukemia cells and a planar lipid bilayer (Weis et al., 1982), single molecule interactions *in vitro* (Funatsu et al., 1995), and the dynamics of cellular membranes *in vivo* (Steyer et al., 1997) have been imaged using this technique (Oheim et al., 1998; Sund et al., 1999).

In TIR-FM, an excitatory beam of light is directed through the coverslip at an angle steep enough that it completely reflects off the coverslip-water interface (Chapter 2). This results in what is called an 'evanescent field'. This is an excitatory field that decays exponentially with distance from the coverslip into the aqueous medium, in this case the cell. Typically, the intensity of the evanescent field decays within ~100nm down to 1/e of its value at the interface. Therefore, only fluorescent molecules within this distance from the coverslip are excited strongly enough to be visible. The main advantage of TIR over epifluorescence illumination is therefore the reduction of background fluorescence emerging from deeper parts of the cell. In other words, TIR-FM is ideal to selectively excite fluorophores at the contact surface of cells adhering to a coverslip, and, in that way to image exocytic events.

The fluorescence caused by TIR excitation emanates from a very thin optical section (~100 nm), which is much smaller than the minimal optical section taken by laser scanning confocal microscopy (~500 nm). In addition, TIR-FM provides wide-field illumination and fast direct imaging, whereas in a confocal setup, the image has to be reconstructed from many scanned spots. Our results will demonstrate that TIR-FM is the first, and so far the only, imaging technique by which fusion of single vesicles can be detected in a quantitative manner (Chapter 3).

1.3. Applying TIR-FM to study membrane traffic

There have been several applications of TIR-FM in cell surface imaging (Wang and Axelrod, 1994; Omann and Axelrod, 1996; Thompson and Lagerholm, 1997; Murthy, 1999; Sund et al., 1999) and in single molecule microscopy during recent years, demonstrating the high impact of this technique on cell biological research (Schmoranzer et al., 2000; Sund and Axelrod, 2000; Toomre et al., 2000; Ishijima and Yanagida, 2001). Recent technical advances, especially increased sensitivity due to the introduction of 'ultra' high numerical aperture objectives (Tsuboi et al., 2000; Axelrod, 2001), has extended the application range of TIR-FM in cell biology even further (Schmoranzer et al., 2000; Steyer and Almers, 2001). The increasing demand for TIR-FM systems in cell biology has recently motivated microscope companies to begin developing complete "turn-key" TIR-FM systems. However, while the work presented here was underway, such "user friendly" TIR-FM systems were not yet available. Therefore, one goal of this work was to build and optimize a TIR-FM system capable of detecting single fusion events of constitutive post-Golgi carriers with the plasma membrane. We then applied this method of fusion detection to answer basic questions in membrane traffic. In brief, the questions are:

1. Are there different classes of post-Golgi carriers (spherical or tubular structures) that fuse with the plasma membrane during constitutive exocytosis?
2. Where at the cell surface does fusion occur in non-polarized cells, such as

stationary fibroblasts and sub-confluent epithelial cells?

3. Where at the cell surface does fusion occur in polarized cells, such as migrating fibroblasts and confluent epithelial cells? In other words, is there any domain-specific targeting in any of these cases?
4. What cytoskeletal components are involved in the targeting? What happens during disruption of the cytoskeleton?
5. Are different cargo molecules sorted into different vesicles at the Golgi/TGN? Do similar sorting steps exist during recycling from endosomal compartments?

Chapter 2 gives a technical introduction into the TIR-FM setup. Chapter 3 describes the method for the quantitative detection of single fusion events. Chapters 4 and 5 describe the investigation of the post-Golgi traffic in fibroblasts and epithelial cells. Chapter 6 is a combined discussion of the Chapters 3, 4 and 5. The results presented in Chapter 7 are discussed separately. Each chapter includes a detailed introduction into the relevant subject.

2. Total Internal Reflection Fluorescence Microscopy: Theory and Practical Approach

The theory of TIR-FM, as well as most practical aspects for application in biology have been described in detail previously (Gingell and Todd, 1979; Axelrod, 1989). While our work was underway, TIR-FM became increasingly popular in cell biological research, mostly due to the advent of ‘ultra’ high numerical aperture objectives (Axelrod, 2001). Here, I give a brief introduction to the basic theory of TIR-FM, which is necessary to understand the experimental approaches used in this work.

2.1 Theoretical background

When a light beam passing through a medium of high refractive index (e.g. glass, n_g) encounters an interface to a medium of lower refractive index (e.g. water, n_w), it undergoes refraction, a change in direction of propagation away from the optical axis (Fig. 2.1a, black beams). Snell’s law describes the relation between incident angle θ_g and refracted angle θ_w .

Snell’s law:
$$n_g \cdot \sin\theta_g = n_w \cdot \sin\theta_w$$

If the incident angle θ_g is increased up to the ‘critical’ angle θ_c , the beam propagates in the plane of the interface (Fig. 2.1a, red dotted beam). The critical angle follows from Snell’s law for $\theta_w = 90^\circ$.

Critical angle θ_c :
$$\theta_w = 90^\circ \rightarrow \theta_g = \theta_c = \sin^{-1}(n_w/n_g)$$

Total internal reflection occurs only when the incident angle θ_g is higher than the critical angle θ_c .

Total Internal Reflection:
$$\theta_g > \theta_c$$

For $\theta_g > \theta_c$, all of the light reflects back into the glass. However, some of the incident energy penetrates the interface and propagates along the interface. The

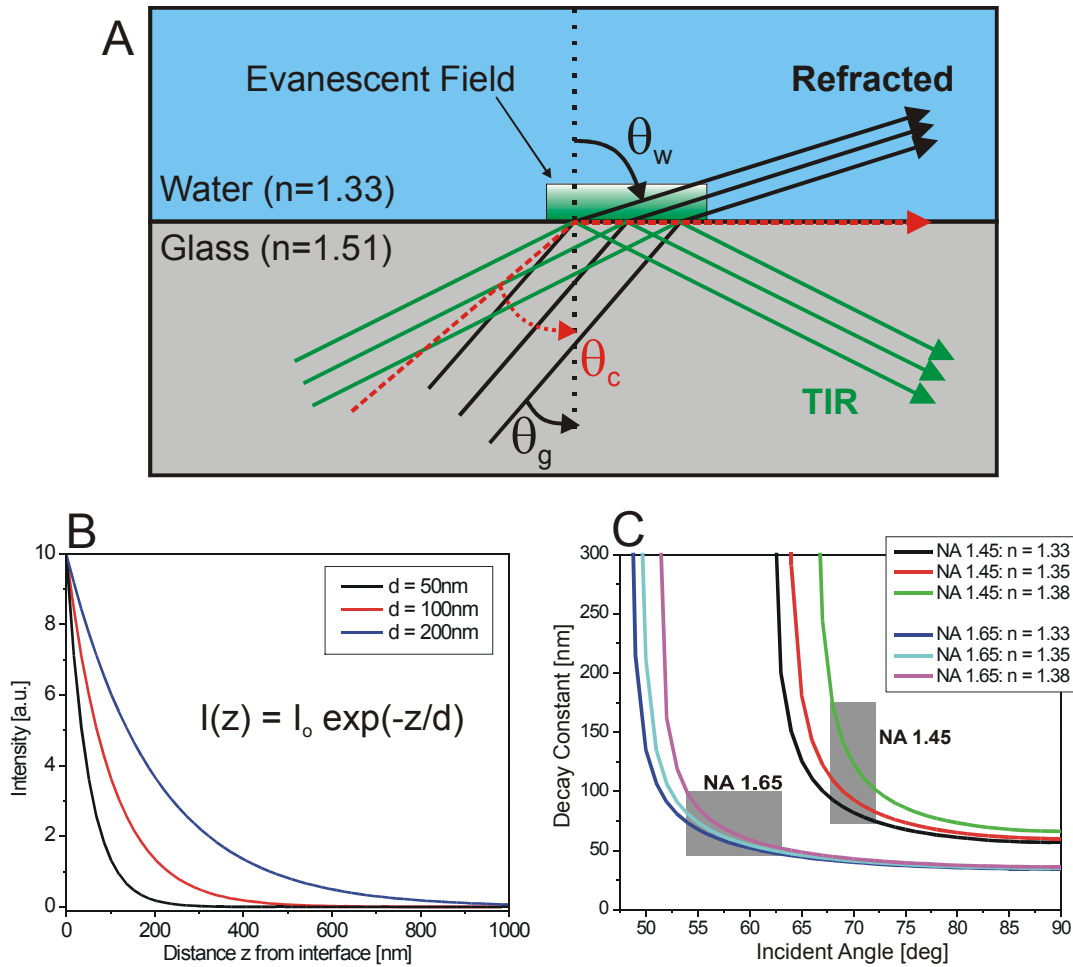


Figure 2.1. (A) Illustration of Snell's law, Refraction and Total Internal Reflection. Refracted beams (black), the beam at 'critical' incident angle (red dotted) and total internal reflected beams (green) are illustrated at a glass-water interface. The evanescent field is indicated in green, falling exponentially with distance from the interface.
(B) Exponential decay of Evanescent Field. The intensity of the evanescent field in the aqueous media is plotted over the distance from the coverslip/water interface for various decay lengths (50nm, 100nm, 200nm) typical of our experiments.
(C) Estimation of the decay constant of the Evanescent Field for different high N.A. objectives and refractive indices. The decay constant for both objectives (N.A. 1.65 and N.A. 1.45) are plotted according to equation (2) for various refractive indices ($n = 1.33, 1.35, 1.38$), typical of cells in aqueous media. The ranges of measured incident angles (methods) for both objectives and the resulting values for the decay constant are indicated by the gray boxes.

field of this propagating wave in the water is called the evanescent field (or evanescent wave). The intensity of the evanescent field I falls off exponentially with distance z into the aqueous medium, with a characteristic decay constant d (Fig. 2.1b).

Evanescent field intensity:
$$I(z) = I_0 \cdot e^{-z/d} . \tag{1}$$

If $z = d$, the intensity of the evanescent field $I(z)$ has decayed to $1/e$ of the value at the interface I_0 . The characteristic decay distance d depends on the wavelength of the incident light λ_0 , the incident angle θ_g and the relative refractive indices of the coverslip n_g and the aqueous medium n_w .

Decay constant:
$$d = \lambda_0 / 4\pi (n_g^2 \sin^2 \theta_g - n_w^2)^{-1/2} \quad (2)$$

In physical terms, the phenomenon of TIR at an interface is seen to be a continuum, rather than a sudden change at $\theta_g = \theta_c$. For small θ_g the light waves in the aqueous medium have a certain sinusoidal period. With θ_g approaching θ_c , these periods become larger as the refracted beam propagates increasingly parallel to the interface. At $\theta_g = \theta_c$, the period is infinite while the wave fronts of the refracted beam are perpendicular to the interface. This corresponds to an infinite decay constant d . With increasing θ_g beyond θ_c , the period becomes mathematically imaginary, which physically results in a finite d value (typically on the order of a tenth to a third of the wavelength) and the exponential decay of the evanescent field into the aqueous medium (Fig. 2.1c).

By measuring the incident angles at which TIR occurred, we estimated the range of possible values for d in our experiments for typical values of the refractive index n_w (Fig. 2.1c). According to these measurements, the evanescent field decayed within 50-200nm from the coverslip into the aqueous medium, depending on the type of objective.

2.2. Comparison of EPI- and TIR-illumination

The main difference between standard epifluorescence microscopy and TIR-FM is schematized (Fig. 2.2). In epifluorescence (left) the exciting beam is directed straight up through the objective, the coverslip and the specimen. As illustrated in the enlargement above, the whole cell is illuminated. In TIR-FM (right), the excitatory beam is directed through the coverslip at an angle higher than the critical angle, so that TIR occurs. For the experiments described in this work, the evanescent field reaches about 50–200nm into the aqueous medium, depending on the incident angle and the type of objective we have used (see 2.3.). As a

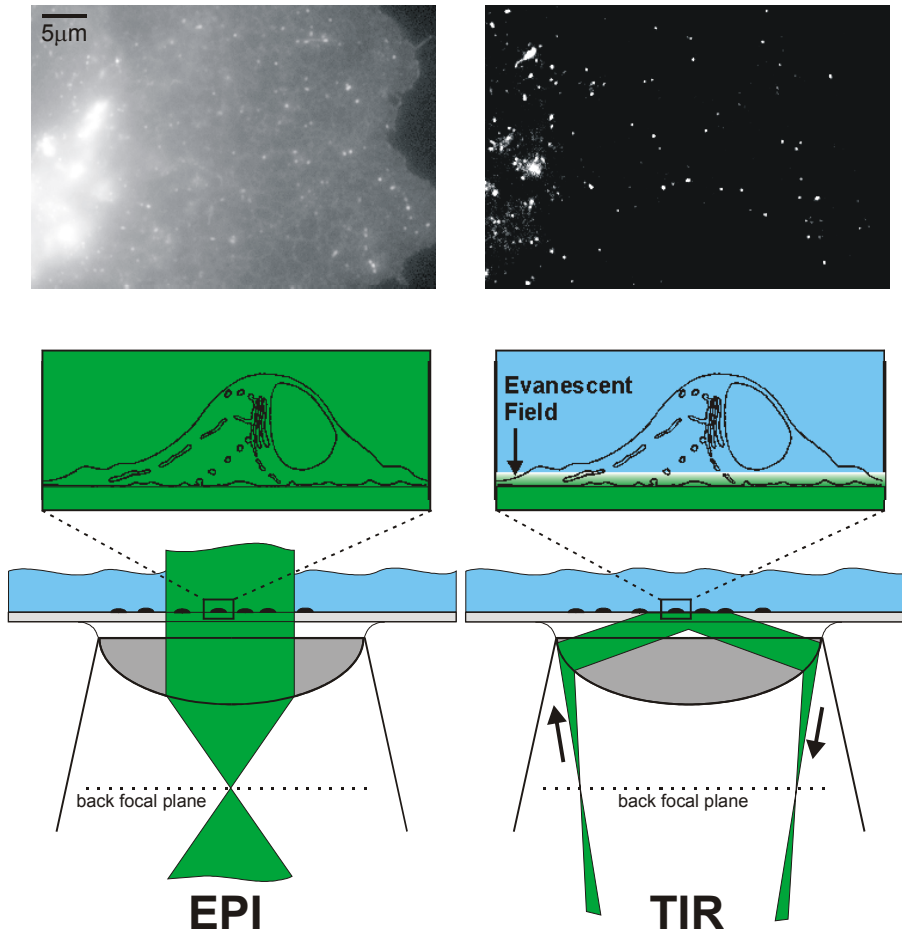


Figure 2.2. Comparison between standard epifluorescence and total internal reflection fluorescence illumination. In both schematics, the excitatory beam (green), the objective lens and the coverslip (gray), the cells (small black spots) and the aqueous medium (blue) are illustrated. In epi-fluorescence (left) the exciting beam is directed straight up through the objective, the coverslip and the specimen. As illustrated in the enlargement above, the whole cell is illuminated. In TIR-FM (right), the exciting beam is directed through the periphery of the objective, resulting in a steep enough angle to be totally internally reflected. Only fluorophores within the evanescent field are excited. The images above the schematic show a COS cell transfected with VSVG-GFP illuminated in epi-fluorescence (left) and TIR-FM (right). Under epifluorescence, the entire cell is visible, with a strong signal in the left area (Golgi complex). In TIR-FM, the excitatory evanescent field decays exponentially with distance from the coverslip (~100nm). Thus, only vesicles very close to the membrane are visible.

result, only fluorescent molecules within this distance from the coverslip are excited, enabling high signal-to-background imaging of surface events.

For illustration, a cell transfected with a secretory membrane protein (VSVG-GFP) was imaged with both epifluorescence microscopy and TIR-FM (Fig. 2.2, top). Under epifluorescence microscopy, the entire cell was visible, with a particularly strong signal in what is probably the Golgi complex (the bright spots

in Fig. 2.2, top left). In TIR-FM, the excitatory evanescent field decays exponentially from the cover slip over ~ 100 nm. Thus, only GFP molecules inside this field fluoresce. The Golgi complex was not visible in TIR-FM, indicating that it was far enough away from the coverslip to be outside the evanescent field (Fig. 2.2, top right). Note that even in the area of the Golgi, TIR-FM resolved distinct transport intermediates close to the plasma membrane with high signal-to-background ratio.

2.3. 'Objective-type' versus 'Prism-type' TIR-FM

Recent technical advances, especially the design of 'ultra' high numerical aperture (N.A.) objectives, have made it possible to perform the 'objective-type' TIR-FM on living cells. For comparison, versions of both the 'prism-type' (left) and the 'objective-type' (right) are schematized (Fig. 2.3). In the traditional 'prism-type' TIR-FM setup, the exciting beam is coupled into the coverslip via a prism (here trapezoid). This approach allows a variety of arrangements, each optimized for a specific application (Axelrod, 1989). Typically, the fluorescence emission is collected through an objective from the opposite side of the prism and the sample, in an upright microscope configuration (Fig. 2.3, left). The relatively large distance between sample and the objective limits this application to an objective with a large working distance and a low N.A. (typically 0.75 or less). It is possible to perform the prism-type TIR-FM with an N.A. higher than 0.75, however, the physical arrangements have limitations in ease of use (Axelrod, 1989).

In the 'objective-type' TIR-FM setup, the supercritical angle on the coverslip/water interface is reached by focusing the excitatory beam on the periphery of the back focal plane of the objective¹. This way, the beam is refracted by the objective and directed through the refractive index-matched media: the objective, the immersion liquid and the coverslip. In this elegant way, the objective functions as the prism delivering the exciting beam *and* as the optics collecting the emission. The main advantage is that objective-type TIR-FM

¹ The back focal plane is the plane inside an objective at which all parallel incoming beams are focused on one spot. Thus, a beam focused on the back focal plane leaves the objective collimated.

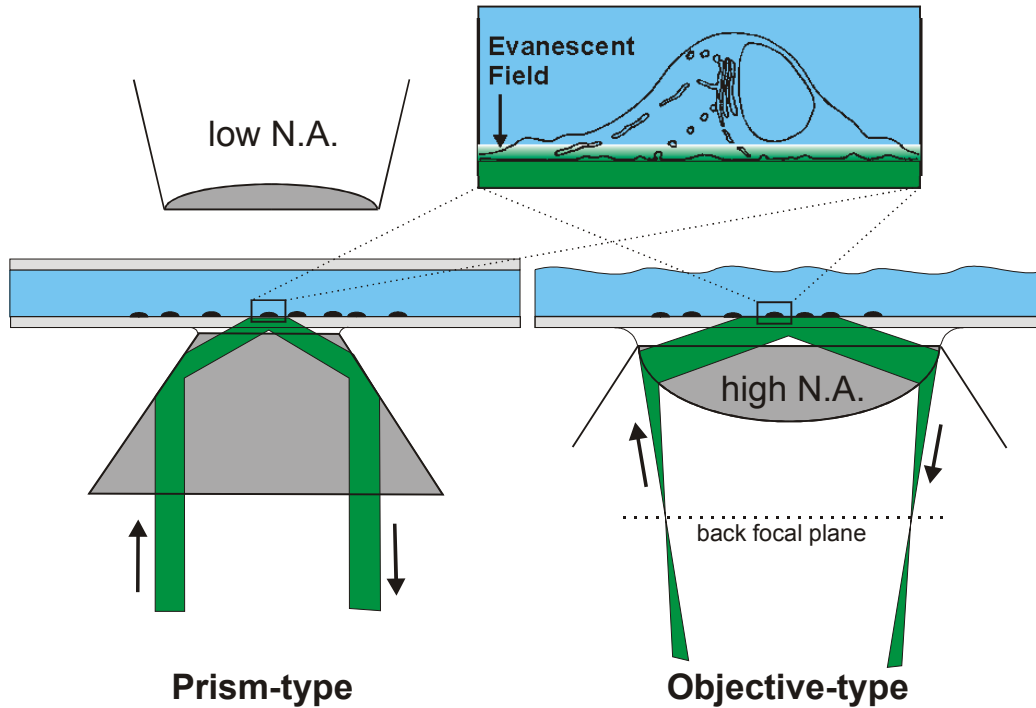


Figure 2.3. Prism-type versus Objective-type TIR-FM. In the prism-type TIR-FM (left) the exciting beam (green) is coupled into the coverslip through a prism located on the opposite side of the low numerical aperture (N.A.) objective. In the ‘objective-type’ TIR-FM (right) the exciting beam (green) is coupled into the coverslip through the high N.A. objective. To yield TIR, the exciting beam is focused on the periphery of the back focal plane, such that the incident angle is larger than the critical angle. Both types result in very similar TIR illumination. The main advantage of the objective-type approach is the more efficient light collection due to the use of high N.A. objectives.

employs high numerical aperture, short working distance objectives, resulting in much higher fluorescence emission collection compared to the prism-type approach. The advantages have been described in more detail elsewhere (Axelrod, 2001).

The numerical aperture of an objective is defined as the product of the refractive index of its material (including lens, immersion and coverslip) and its maximal opening angle θ_{max} .

Numerical aperture:
$$\text{N.A.} = n \cdot \sin\theta_{max}$$

As mentioned above, the critical angle θ_c depends on the refractive indices of both media. Thus, for TIR to occur with tissue culture cells on the coverslip, the refractive index n_g (objective, immersion and coverslip) should be significantly

above the refractive index for the aqueous medium and the cells n_w . For adherent tissue culture cells in aqueous medium n_w is estimated to range between 1.33 (water) and ~1.38 (cells) (Steyer and Almers, 2001). Therefore, the use of 'regular' high numerical aperture objectives with N.A.=1.4 are extremely marginal for yielding 'clean' TIR. The use of 'ultra' high N.A. objectives (N.A.>1.4) facilitates the objective-type TIR-FM for imaging the surface of living cells and allows a range of incident angles for controlling the depth of the evanescent field. Further, the objective-type TIR-FM requires minimal modification, mainly in the beam delivery system, of a regular epifluorescence microscope. Additionally, in an inverted system, the sample is fully accessible for external manipulations such as addition of drugs, microinjection or electrophysiological recordings.

Some disadvantages of 'ultra' high N.A. objectives is the high cost and the limitation to high magnification (60x or higher), which might be problematic for some applications in cell biology where simultaneous imaging of multiple cells is required. In this work, we used two different 'ultra' high N.A. objectives recently developed by Olympus, the Apo 100x 1.65 NA and the Apo 60x 1.45 NA.

The Apo 100x 1.65NA : Because of its unusually high refractive index ($n=1.78$), this objective offers a wide range of usable angles to achieve TIR on living cells (Fig. 2.1c) (Terakawa et al., 1997). The angles under which TIR occurs were estimated to range between 54° and 63° (methods), resulting in an evanescent field decay constant ranging from 50-100nm (Fig. 2.1c, gray box, NA 1.65). The main disadvantages of this objective are the requirement for a special high refractive index immersion liquid ($n=1.78$) and high refractive index coverslips ($n=1.78$). The currently available immersion liquid is volatile and slightly toxic, leaving a crystalline remnant on the objective after a few hours in a heated environment. The special coverslips supplied by Olympus (material: Schott glass type LAFN21, thickness 0.150 mm) are extremely expensive (\$ 30 ea) and fragile. Reuse is problematic because the material dissolves in an acid bath. An acid resistant alternative is the Schott glass type SF11 available in 0.150 mm thickness for ~1/3 of the price (VA Optical, San Anselmo, CA). SF11 is slightly more autofluorescent than LAFN21, but not enough to cause a real

problem in live cell microscopy. However, the SF11 was found to cause severe chromatic focal mismatch and is therefore only usable for single-color experiments.

The Apo 60x 1.45NA : Most of the problems associated with the 100x 1.65NA objective are overcome by the recent introduction of the 60x 1.45NA (Olympus) and the 100x 1.45NA (Zeiss), which use regular immersion oil and coverslips. The range of incident angles for TIR is smaller for the 60x 1.45NA (67-72°) compared to the 100x 1.65NA. Therefore, the decay constant of the evanescent field for the 60x 1.45NA is larger ($d \sim 75\text{-}200\text{nm}$) than for the 100x 1.65NA ($d \sim 50\text{-}100\text{ nm}$) (Fig. 2.1c, gray boxes). Because of the limited sizes of cooled CCD arrays, the lower magnification of the 60x objective is more suitable for the imaging of whole tissue culture cells, which in some cases are too large to be imaged with 100x magnification. Due to the obvious advantages of the Apo 60x 1.45NA over the Apo 100x 1.65NA, we preferred the 60x for routine imaging on whole cells.

2.4. Objective-Type TIR-FM setup

A regular inverted fluorescence microscope requires a few modifications to be used for objective-type TIR-FM. To employ the 'ultra' high N.A. objectives, it was necessary to build a custom excitation system (Fig. 2.4, methods). The beam from a Argon-ion laser (488nm) was coupled into a single mode optical fiber for remote beam delivery, passed through an electronically controlled shutter (S), collimated by a convex lens (L1), cropped by a field diaphragm (FD), attenuated by a neutral density filter (ND) and delivered via two mirrors (M1, M2) to the dichroic² mirror of the inverted microscope. The beam was focused on the back focal plane of the high N.A. objective via a movable convex lens (L2). To align the TIR, the beam was centered in the field of view and positioned at the periphery of the objective by tilting the mirrors (M1, M2) and moving the lens (L2). TIR was verified and tested as described (methods).

² A dichroic mirror is usually a longpass interference filter which is placed in a 45° angle into the epifluorescence lightpath to reflect the excitatory light onto the sample while the emission is transmitted.

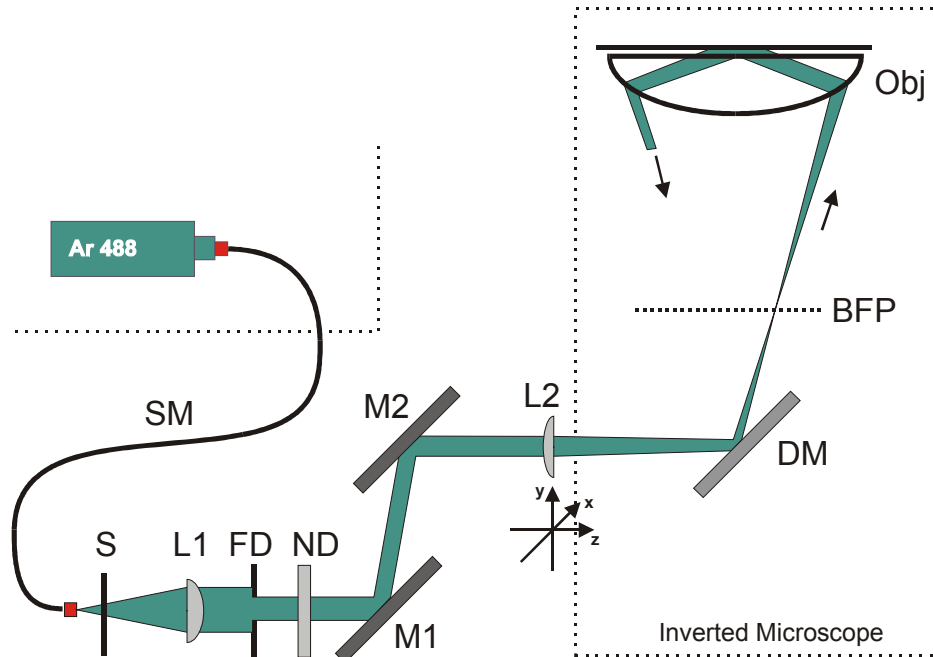


Figure 2.4. Single-color TIR-FM illumination system for GFP excitation. The beam from an Argon laser (488nm) was coupled into a single-mode optical fiber (SM) for remote beam delivery, passed through an electronically controlled shutter (S), collimated by a convex lens (L1), cropped by a field diaphragm (FD), attenuated by a neutral density filter (ND) and delivered via two mirrors (M1, M2) to the dichroic mirror of the inverted microscope. The beam was focused on the back focal plane (BFP) of the high N.A. objective via a movable convex lens (L2). (see also photograph in appendix)

2.5. Multi-color TIR-FM

Study of colocalization of multiple reporter proteins with TIR-FM was expected to provide answers to fundamental questions about the sorting, transport and targeting of various membrane proteins on their way to the plasma membrane. For example, what cytoskeletal elements colocalize with post-Golgi carriers during fusion? Or, are different membrane proteins, which originate from the same compartment, delivered in separate or in identical vesicles to the plasma membrane? The simultaneous imaging of at least two colors was needed to expand the experimental options of the TIR-FM setup. While investigations were underway, a multi-color TIR-FM system was not commercially available. Therefore, a novel system was set up, capable of imaging two proteins tagged with different fluorophores simultaneously in TIR-FM.

The detection of single vesicle fusion with the plasma membrane requires high temporal resolution. The minimum time resolution depends on the load of the reporter protein in the vesicle, the intensity of excitation and the efficiency of detection. For most vesicles derived from the biosynthetic pathway, the minimum time resolution for quantitative detection of single fusion events was found to be ~5 frames/sec with our system. Thus, it was crucial to monitor both proteins at the exact same time to make any quantitative claim about spatial and temporal colocalization. In such a simultaneous dual-color setup, both fluorophores are excited with separate laser lines (at the same time) and the dual-color emission is split by an emission splitter onto the detector. After the acquisition the two colors can be separated and aligned using off-line software. In summary, the single-color system was expanded using a multi-laser combiner system on the excitation side and a dual-channel splitter on the emission side.

2.5.1. Multi-color TIR-FM illumination

The multi-color TIR-FM system was designed for the use of currently available live cell probes, most important the spectrally different mutants of green fluorescent protein (GFP). It enabled us to image the following pairs of fluorophores simultaneously: cyan fluorescent protein together with yellow fluorescent protein (CFP, YFP) and GFP together with various red fluorescing probes (dsRED, Cy3 or Cy5). A similar approach was used to simultaneously image Cy3 and Cy5 with TIR-FM previously (Sako et al., 2000). The lasers for the setup were chosen for optimal excitation of each of these fluorophores (Table 2.1).

To perform TIR-FM with two different laser lines at the same time, the laser beams have to enter the beam expander co-linearly to ultimately yield the same depth of the evanescent field³. For this purpose we built a multi-laser combiner, based on a mirror system (Fig. 2.5a).

³ According to equation (2) the decay constant d depends linearly on the wavelength. Therefore, the intensity of the evanescent field will be slightly different (~5-10%) for the wavelengths used in our experiments. Since we do not compare absolute values in the intensity during the dual-color experiments, this effect is negligible.

Table 2.1: Lasers and dichroic mirrors of the multi-laser combiner.

Laser	Line(s) [nm]	Max. power [mW]	Fluorophore	Dichroic Mirrors
HeCd	442	20	CFP	455LP
Argon Ion	488 or 514	55 or 40	GFP or YFP	525LP
HeNe green	543	1,5	Cy3	565LP
HeNe red	633	10	Cy5	Mirror

Practically, there are two ways to combine laser lines of different wavelengths, either by employing a system based on dichroic mirrors, or a system based on fused optical fibers. In the optical fiber system each laser line is fed into a separate fiber, which can then be fused together into one single fiber to combine the lines. Initially, this approach was considered to be the most elegant, because it does not require complex mechanical beam delivery systems. However, the loss of about 50% of light in the currently available fused fiber combiners forced us to abandon the fiber approach, because at the time we were limited to use relatively inexpensive low power lasers. In addition, the currently available fused fibers combine only 2 laser lines at the same time, whereas a laser combiner system based on dichroic mirrors is easily extendable to more than 2 lines.

The laser combiner (Fig. 2.5a) consists of various reflective mirrors (M) for beam delivery and custom made dichroic mirrors (DM) for the combination of the laser-lines listed in Table 2.1. The additional lasers were mounted in vertical arrangement and each beam was reflected off adjustable mirrors (M) for accurate delivery. The dichroic mirrors (DM) were placed at a 45° angle to the beam path, also on adjustable mounts in order to fine-tune the co-alignment of the beams. The combined beams entered the electronic shutter (S) of the single-color setup (Fig. 2.4).

A few modifications had to be made to the single-color setup to accommodate the simultaneous delivery of different laser lines for TIR-FM. The

use of multiple laser lines with different wavelengths requires chromatically corrected optics for focusing all colors onto the same spot in the back focal plane. Therefore, the original lens system consisting of L1 and L2 (Fig. 2.4) was replaced with achromatic lenses. In addition, the dichroic mirror (DM) was replaced with custom-made polychroic mirrors⁴ (PC) which enabled us to deliver at least two exciting laser beams. The PCs used here were designed to reflect both the laser lines and to have an optimized transmission band in between the laser lines.

2.5.2. Dual-color emission splitter

As mentioned earlier, simultaneous dual-color acquisition is crucial for following rapid movements and fusion of vesicles marked with different color probes. This was achieved by using a dual-channel emission splitter (Fig. 2.5b, methods). The emission splitter is mounted in between the microscope and the camera. The emission splitter is mounted in between the microscope and the camera. The

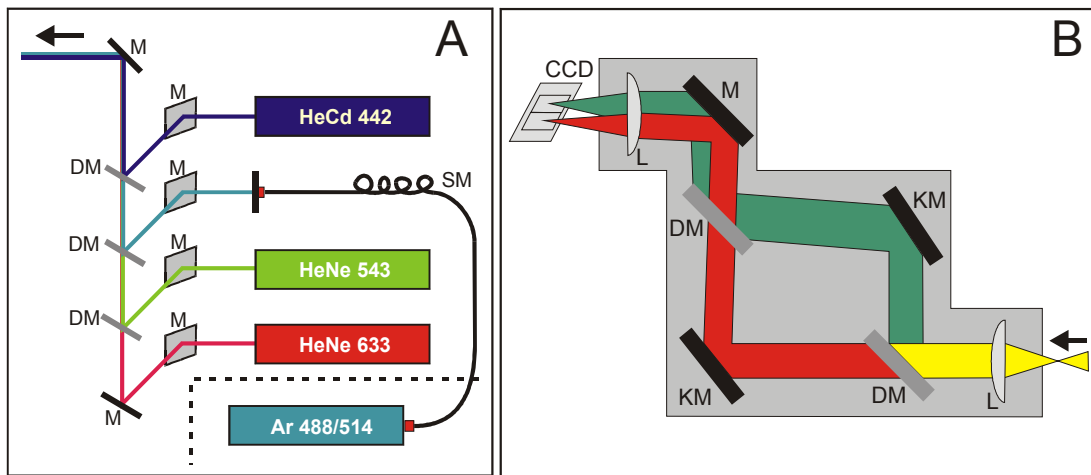


Figure 2.5. (A) Multi-color TIR-FM laser combiner. Additional lasers (methods) to the Argon laser were arranged vertically. The beams were delivered via adjustable mirrors (M) to the dichroic mirrors (DM). By adjusting the angles of the dichroic mirrors, the beams could be co-aligned. The remaining excitation path was very similar to the single-color TIR-FM illumination system (Fig. 2.4).

(B) Dual-Channel Emission Splitter. The emission splitter was attached between the microscope and the CCD camera. The mixed dual-color emission from the microscope (yellow) is collimated by a lens (L), then split by a dichroic mirror (DM) with appropriate cut-off wavelength (see Table 2.1) into red and green emission. Kinematic (adjustable) mirrors (KM) help to align the separate emissions side-by-side on the CCD array.

⁴ A polychroic mirror is a dichroic mirror which is designed to reflect more than one excitatory wavelength (here two) and transmit the emission of more than one color.

mixed dual-color emission from the sample leaving the microscope (here yellow) is first collimated by a lens (L) and then split into separate channels by a dichroic mirror (DM). The channel with the longer wavelength (here red) passes through DM while the channel with shorter wavelength (here green) is reflected. A second DM identical to the first is used to recombine the two channels and a second lens (L) to image both channels onto the camera. Both emission channels are positioned by kinematic (movable) mirrors (KM) to appear side by side on the same camera. Following acquisition, the two channels have to be co-aligned on pixel by pixel basis (methods). A simple but costly alternative to the emission splitter is the installation of two separate cameras. This would have the advantage that the whole CCD array can be used for imaging the sample and not just one half of it.

2.5.3. Optimization of a filter set for simultaneous dual-color imaging – current limitations

In comparison to single-color acquisition, where the whole emission tail of a fluorophore can be collected, the light collection in simultaneous dual-color acquisition is limited by the use of polychroic mirrors and narrow emission bandpass filters. This is best demonstrated by the example of CFP- and YFP-emission (Fig. 2.6). The spectra of the custom-made filter set used for the simultaneous imaging of CFP- and YFP-tagged proteins are shown in Fig. 2.6a. The laser lines for excitation of CFP (442nm, blue line) and YFP (514nm, green line) are indicated. The spectrum of the polychroic mirror (PC) is shown in black, the spectrum of the dichroic mirror in the emission splitter (505 DCLP) is shown in dotted black line and the spectra of the emission bandpass filters for CFP and YFP are shown in cyan and yellow, respectively. For comparison, the excitation/emission spectra of CFP and YFP are shown in Fig. 2.6b. The spectra of CFP and YFP are not completely separate. The tail of CFP emission spectrally overlaps with the emission of the YFP. Depending on the chosen emission filters, a part of the CFP emission is collected together with the YFP emission. This is called the “bleed-through” of the CFP into the YFP emission. To minimize this bleed-through, narrow emission bandpass filters with minimal overlap are

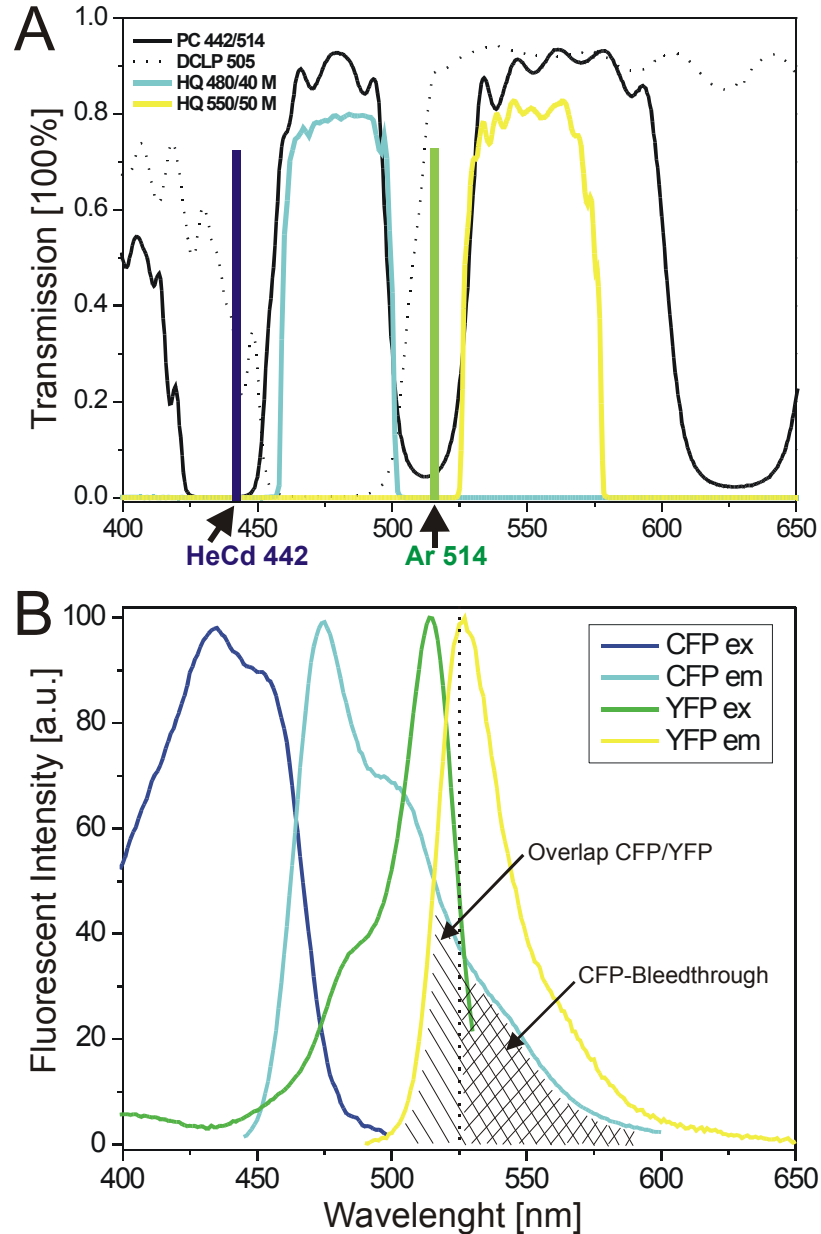


Figure 2.6. Filter spectra for simultaneous dual-color imaging of CFP and YFP.

(A) The 442nm line from a HeCd laser (dark blue) as well as the 514nm line from an Argon-Ion laser (green) are reflected off a polychroic mirror (pc 442/514, black line) for excitation. The emission of CFP and YFP is split (inside the emission splitter, Fig. 2.5b) by a dichroic mirror (dotted black line, DCLP 505) and cleaned up with emission bandpass filters (CFP: light blue, HQ480/40M; YFP: yellow, HQ550/50M).

(B) The excitation/emission spectra of CFP and YFP are shown for comparison. The cut-off wavelength of the YFP emission bandpass filter is indicated (dotted black line). Note that the cut-off wavelength of the polychroic (black line in A) limits the extent of emission collected for both channels. (The spectra of CFP and YFP were kindly provided by Michael Stanley, Chroma Techn. Corp., Brattleboro, VT.)

required (Fig. 2.6a). Even though the filter-set was optimized for CFP/YFP, it yielded a bleed-through of close to 50%, meaning that 50% of the CFP signal was detected in the YFP channel. However, since the CFP channel is 100% 'clean' of YFP emission, quantitative bleed-through correction can be performed routinely for all acquired dual-color data (methods).

The polychroic mirrors and the narrow bandpass emission filters (in the emission splitter) are responsible for the moderate emission collection efficiency of a dual-color setup. The reduced light collection compared to a single-color setup (~50%) must be compensated by an increase in excitation intensity, leading to increased photo-bleaching of the probe. For TIR-FM, the requirement for higher excitation intensity also means the purchase of higher power and more expensive lasers. Further, currently available dual-channel emission splitters (methods) have been made available for research in fluorescence microscopy only recently. The ease of use and the optical properties are far from being optimized. We observed chromatic focal mismatches, field distortions and rotational misalignments, between pairs of emission channels. In addition, the light loss through the optical element was estimated to ~30%. Future efforts in improvement of the optical properties (chromatic and spherical correction, light throughput) of the emission splitters might minimize these problems.

Comparing the transmission spectra of the chosen filters (Fig. 2.6a) with the excitation/emission spectra of the proteins CFP and YFP (Fig. 2.6b), it is apparent that the laser sources and the filter-set used in our simultaneous dual-color experiments were optimized to (i) maximize emission collection, (ii) minimize bleed-through and (iii) reduce the background originating from longer wavelengths. Similar optimization of filter sets was done for the dual-color imaging of GFP and Cy3 (methods).

3. Imaging Constitutive Exocytosis: A Quantitative Method for the Detection of Single Fusion Events

3.1. Introduction

Most of the data supporting the vesicular model of secretion originates from assays on individual fusion events in regulated exocytosis. When a cell is stimulated to secrete, quantal packages of content are released into the extracellular space. This model was originally suggested by the detection of a quantal end-plate potential arriving in the postsynaptic cell at the frog neuromuscular junction (Fatt and Katz, 1952; Del Castillo and Katz, 1954). Since then various techniques have been used to assay exocytosis. The fusion of individual vesicle membranes has been examined by the measurement of rapid increases in membrane capacitance (membrane surface area) during stimulated secretion in adrenal chromaffin cells (Neher and Marty, 1982). More detailed kinetics of the fusion event, especially the opening of the fusion pore marking the first aqueous contact between vesicle interior and cell exterior, were resolved by patch-clamp techniques during stimulated secretion in mast cells (Fernandez et al., 1984; Zimmerberg et al., 1987; Breckenridge and Almers, 1987; Spruce et al., 1990), in neutrophils (Nusse and Lindau, 1988; Gillis et al., 1991), and during viral-mediated cell-cell fusion (Zimmerberg et al., 1994). The quantal release of vesicular contents upon stimulation has also been observed by simultaneous capacitance measurements and amperometry (Chow et al., 1994; Zhou and Mislner, 1995; Albillos et al., 1997) and by confocal laser scanning microscopy (Ryan et al., 1997).

The first attempt to image single vesicle exocytosis was performed with TIR-FM on chromaffin cells. However, the sudden disappearance of secretory granules did not prove that exocytosis had, in fact, occurred. Exocytosis could not be distinguished from rapid movement out of the evanescent field or photolysis of the loaded granules (Lang et al., 1997). Only by combining TIR-FM

with capacitance measurements, was it shown that the abrupt disappearing of the granule coincided with a jump in capacitance (Steyer et al., 1997).

All eukaryotic cells deliver newly synthesized proteins to the plasma membrane and external medium, a process called constitutive exocytosis. The inability to trigger this process has made it difficult to assay single fusion events with the plasma membrane. Previously, GFP-chimera of secreted membrane proteins were used to follow the kinetics of the secretory cargo moving through a living cell (Presley et al., 1997). Laser scanning confocal microscopy has been used to demonstrate that the rate of secretion through the constitutive secretory pathway follows simple first order kinetics (Hirschberg et al., 1998). Potential fusion events of post-Golgi carriers have been visualized by time-lapse epifluorescence microscopy. However, a more sensitive and quantitative assay is required to distinguish fusion from either movement out of the focal plane or photolysis of the carriers.

In this study, we used TIR-FM to acquire high-resolution video-rate images of the fusion of single constitutive secretory carriers with the plasma membrane. TIR-FM has been used previously to image the release of soluble vesicular contents (acridine orange) during regulated exocytosis of chromaffin cell granules (Steyer et al., 1997). However, the contents diffuse very quickly into the 3 dimensional extracellular space, often in less than one image frame (Fig. 3.1, top). To be able to quantitatively analyze constitutive exocytosis, we made two modifications to improve the resolution. First, we examined the delivery of a membrane protein to the plasma membrane rather than the luminal contents of a secretory vesicle (Fig. 3.1, bottom). While soluble cargo (red) is rapidly discharged, a membrane protein (green) should diffuse considerably more slowly in the plane of the plasma membrane, giving time to resolve the dispersal of the cargo molecule. Second, we used a high N.A. lens to perform objective-type TIR-FM on living cells (Steyer et al., 1997). In contrast to the traditional approach of using a prism to couple the exciting beam at a super-critical angle to the interface, a high N.A. lens (N.A.= 1.65 or 1.45) is used to deliver the exciting beam, which results in a substantial increase in light collection.

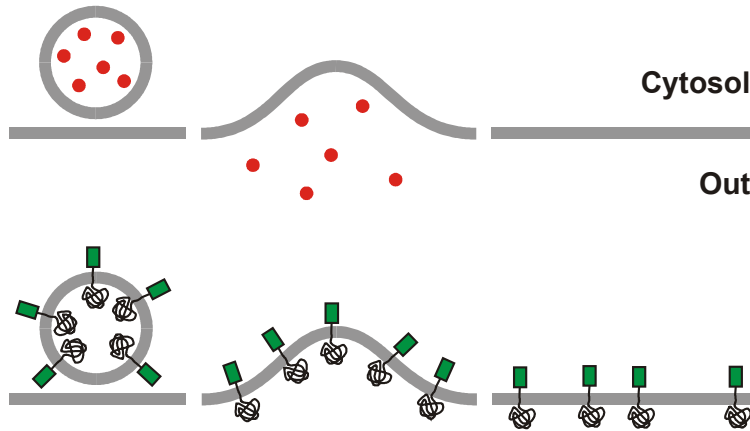


Figure 3.1. Schematic exocytosis of luminal and membrane-bound cargo.

A luminal marker (red) is expelled into the extracellular space, while membrane-bound cargo (green) diffuses laterally into the plasma membrane during exocytosis. We used biosynthetic proteins tagged with GFP on the cytoplasmic side (green box) as reporters to image the flattening of the vesicle and the spread of the membrane protein into the plasma membrane.

Using TIR-FM and a GFP-tagged membrane protein as reporter we followed the kinetics of fusion with a time resolution of 30 frames/sec. Quantitative analysis showed that carriers undergoing fusion can be easily distinguished from carriers moving perpendicularly to the plasma membrane. The flattening of the carriers into the plasma membrane is seen as a simultaneous rise in total, peak and width of the fluorescence intensity. The duration of this flattening process depends on the size of the carriers, distinguishing small spherical from large tubular carriers. The data support the proposal that long tubular structures contribute to transport from the Golgi to the cell surface (Hirschberg et al., 1998; Toomre et al., 1999). Quantifying the spread of the membrane protein into the plasma membrane showed that the cargo is freely diffusive upon fusion.

3.2. Results

In our initial approach to image constitutive exocytosis we used the temperature sensitive folding mutant ts045 of the vesicular stomatitis virus glycoprotein (VSVG) (Wehland et al., 1982), with the green fluorescence protein (GFP) fused to its cytoplasmic tail (VSVG-GFP) as a reporter (Presley et al., 1997; Toomre et al., 1999). This mutant is retained in a misfolded form in the ER at 40°C, but upon shifting to 32°C, moves synchronously to the Golgi, from where it is transported to the plasma membrane. We chose ts045 VSVG-GFP for our initial experiments because, after releasing the 40°C block, highly fluorescent post-

Golgi carriers could be easily detected with current microscopic techniques (Hirschberg et al., 1998). In this study, VSVG-GFP was transiently expressed and accumulated in the ER of COS cells and its delivery to the plasma membrane was imaged shortly after shifting to 32°C. Further experiments using other proteins, in combination with a Golgi exit block at 20°C, showed that the method for the detection of single fusion events is applicable for a wide variety of membrane proteins (see Chapters 4, 5 and 7).

Studying delivery of a membrane protein offered a number of advantages over delivery of a luminal marker. As mentioned earlier, the use of a GFP-labeled membrane protein should allow us to temporally resolve the dispersal of the membrane protein from the site of fusion. Second, the concentration of membrane-permeant luminal fluorophores, such as acridine orange, is sensitive to changes in the vesicle lumen. In our experiments, the concentration of the fluorophores remains constant in each carrier since the GFP is synthesized as part of a membrane protein. Third, the fluorescence of luminal fluorophores is sensitive to physiological changes inside the vesicle, such as pH. The GFP fluorophores in our experiments were synthesized on the cytoplasmic side of the VSVG and therefore were unaffected by changes inside the vesicles. Finally, by quantitatively demonstrating that the fluorescence of a membrane-bound GFP in a carrier is delivered to the plasma membrane, we could ensure that we were monitoring fusion of the carrier and not lysis or movement out of either the plane of focus or the evanescent field.

3.2.1. Post-Golgi carriers at the plasma membrane are imaged in TIR-FM with high signal to background ratio

A cell transfected with VSVG-GFP was imaged with both epifluorescence microscopy and TIR-FM (Fig. 2.2, top left). Under epifluorescence microscopy, the entire cell was visible, with a particularly strong signal in what is probably the Golgi complex. In TIR-FM, the excitatory evanescent field decays exponentially from the cover slip over ~70 nm (methods). The Golgi complex was not visible, indicating that it was far enough away from the coverslip to be outside the evanescent field (Fig. 2.2, top right). Instead, discrete fluorescent spots were

observed which exhibited various morphologies, ranging from small spherical to large tubular structures that can be up to many microns long (Hirschberg et al., 1998; Toomre et al., 1999). In this study we refer to these as carriers, independent of their morphology.

3.2.2. Possible post-Golgi carrier dynamics in TIR-FM

In simple terms, one can imagine three different types of carrier dynamics occurring in TIR-FM (Fig. 3.2). In the first case, a carrier moves in and out of the evanescent field (Fig. 3.2a). This would result in an increase and decrease of the total fluorescent intensity. Since the focal depth of the objective is large compared to the depth of the evanescent field, the area $[(width)^2]$ of the carrier fluorescence should not change much. Another possibility is that the carrier membrane lyses as a result of photochemical/phototoxic⁵ reactions (Fig. 3.2b). In this (hypothetical) case, the total intensity should rapidly decrease while bits of the carrier membrane are dispersed into the cytoplasm into areas outside of the evanescent field. The width would probably increase very transiently during the rapid dispersion, and then become very noisy due to the loss of the carrier. In contrast, the fluorescence intensity of a fusing carrier should show a characteristic behavior (Fig. 3.2c). During the approach toward the plasma membrane, both total and width of the fluorescence intensity would be indistinguishable from the initial phase in (A) and (B). During fusion, however, when the carrier membrane flattens down into the plasma membrane, more fluorophores move into the stronger region of the evanescent field. Therefore, we would observe an additional rise in total fluorescence intensity. Simultaneously, there should be an increase in the width of the fluorescence intensity because the diffusive membrane protein would spread laterally into the plasma membrane. We will see in the following paragraphs that our data is consistent with scenarios illustrated in (A) and (C).

⁵ Biomolecules can be damaged by absorption of intense light, a process which is not fully understood, but which can lead to the disruption of membranes (Lock and Friend, 1986).

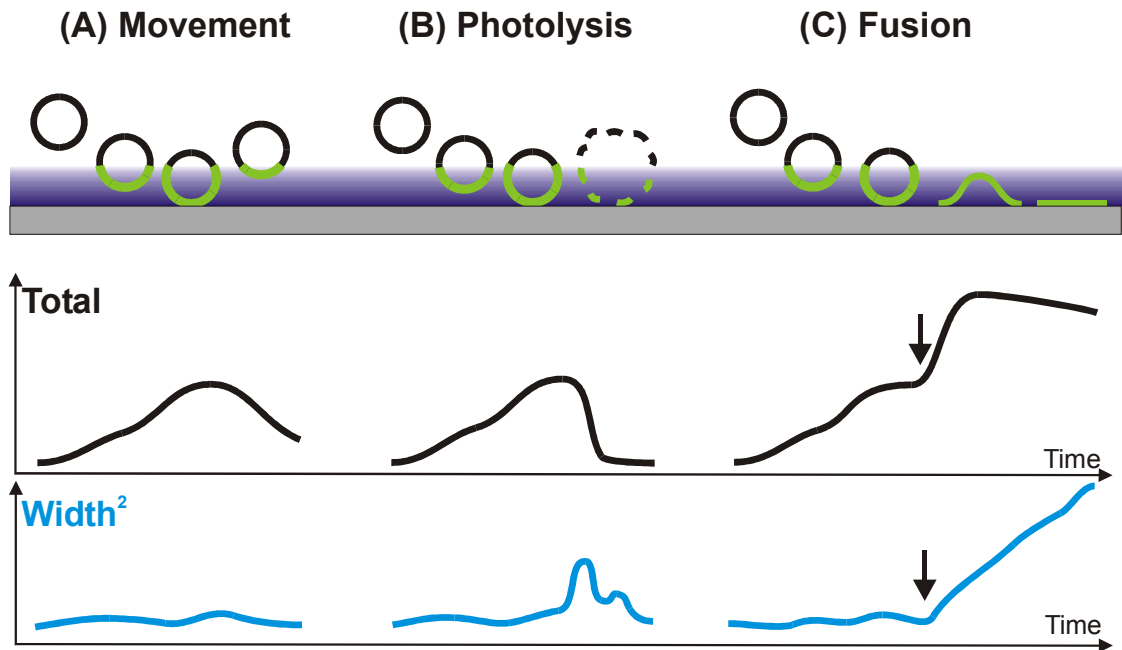


Figure 3.2. Possible scenarios of post-Golgi carrier dynamics in the evanescent field. (A) Movement in and out of the evanescent field. (B) Photolysis. (C) Fusion. For each scenario, the total and width² of the fluorescence intensity is shown qualitatively. Note that only during fusion (arrow) does the width² increase simultaneously with the total intensity of the fluorescence.

3.2.3. Quantitative characterization of post-Golgi carrier dynamics in TIR-FM

COS cells expressing ts045 VSVG-GFP were imaged in TIR-FM at 30 frames/sec. About 20min after the release of the ER-exit block (methods) post-Golgi carriers were observed at the cell surface. Each of these carriers was characterized by its movement, total intensity, peak intensity, and the width of its intensity profile. Changes of the fluorescence intensity were the consequence of the fluorescent cargo moving relative to the coverslip, thereby changing the excitation by the evanescent field. Photobleaching was negligible on this time scale (measured to be only ~0.1% per frame).

The carriers that we imaged fell into three groups (see video 3.3). Some carriers stopped moving and remained stationary adjacent to the membrane (or were stationary during the entire observation period). These are carriers that we believe “docked”, but did not fuse, during the one-minute observation period.

The second group of carriers showed synchronous increases and decreases in the total and peak intensities with no significant change in the width (Fig. 3.3a, c). Most of these carriers also moved in the image plane while these changes in fluorescence intensity occurred. We believe that these carriers moved in and out of the plane of the evanescent field without fusing with the membrane. In conventional epifluorescence the observed width of a fluorescent object widens as it moves out of the plane of focus, which was not observed with these carriers. This is the consequence of the narrow depth of the evanescent field in TIR-FM (50–90nm for 100x 1.65 NA), which is significantly smaller than the depth of field of the objective (~300nm). Thus the fluorophores are never excited outside of the plane of focus.

The third group of carriers moved along curvilinear paths in the image plane and stopped for a variable time (~15sec) before they showed a synchronous increase in the total, peak and width of the fluorescence (Fig. 3.3b, d). If a carrier fuses with the plasma membrane, the total intensity should increase as the vesicle flattens to the membrane (moving the fluorophores into the evanescent field), while the width should increase as the VSVG-GFP diffuses laterally into the membrane. Therefore, we believe these carriers have fused to the plasma membrane. Selected temporal frames are shown for such a fusing carrier (Fig. 3.3d). The total intensity, peak intensity, and $(\text{width})^2$ of the fluorescence for this fusion event are plotted as a function of time (Fig. 3.3b). This data allows us to clearly distinguish three temporal phases, which we label stationary, rise and spread. During all three phases, the center of mass of the carrier was tracked to account for lateral movements, which were on average less than one pixel per frame.

Stationary phase: During this phase, the total intensity, the peak intensity and the width were constant. The fact that the total and peak intensity were constant suggests there was no detectable movement of the carrier perpendicular to the evanescent field. Further, the fact that the width remained constant indicates that the VSVG-GFP was not spreading into the plasma membrane. Therefore, the stationary phase probably represents a vesicle that

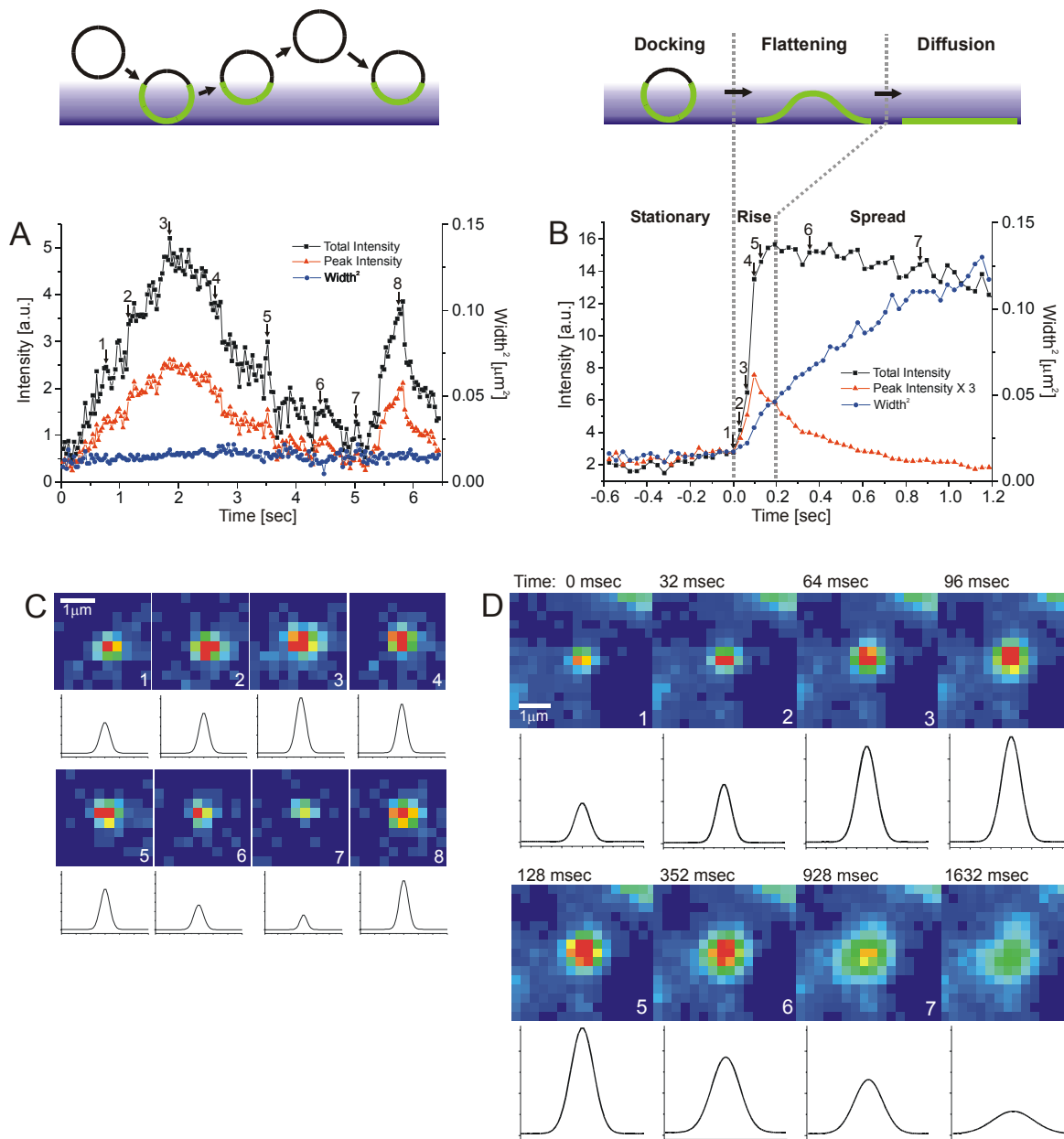


Figure 3.3. Comparison of a carrier moving perpendicular to the plasma membrane and a carrier fusing to the plasma membrane (see videos). The VSVG-GFP fluorescence was imaged in TIR-FM (30 frames/sec). Selected frames are shown for a carrier which moved perpendicular to the coverslip, without fusing to the plasma membrane (C) and for a carrier which fused to the plasma membrane (D). The intensity of the VSVG-GFP is shown in pseudo-color. Each sequence was processed with a running average in time of (+/- one frame) and thresholded separately to aid visualization. The radially symmetric Gauss fit of the carrier fluorescence is shown below each frame. In (A) and (B), the total intensity, peak intensity and the square of the Gaussian width of the carrier fluorescence is shown over time. The arrows indicate the frame numbers. In (B), the three phases: stationary (docking), rise (flattening) and spread (diffusion), are indicated. The fusion start ($t = 0.0\text{sec}$) is defined as the start of the rise phase.

was "docked" or "tethered" close to the plasma membrane. Occasionally a slight increase in total and peak intensity was evident just before the rise phase (data not shown). This may correspond to a movement of the carrier towards the plasma membrane before fusion. The duration of the stationary phase was measured to be ~15sec (see Chapter 4 for more details).

Rise phase: During the second phase, total and peak intensity rose rapidly and the (width)² began to increase in a roughly linear fashion (Fig. 3.3b). Importantly, the increase in all three values was simultaneous for all analyzed fusion events (n>100). The increase in width indicates that the VSVG-GFP was diffusing into the plane of the plasma membrane. The increase of total fluorescence (average of 4.6 +/- 2.0 fold, n=16) implies the fluorescent cargo was moving towards the coverslip, where the evanescent field was stronger. This increase in total intensity is expected when a spherical vesicle containing a membrane marker flattens down into the plasma membrane. Since the evanescent field decays exponentially with distance into the cell, the total intensity of a stationary spherical vesicle ($\mathbf{TI}_{\text{spherical}}$) at the plasma membrane must be lower than the total intensity of the same vesicle after flattening down into the plasma membrane ($\mathbf{TI}_{\text{flat}}$). In the latter case it forms a disk in the plane of the plasma membrane with an area identical to that of the vesicle surface (for simplicity ignoring the lateral diffusion of the membrane protein). The magnitude of this intensity increase can be described by the ratio $\mathbf{TI}_{\text{flat}}/\mathbf{TI}_{\text{spherical}}$, which is independent of the position of the plasma membrane in the evanescent field. For a 250nm spherical vesicle with the fluorophore uniformly distributed over the membrane and using an evanescent decay length of 50-90 nm (the estimated decay length in our experiments), the calculated ratios are between 2.7 and 5.0 (methods). Most experimental values obtained for the ratio $\mathbf{TI}_{\text{flat}}/\mathbf{TI}_{\text{spherical}}$ for events with short rise times (<200ms) are within this range (average of 16 events = 4.6 +/- 2.0). We conclude that the rapid increase of the total intensity indicates the flattening of the carrier membrane into the plasma membrane.

Spread phase: During the third phase, the total intensity remained relatively constant, the peak intensity decreased exponentially, and the width squared

increased linearly. The observation that the total intensity remained at a plateau indicates that the fluorescence within the region of interest was conserved: fluorophores were neither moving closer to or further away from the coverslip. The subsequent slow decrease of the total intensity in this phase is probably due to photo-bleaching (measured at ~0.1% per frame) and diffusion of VSVG-GFP out of the region used for the analysis. The exponential decay of the peak intensity together with the increase in width can be explained by the spread of the VSVG-GFP into the plasma membrane upon fusion. If the spread of the VSVG-GFP into the membrane was diffusive then the $(\text{width})^2$ should increase linearly (Crank, 1995). Potential deviations from simple diffusion would contribute nonlinear terms. The width of the fluorescence was analyzed for 28 fusion events from seven different cells. The data could be fit to a straight line with a correlation coefficient (r^2), which ranged from 0.96 to 0.996. Thus, our subsequent analysis assumed that the dominant behavior was diffusive [$(\text{width})^2$ increased linearly over time], yielding an average diffusion constant of $(11.0 \pm 0.5) \times 10^{-10} \text{ cm}^2/\text{s}$. A diffusion constant of VSVG in the plasma membrane was previously reported to be $(3.8 \pm 1.8) \times 10^{-10} \text{ cm}^2/\text{s}$ using FRAP (fluorescence recovery after photo bleaching) measurements on fluorescently labeled Fab fragments bound to VSVG (Zhang et al., 1991). There are a few possible explanations for the ~2-fold difference between the two values. First, the attachment of Fab fragments to the VSVG could slow down the mobility. Second, the diffusion constant may be temperature-sensitive. The FRAP experiments were performed at room temperature whereas our measurements were at 32°C. Third, the mobility of newly delivered membrane proteins may be different from those that have been resident in the membrane. Finally, the photobleaching involved in FRAP may induce changes in the membrane that slow the subsequent diffusion.

3.2.4. The ‘rise time’ is characteristic of the carrier morphology

In addition to the fusion events with short rise times (Fig. 3.3b,d and 3.4c), we observed two other types of fusion events. First, a small fraction of the events with short rise times had widths that increased at a slower than linear rate. This

may be the consequence of a variable distance between the coverslip and the plasma membrane. In certain areas, the cell membrane buckled away from the coverslip. This was seen in TIR-FM pictures of cells that were surface-labeled with a membrane marker (data not shown). A fusion event occurring at the edge of such a buckle, therefore, would deliver at least part of its fluorescent cargo into a region of the plasma membrane that is in a weaker part of the excitation field.

Second, there were events with significantly longer rise times, which were associated with tubules. The carriers in the short-rise-time events described above appeared as fluorescent spots close to the plasma membrane. In some cases, however, the carriers appeared as tubules moving in and out of the evanescent field, as indicated by the intensity changes along their length (Fig. 3.4a). The fusions of tubules to the plasma membrane were similar to the short-rise-time events, with stationary, rise and spread phases. However, these tubules were different in a few characteristics. At the beginning of the rise phase, the tubules rounded up to a spot ($n > 10$) (Fig. 3.4a, frames at $t = 0.0$ sec and 0.1 sec). This accounts for the drop in the width of the fluorescence at the beginning of the rise phase (Fig. 3.4b). For these tubular carriers, the rise phase lasted substantially longer (> 1 s) than the rise phase of the short-rise-time carriers (compare Fig. 3.4b with 3.4c and 3.3b). The peak fluorescence intensity was approximately the same for both types of carriers. However, the total fluorescence intensity delivered by a tubule was up to 25-fold greater. Further, the total fluorescence continued to increase even after the peak fluorescence reached its maximum (Fig. 3.4b). This suggests there was a sustained delivery of fluorescent membrane protein into the evanescent field.

Some carriers that appeared as spots also exhibited long rise times (data not shown). These may have been tubules oriented perpendicular to the membrane. Consistent with this interpretation, carriers that had long rise times also continued to increase their total fluorescence after the peak fluorescence was reached and delivered a greater total amount of fluorescence to the membrane. For one particular cell, the carriers that had a rise time of > 1 sec represented 21% of all the events we observed ($n = 96$), but they accounted for 59% of the total

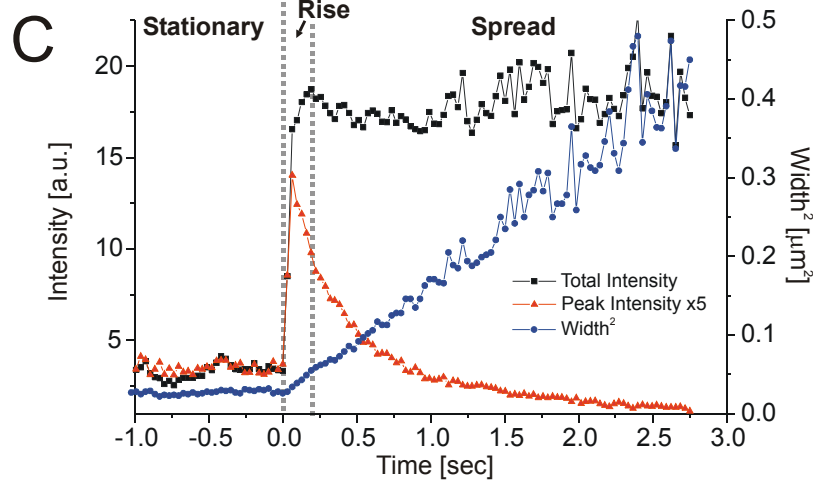
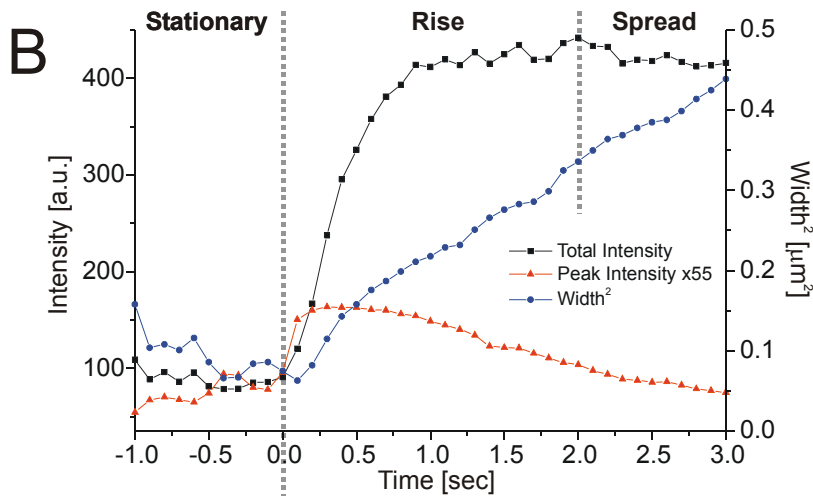
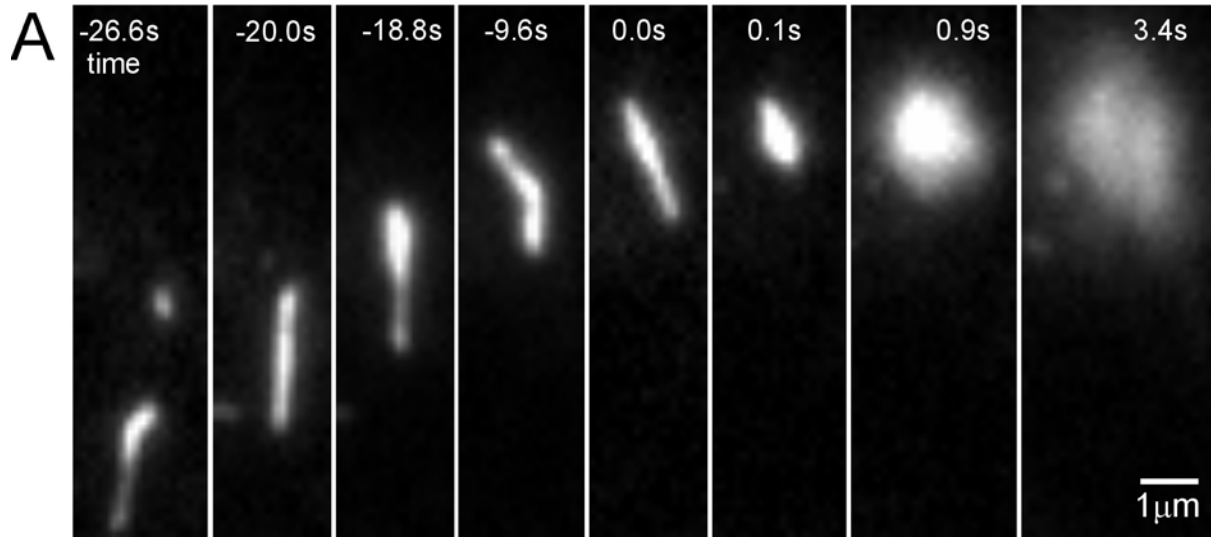


Figure 3.4.

(A) Transport, docking and fusion of a large tubular carrier (see video). The fusion start ($t = 0.0\text{sec}$) is defined as the start of the rise phase.

(B, C) Carrier fusion events with different rise times. Total intensity, peak intensity and square of the Gaussian width were plotted on the same time axis for carriers with long rise time (B, $\sim 1.9\text{sec}$, long tubule from A) and short rise time (C, $\sim 160\text{msec}$, spot-like morphology). The three phases: stationary, rise and spread, are indicated.

fluorescence intensity (Table 3.1). This is consistent with a model in which the longer rise times result from the fusion of larger carriers (tubules), which deliver a larger amount of VSVG-GFP to the plasma membrane.

In this chapter I described the establishment of a method for the quantitative detection of single fusion events of post-Golgi carriers. This provides a tool for the localization of constitutive exocytosis. Consequently, we are equipped to address further questions: Where on the cell surface does fusion occur in polarized cells, such as migrating fibroblast and polarized epithelial cells? Is there domain-specific targeting in any of these cases? Further, the observation that post-Golgi carriers are transported along curvilinear paths close to the plasma membrane just before fusion leads to the question: What cytoskeletal component is involved in transporting the carriers during exocytosis?

Table 3.1: Statistics of Rise Time and Total Delivered Fluorescence Intensity.

Rise Time	< 200ms	200ms – 1sec	> 1sec
% of total events (n=130, 7cells)	31	48	21
% of total fluorescence intensity delivered (n=96, 1cell) ⁶	11	30	59

⁶ Since the total fluorescence intensity delivered to the plasma membrane is difficult to compare between different experiments because of variations in the evanescent field intensities, the percentage (%) of the total intensity are calculated from a single cell experiment (96 fusion events).

4. Role of Microtubules in Delivery and Fusion of Post-Golgi Carriers in Fibroblasts

4.1. Introduction

The role of microtubules (MTs) in the transport of secretory cargo from the sites of synthesis in the ER to the sites of exocytosis at the plasma membrane has been a long-standing question in cell biology (Bloom and Goldstein, 1998). MTs are involved in the transport of membrane cargo carriers from the ER to the Golgi as well as from Golgi/TGN to the periphery of the cell in mammalian fibroblasts (Lippincott-Schwartz et al., 2000). However, it remains unclear what, if any, cytoskeletal elements are involved in the transport in the periphery of the cell, just before the fusion of the post-Golgi transport carriers with the plasma membrane (Fig. 4.1). In regulated exocytosis the actin cytoskeleton is thought to be involved in the capture and/or the short-range transport of secretory vesicles at the plasma membrane, suggesting cooperation of the microtubules and the actin cytoskeleton in exocytosis (Lang et al., 2000; Rudolf et al., 2001). The role

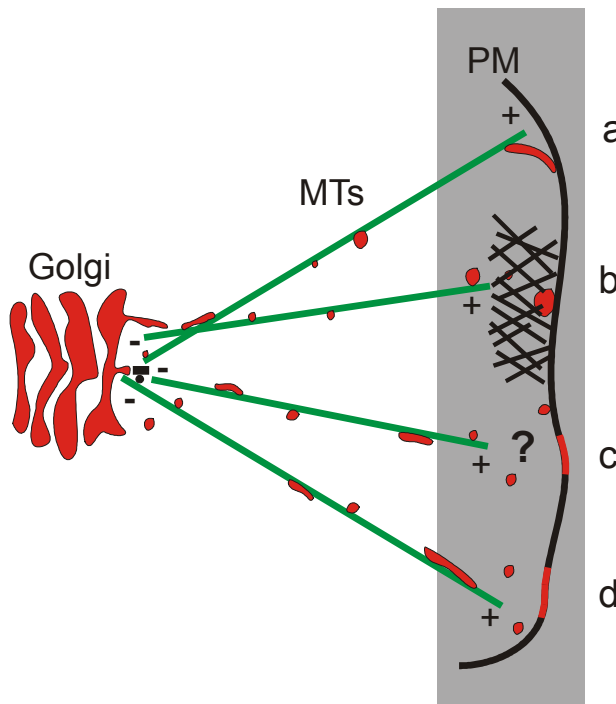


Figure 4.1. Possible scenarios of post-Golgi carrier transport close to the plasma membrane.

The Golgi membrane cargo (red), the MTs (green) and the plasma membrane (black) are illustrated. Possible scenarios in final delivery of post-Golgi membrane cargo are:

a) directly via MTs, b) filamentous actin functions either as a transport medium or as a barrier, or both, c) some unknown steps occur, d) detachment from MTs and random diffusion.

of MTs in post-Golgi traffic has been tested with various reporter proteins fused to GFP. In Vero cells, the directed transport of secretory vesicles containing human chromogranin B from the Golgi/TGN to the cell periphery was found to be blocked by treatment with the MT-depolymerizing agent nocodazole. However, overall secretion from the Golgi/TGN to the surface was only diminished, but not blocked (Wacker et al., 1997). Similarly, the saltatory motion of post-Golgi carriers labeled with VSVG-GFP was stopped after treatment with nocodazole, but the rate of bulk delivery from TGN to plasma membrane was found to be unchanged compared to untreated cells (Hirschberg et al., 1998). Further, post-Golgi traffic of another reporter, p75-GFP, was completely inhibited by injecting a function-blocking antibody against kinesin into sparsely seeded MDCK cells (Kreitzer et al., 2000). Additionally, using sequential dual-color epifluorescence microscopy, some post-Golgi carriers loaded with VSVG-GFP were seen to track along MTs in PtK₂ cells (Toomre et al., 1999). These data suggest on one hand that the MT cytoskeleton facilitates the delivery of post-Golgi cargo to the plasma membrane, but on the other hand that MTs are not absolutely required for post-Golgi traffic in fibroblasts.

A number of studies have implicated a role of the cortical actin cytoskeleton in regulated exocytosis. In neurons the synaptic vesicles are embedded, via synapsin, in a meshwork of actin (Humeau et al., 2001). In PC-12 cells, the motility of secretory granules was found to be both hindered as well as mediated by the actin cytoskeleton (Steyer and Almers, 1999). The secretory granules are thought to undergo a maturing process while trapped in the actin cortex (Rudolf et al., 2001). Inhibitors of myosin light chain kinase can block mobilization of the reserve pool in neurons (Ryan, 1999). In constitutive exocytosis myosin II was involved in the production of transport vesicles from the TGN (Musch et al., 1997). However, the role of actin in the final delivery of constitutive post-Golgi cargo has not been studied.

We showed in Chapter 3 that post-Golgi carriers labeled with a GFP-tagged membrane protein, upon reaching the cell periphery, move within ~100nm of the plane of the membrane for distances of microns prior to fusion. The goals of the

study presented in this chapter were to examine this final step in membrane transport and address the questions:

- Which cytoskeletal components (MTs or actin) are responsible for this transport prior to fusion with the plasma membrane?
- Are post-Golgi carriers transported to specific domains or sites of fusion at the plasma membrane?
- If so, what are the physiological consequences for this behavior? For example, migrating fibroblasts are proposed to have a mechanism for directly inserting secretory membrane cargo into their leading edge (Bergmann et al., 1983). If this is true, does the cytoskeleton contribute to polarized exocytosis?
- How does the distribution of the fusion sites alter upon disruption of the relevant cytoskeletal component?

To address these questions we used TIR-FM, which has been used to image the final step of the constitutive secretory pathway (Chapter 3). As detailed in the previous chapter we have established a quantitative assay to identify single fusion events, in contrast to most assays measuring bulk secretion. This allowed us to study the spatial and temporal distribution of single post-Golgi carriers fusing with the plasma membrane.

Nuclear microinjection of cDNA was used to allow a synchronized synthesis of the low density lipoprotein receptor (LDLR) or the neurotrophin receptor (p75), both fused to GFP, as reporters for post-Golgi traffic (Fig. 4.2) (Kreitzer et al., 2000). After microinjection, expression of the reporters was allowed at 37°C for ~1hr (“pulse”). Then, protein synthesis was inhibited and the already synthesized proteins were accumulated in the Golgi/TGN at 20°C for ~3hr (“chase”). Upon shift to 32°C the Golgi/TGN block was released and the markers moved synchronously in post-Golgi carriers to the plasma membrane. This way, the delivery of post-Golgi carriers to the cell surface could be observed with high signal-to-background ratio in TIR-FM. In our previous study we used a temperature sensitive folding mutant of VSVG, which accumulates in the ER at the restricted temperature (Chapter 3). We preferred the method of microinjection

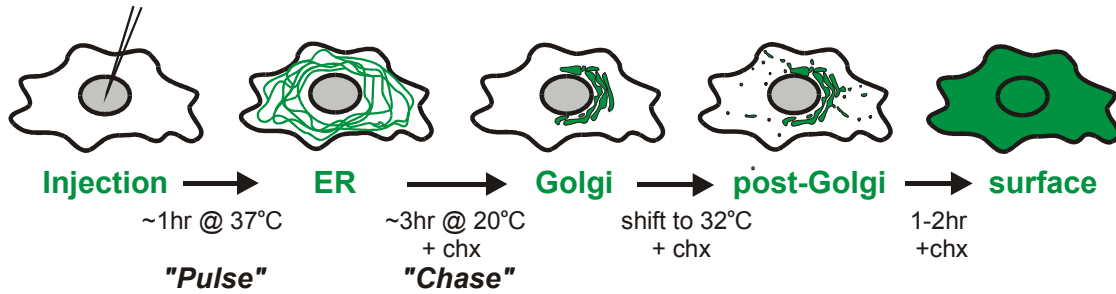


Figure 4.2. Pulse-chase of secretory membrane cargo by nuclear microinjection and Golgi exit block. cDNAs of the membrane proteins are microinjected into the nucleus and expression is allowed for ~1hr at 37°C ("pulse"). Further protein synthesis is then inhibited with cycloheximide. The cells are incubated for ~3hr at 20°C ("chase") to accumulate cargo in the Golgi/TGN. Post-Golgi traffic is imaged after shift to 32°C in the presence of cycloheximide. After 1-2hr all of the cargo is delivered to the cell surface.

and Golgi-block for practical reasons. It requires less than 4h from injection of the cDNA to the start of data acquisition, as compared to transfection of ts045 VSVG, which requires two days between transfection and imaging. Moreover, the method of Golgi-block is not restricted to a specific protein, rather may be applied to any secreted protein. The MT cytoskeleton was labeled using GFP-chimera of either β -tubulin or the neuronal MT-associated protein, tau.

Applying dual-color TIR-FM, we show that post-Golgi cargo is transported via MTs to the sites of fusion at the plasma membrane. The spatial distribution of fusion sites in single fibroblasts was mapped, revealing that migrating cells exhibit polarized exocytosis close to the leading edge. A comparison of transport behavior in cells with intact MTs versus cells with disrupted MTs provides evidence for the necessity of MTs in domain-specific delivery of post-Golgi cargo. Further, we show that inhibition of myosin-II and -V ATPases with 2,3-butanedione-monoxime (BDM) or the depolymerization of the filamentous actin with cytochalasin-D slightly shorten the "docking" time before fusion but do not otherwise affect transport and fusion dynamics of constitutive post-Golgi carriers.

4.2. Results

4.2.1. Peripheral MTs can be visualized within ~100nm from the plasma membrane using TIR-FM

To visualize single microtubules at the cell surface we used nuclear microinjection of cDNA encoding either β -tubulin or tau, a neuronal MT-associated protein, both fused to GFP. In the case of GFP- β -tubulin, we saw clear MTs at about 24h post-injection in NRK fibroblasts (Fig. 4.3d, e, f). Before that time the background from unincorporated β -tubulin was too high to resolve single MTs (data not shown). In contrast, the fluorescence of tau-GFP yielded a higher signal-to-background image of the MTs (Fig. 4.3a, b, c). Tau-GFP clearly labeled the MT array with a minimal expression time of 60min post-injection. The MT network in NRK fibroblasts expressing tau-GFP at 2h post-injection looked very similar to cells expressing GFP- β -tubulin at 24h post-injection. In epifluorescence, the microtubule-organizing center (MTOC) appears as a very bright area whereas the peripheral MTs are comparably dim. In contrast, in TIR-FM of the same cell there were areas of brighter and dimmer MT tracks, demonstrating that some of the MTs were close enough to the plasma membrane to be within the evanescent field, which in this case had a decay constant of ~125nm. Many MTs were also visible in TIR-FM if the evanescent field was restricted to extend ~70nm from the cover slip (data from using 100x 1.65NA objective, not shown). The variations in fluorescence intensity are due to the distribution of the MTs relative to the coverslip. The distance of the MTs from the coverslip are determined by both the adhesion pattern of the cell, and the three dimensional distribution of the MTs within the cell. The area of the MTOC is dark in the TIR-FM image, showing that the MTOC is outside the evanescent field. The pseudo-color overlay clearly shows that the MTs are imaged with much higher signal-to-background in TIR-FM compared to epifluorescence.

In TIR-FM there are fluorescent tracks that appear to end at points distributed all over the cell surface. From an image at a single time point it cannot be determined if these are MT ends or intermediate parts of the MTs which enter

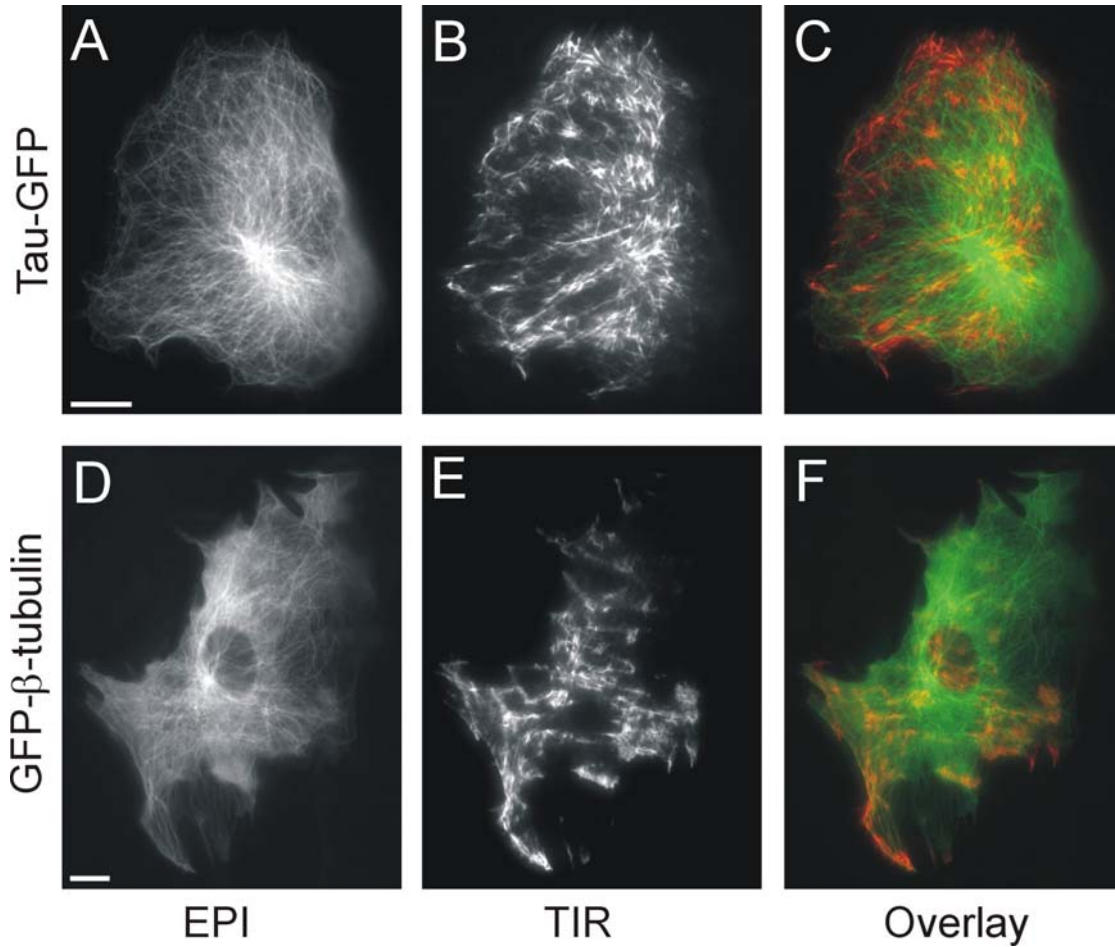


Figure 4.3. MTs imaged in epi- and TIR fluorescence microscopy (see video). NRK fibroblasts were microinjected with cDNA encoding either tau-GFP at 2 h (A, B, C) or GFP- β -tubulin at 24h (D, E, F) prior to imaging in epifluorescence (A, D) and TIR-FM (B, E). Pseudo-color overlays from the images taken in epifluorescence (green) and TIR-FM (red) are shown (C, F). Scale bars = 10 μ m.

and leave the evanescent field. However, in time-lapse TIR-FM (videos 4.3b,e) we observed distinct MTs undergoing phases of growth, shortening and pause, typical of dynamic instability (Mitchison and Kirschner, 1984; Saxton et al., 1984; Schulze and Kirschner, 1986; Sammak and Borisy, 1988). This behavior was observed for MTs labeled with either tau-GFP or GFP- β -tubulin. Further, we confirmed by immunofluorescence, that tau-GFP labels all MTs (Fig. 4.4). Thus, we used tau-GFP as a marker for the MT cytoskeleton in our analysis of post-Golgi carrier traffic.

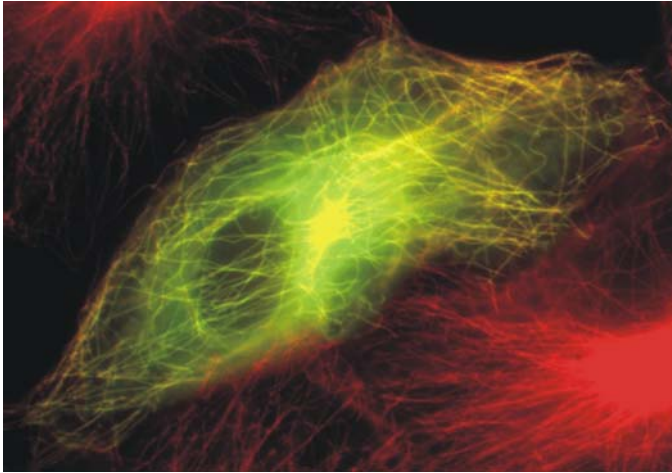


Figure 4.4. Colocalization of tau-GFP with anti- β -tubulin-Cy3.

Cells were injected with cDNA encoding tau-GFP (green), incubated for 2h at 37°C, then fixed and stained with anti- β -tubulin-Cy3 (red). All MTs of the tau-GFP expressing cell are yellow, demonstrating that all MTs are labeled by tau-GFP.

4.2.2. Post-Golgi carriers are transported along MTs to the sites of fusion with the plasma membrane

To characterize the roles of the microtubules in transport, ‘docking’ and fusion of post-Golgi carriers at the plasma membrane, we simultaneously imaged the MT cytoskeleton and membrane proteins as they moved through the biosynthetic pathway. Alternating acquisition of the MTs and the membrane cargo has potential problems of temporal and spatial correlation. Instead we used two approaches to simultaneously image the MTs and the membrane protein cargo. The first approach used two different GFP variants, cyan and yellow fluorescent proteins, to differentially label the MTs and the membrane cargo. Both fluorophores were excited simultaneously and the fluorescence image was split with a dichroic mirror, passed through different emission filters, and then focused side-by-side on the same cooled CCD camera (Chapter 2, methods). The second approach took advantage of the very different temporal dynamics of MT and membrane carrier movements. With TIR-FM at high spatial and temporal (>5 frames/sec) resolution, it is possible to unambiguously characterize single membrane fusion events (Chapter 3). In contrast, most dynamics of MTs are resolved by an acquisition speed of 1 frame/sec or less (Rusan et al., 2001). If it is assumed that all rapidly changing events were due to movement of protein cargo in the carriers and slower changing events were from movement of MTs, then the two can be separated by their temporal properties. This latter approach,

which will be referred to as “temporal pseudo-dual-color”, had the advantage that the full emission spectrum could be collected from the fluorophores. In contrast, the former approach of two different fluorophores did not require assumptions about the temporal behavior of the fluorophores. However, it required polychroic mirrors for excitation and additional dichroic mirrors and narrow bandpass filters to split the emission, which decreased the signal. Both approaches gave indistinguishable results.

To image the MTs and post-Golgi membrane cargo simultaneously, we needed to select reporter proteins, which were synthesized with similar kinetics after microinjection of the cDNAs. As biosynthetic markers we used p75-GFP/YFP or LDLR-GFP, which are both abundantly synthesized within ~1h after microinjection. Since tau-CFP/GFP was synthesized within 1-2 h after injection without showing significant cytoplasmic background, we chose to co-inject the cDNA encoding tau-CFP/GFP, rather than GFP- β -tubulin, together with the cDNA encoding the membrane proteins.

Stable expression of tau in CHO cells moderately affects the plus-end-directed motion of secretory cargo by shortening the run length of vesicles (Trinczek et al., 1999). In our experiments with short-term transient expression of tau-GFP the typical transport of the post-Golgi carriers was not significantly altered. It is likely that the expression level of tau-GFP was low enough in our experiments that potential effects on transport were not detectable.

The overall motion of the carriers labeled with LDLR- GFP/YFP or p75-GFP/YFP observed in TIR-FM in NRK cells was very similar to the motion we previously observed with VSVG-GFP labeled carriers. As characterized in Chapter 3, the motion of the carriers in the periphery of the cell could be classified into a transport phase, a stationary phase and a fusion phase.

Transport phase: Movement of post-Golgi carriers along MTs adjacent to the cell surface.

The ‘temporal’ dual-color visualization of the fast moving carriers together with the much slower moving MTs (methods), demonstrated that the p75-GFP

carriers were transported on curvilinear tracks when in close proximity (<125nm) to the plasma membrane. These tracks appeared spatially coincident with the tau-GFP labeled MTs (Fig. 4.5b). The overall movement of the p75-GFP carriers in cells expressing tau-GFP was qualitatively indistinguishable from the motion of these carriers in cells that were not injected with tau-GFP. The transport of membrane cargo along the MTs occurred in the typical saltatory fashion, alternating between fast and slow movements. The carriers frequently switched between different MT tracks in the dense MT meshwork. Some carriers reached the edge of the cell.

Stationary phase: Docking of post-Golgi carriers along MT tracks.

The transport phase was followed by a stationary phase, during which the carriers did not move in unidirectional fashion and did not leave an area with a radius of ~100nm (methods). The duration of this phase between cessation of directed transport and the start of the fusion, which we will refer to as the 'docking phase', turned out to have a broad distribution with a mean of 15.1 +/- 12.4 sec (n = 57) (Fig. 4.11, top).

Fusion phase: Fusion of post-Golgi carriers along MT tracks.

Many carriers were seen to fuse with the plasma membrane. The criteria used to determine whether a carrier either a) fused to the plasma membrane, b) photolysed or c) moved perpendicular to the membrane have been described previously (Chapter 3). The minimal time resolution needed for the quantitative detection of single fusion events of p75-GFP or LDLR-GFP containing carriers was found to be ~5 frames/sec. For initial experiments on the imaging of constitutive exocytosis using ts045 VSVG-GFP, in contrast, we used the maximal time resolution given by the detection system (30 frames/sec), which limited us to "bin" pixels of the CCD array (2x2 or 4x4 binning, methods). This was necessary initially to establish the quantitative criteria used to distinguish different dynamics of post-Golgi carrier fusion. All criteria still hold at the lower time resolution of 5 frames/sec. One major advantage of lowering the frame rate was the reduction of

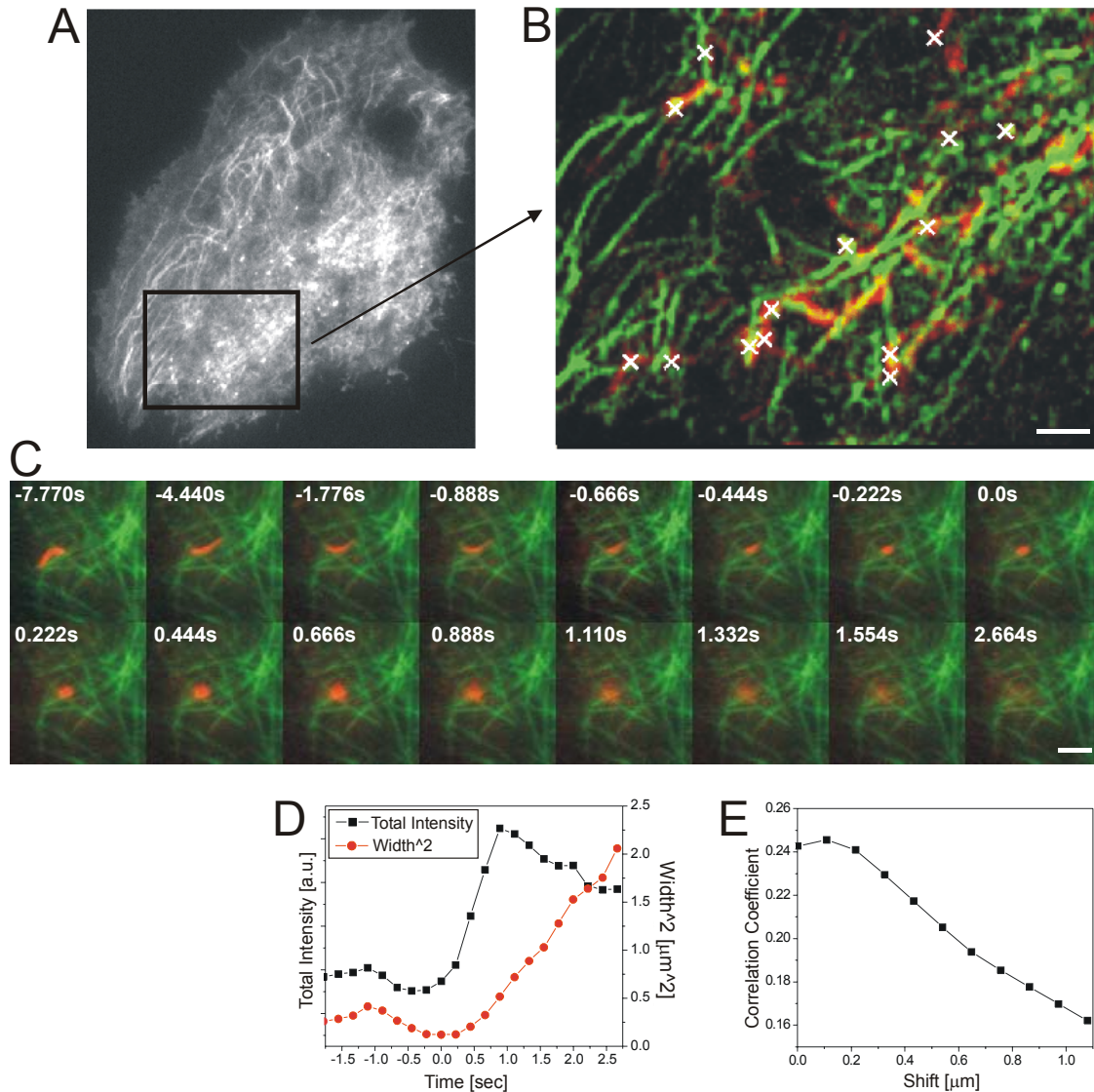


Figure 4.5. Transport, docking and fusion of post-Golgi carriers along the MTs imaged in dual-color TIR-FM (see videos). (A, B) NRK fibroblasts were microinjected with cDNA encoding p75-GFP and tau-GFP and imaged in TIR-FM (~5 frames/sec). The sequence was processed according to the protocol for ‘temporal’ pseudo-color TIR-FM to separate the fast moving carriers from the slow motion of the MT cytoskeleton (methods). A region of the whole cell (A) is shown in (B). To reveal the colocalization of the carrier tracks (red) with the MT tracks (green), the maxima of each pixel for each color channel were merged into a single image (B). The fusion sites are marked as white crosses.

(C) MDCK cells were microinjected with cDNA encoding p75-YFP and tau-CFP and imaged in simultaneous dual-color TIR-FM (~5 frames/sec). The sequence was processed as described, including bleed-through correction and contrast enhancement (methods). A tubular post-Golgi carrier containing p75-YFP (red) is shown to track, collapse and fuse along the MTs (green).

(D) Measured values for the total and the width² of the intensity of the fusing tubular carrier (C). Fusion start ($t = 0.0s$) is defined as the start of the rise in total fluorescence intensity.

(E) To quantify the colocalization of the tubular carrier just before fusion with the MTs, we calculated the average correlation coefficient between both channels for the whole region. To test the quality of correlation, the channels were shifted relative to each other about $\pm 1.1\mu m$ in x- and y-direction in 108nm steps. The resulting values for the correlation coefficient were averaged. Scale bars = $2\mu m$.

imaging data to be stored in memory, which enabled us to image longer intervals during the continuous stream of data to memory.

Using the established quantitative criteria, fusions of carriers containing p75-GFP were mapped on the plasma membrane of NRK fibroblasts (Fig. 4.5b). Within our optical (lateral) resolution ($\sim 250\text{nm}$) and temporal resolution ($\sim 200\text{ms}$) the center of the fusions colocalized with the MT tracks. The MT fluorescence signal at fusion sites ($n=20$) was ~ 50 times higher than the background (methods). This is consistent with colocalization of the MTs and fusion sites and with the possibility that the carriers do not leave the MT tracks before they reach their site of fusion.

As an independent test of the result obtained by temporal pseudo-dual-color imaging, the experiments were repeated with simultaneous dual-color TIR-FM in cells expressing tau-CFP to label the MTs, and p75-YFP to label the post-Golgi carriers. Since this approach required narrowing the ranges of fluorescence emissions collected, the signals were weaker compared to the imaging of single fluorophores. To still be able to monitor fusion in simultaneous dual-color, we chose MDCK cells expressing p75-GFP, in which many of the post-Golgi carriers are in fact highly fluorescent tubules which can be up to many microns long (Kreitzer et al., 2000). We clearly observed some carriers moving and fusing along MT tracks. One tubular carrier loaded with p75-YFP is shown tracking along the continuous MT meshwork (Fig. 4.5c). It bends while switching tracks, moves back a small distance, until it collapses and fuses along the MT track. The quantification clearly shows the simultaneous rise of total and width² of the fluorescence intensity characteristic for all fusion events (Fig. 4.5d). The dip in the width² just before fusion start indicates the collapse of the membrane tubule. To test for colocalization of the fusing carrier with the MT track, we performed a spatial cross-correlation analysis between the carrier and the MT channel just before fusion (methods). The radially averaged correlation coefficient clearly shows a peak at zero-shift between the two channels within $\pm 100\text{nm}$ (Fig. 4.5e). These data confirm the observation obtained by temporal pseudo-dual-color TIR-FM that post-Golgi carriers fuse along MT tracks.

4.2.3. Post-Golgi carriers can remain bound to the MTs during fusion and are seen to fuse in multiple steps

Post-Golgi carriers are seen in a distribution of shapes from spheres to elongated tubules. Using VSVG-GFP as membrane cargo expressed in COS-1 cells, it was shown that tubular post-Golgi carriers undergo a rapid shortening, or 'collapse', of the tubular morphology shortly before, or at the onset of dispersal of the cargo into the plasma membrane (Fig. 3.4a). This 'collapse and fusion' of tubular carriers was subsequently observed in various cell types (NRK fibroblasts, sub-confluent MDCK cells) using different membrane cargo (LDLR-GFP, p75-GFP). It was always seen when the tubule was oriented parallel to the plasma membrane (coverslip) in the evanescent field, such that the tubular morphology was clearly resolved. Such 'collapse and fusion' events were most easily observed in MDCK cells expressing p75-GFP because many of the post-Golgi carriers are highly fluorescent tubules. Two examples of collapse and fusion events of tubular carriers are shown in single-color (Fig. 4.6a) as well as dual-color TIR-FM (Fig. 4.5c). The critical parameters describing the collapse and fusions are quantified (Fig. 4.6c and 4.5d). For example, in the single-color fusion (Fig. 4.6a, c), the start of the carrier flattening into the plasma membrane is indicated by the increase in total fluorescence intensity (time = 0.00sec). The start of the increase in width² of the fluorescence intensity is slightly delayed (time = 0.44sec), indicating the collapse of the tubular carrier. Importantly, tubular carriers and their collapse and fusion into the plasma membrane, was never observed in cells with disrupted MTs. This suggests strongly, that the tubular morphology is due to the attachment of the carriers to the MT.

The amount of tubular carriers observed varies greatly between cell types and constructs. In NRK fibroblasts, we mostly observed vesicular post-Golgi carrier fusing with the plasma membrane. In ~87% of all analyzed fusion events (n=534, 8 NRK cells) all the cargo was delivered into the plasma membrane in a single step, a process we will call complete fusion. The remaining ~13% of fusions occurred in multiple steps: only a part of the cargo was dispersed into the plasma membrane in each step, leaving a significant amount of fluorescence

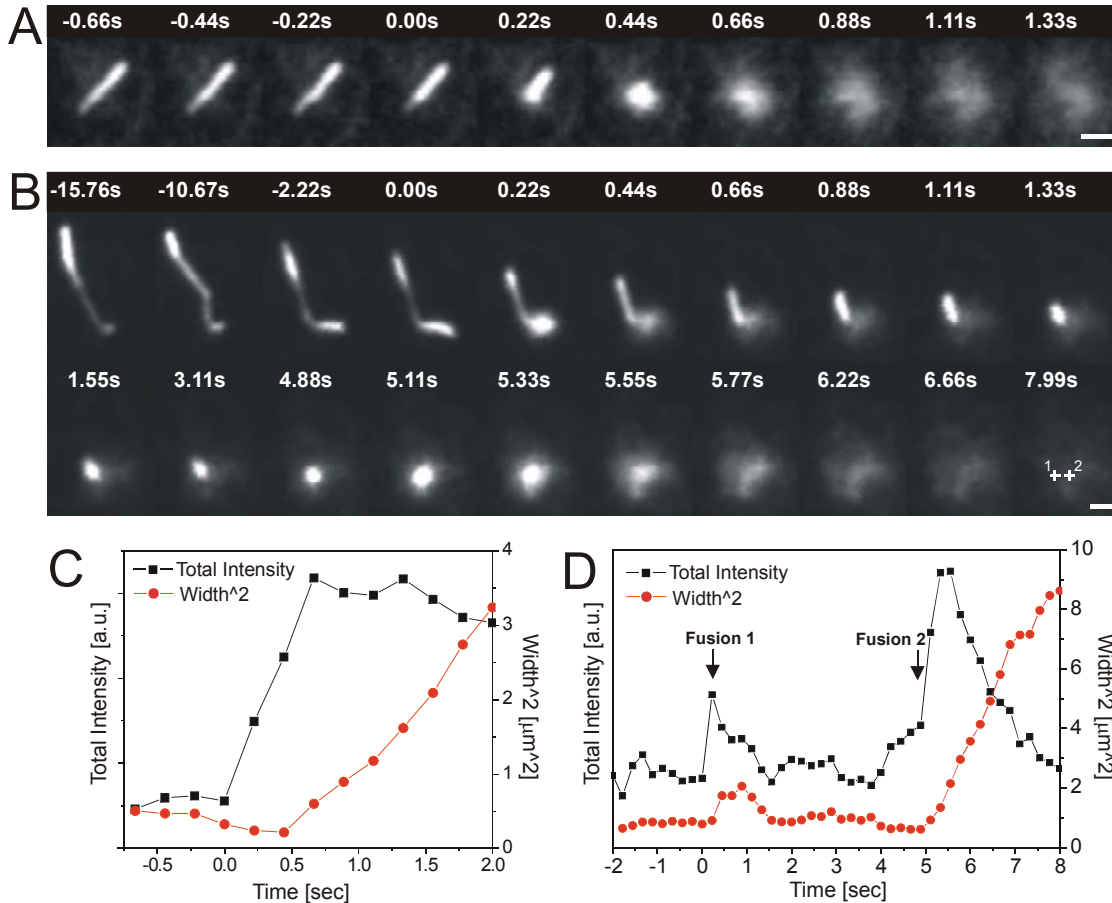


Figure 4.6. Collapse and fusion of tubular post-Golgi carriers (see videos). Sparsely plated MDCK cells were microinjected with cDNA encoding p75-GFP and imaged in TIR-FM after release of the Golgi block. Tubular carriers loaded with p75-GFP were seen to collapse and fuse both in a single step (A, C) and in two steps (B, D). For both carriers, the time is indicated relative to the fusion start. For the two-step fusion (B), the second fusion starts at 4.88sec. The location of the sequential fusions are marked by crosses 1 and 2 in the last frame (time=7.99sec), indicating that the carrier was displaced by $\sim 0.5\mu\text{m}$ between fusions 1 and 2. The total and the width² of the intensity of the fusing tubular carriers are plotted (C, D). Scale bars = $1\mu\text{m}$.

signal behind. This fusion in multiple steps we will call partial fusion. Partial fusion was seen for both vesicular and tubular carriers in all cell types examined. However, it is most clearly resolved as multiple fusions from a single elongated tubule. An example of one $6\mu\text{m}$ long tubule is shown from an MDCK cell (Fig. 4.6b). At $t = 0$ there is an initial fusion as indicated by a brief simultaneous rise in total and width² of the fluorescence intensity (Fig. 4.6d). This fusion is co-incident with an abrupt shortening of the rest of the tubule. During the shortening event the tubule moved toward the fusion site with a maximum speed of $\sim 5\mu\text{m}/\text{sec}$.

This value is at least 2-fold faster than reported maximum speeds for kinesin mediated vesicle movements on MTs (2.5 μ m/sec) (Trinczek et al., 1999). This collapse of the carrier along the MT is similar to what was shown in single-color (Fig. 4.6a) and dual-color imaging (Fig. 4.5c). However, in Fig. 4.6b the post-Golgi carrier does not collapse fully into the fusion center. The first (partial) fusion and shortening was followed by a 3-4 sec long stationary phase. Then the tubule fused a second time to a spot shifted by about 0.5 μ m relative to the first fusion site (see crosses in last frame of Fig. 4.6b). During the second fusion event all remaining cargo is diffusing in the plasma membrane, as shown by the linear increase in width² (time ~ 5-8 sec, Fig. 4.6d).

4.2.4. Nocodazole alters the sites of post-Golgi carrier fusion with the plasma membrane

The potential role(s) of MTs in the spatial distribution of post-Golgi cargo delivery to the plasma membrane was examined by mapping the sites of fusion in untreated and in nocodazole-treated stationary NRK cells. NRK cells were grown to confluence for 2 days, such that each cell was in contact with neighboring cells. Herein, we will refer to these cells as 'stationary' (Fig. 4.7e, left). The membrane protein LDLR-GFP was accumulated in the Golgi/TGN by incubating the cells at 20°C. Fusion of post-Golgi carriers was detected at the plasma membrane by 10min after shifting the cells to 32°C. Fusion was observed with an average frequency of ~8 fusions/min (181 fusions in 4 cells) until the Golgi was completely empty, which sometimes took more than 60 min. The sites of fusion in a stationary cell were widely distributed over the cell surface (Fig. 4.7a), showing areas of sparse and areas of more clustered fusion sites. In general, most of the carriers were transported away from the Golgi towards the periphery of the cell until they fused.

When NRK cells were treated with 10 μ M nocodazole during the last hour of the 20°C Golgi block, the MTs were largely, but not completely, depolymerized, resulting in a partially dispersed Golgi (data not shown). The post-Golgi carriers showed very little directed transport (see video 4.7b).

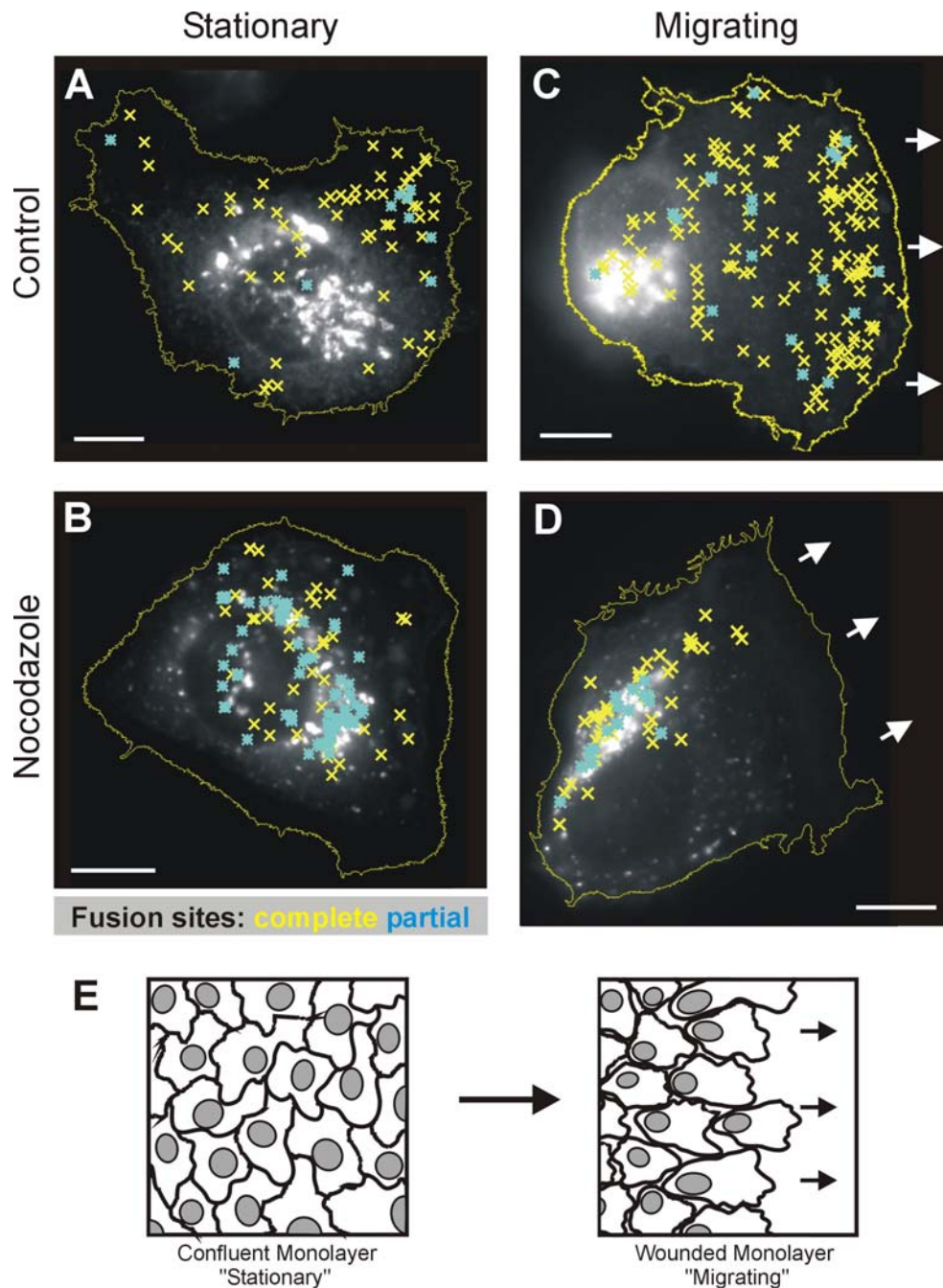


Figure 4.7. Map of fusion sites of post-Golgi carriers in NRK fibroblasts (see videos). NRK fibroblasts were microinjected with cDNA encoding LDLR-GFP and imaged in TIR-FM (~5 frames/sec) after release of the Golgi block. Epifluorescence images were taken just before release of the Golgi block (gray scale image) to indicate Golgi location. Cells are outlined in yellow. The fusion sites accumulated over time (~60min after release) are indicated by either yellow crosses or cyan stars, depending on if the fusions were complete or partial, respectively. For the migrating cells (C, D), the direction of the leading edge is indicated by white arrows. Stationary (A, B) and migrating cells (C, D) are either untreated (A, C) or treated with 10 μ M nocodazole (B, D) during the last hour of the 3h Golgi block. Scale bars = 10 μ m. (E) When a confluent monolayer of NRK fibroblasts (left, "Stationary") is wounded, the cells at the wound edge (right, "Migrating") change from a symmetric to an asymmetric shape and start migrating into the free space.

Fusion events were still observed, but at a reduced frequency (~4 fusions/min, 185 fusions) and the sites were almost exclusively clustered around the partially dispersed Golgi area (Fig. 4.7b). Very few fusions occurred in the periphery of the cell. When 10 μ M nocodazole was added 30min after microinjection and kept in the medium during the 3hr Golgi block, the MT array completely disassembled and the Golgi was fully dispersed into small fragments throughout the cytoplasm (data not shown). Under these conditions the frequency of fusion (~4 fusions/min, 68 fusions) was similar to that of the shorter nocodazole treatments. Again, we did not observe directional transport of any post-Golgi carriers by TIR-FM.

We quantified the distribution of fusion sites by measuring the distance of each site from the closest Golgi element (methods). This analysis assumes that post-Golgi carriers travel minimal distances between the exit site at the Golgi and the site of fusion. Since post-Golgi carriers are transported along curvilinear MT-tracks this does not display the truly traveled distance. However, this analysis can be used to compare the statistical distributions of the values from cells under different conditions. For untreated stationary cells, the distance values show a fairly even distribution falling off gradually at about 40% of the maximum distance between the Golgi-center and the furthest edge of the cell (Fig. 4.8a). In contrast, in nocodazole-treated cells, the distribution is dramatically shifted to smaller values, with ~70% of all fusion sites clustered between 0 % and 5 % (note the break in the vertical axis).

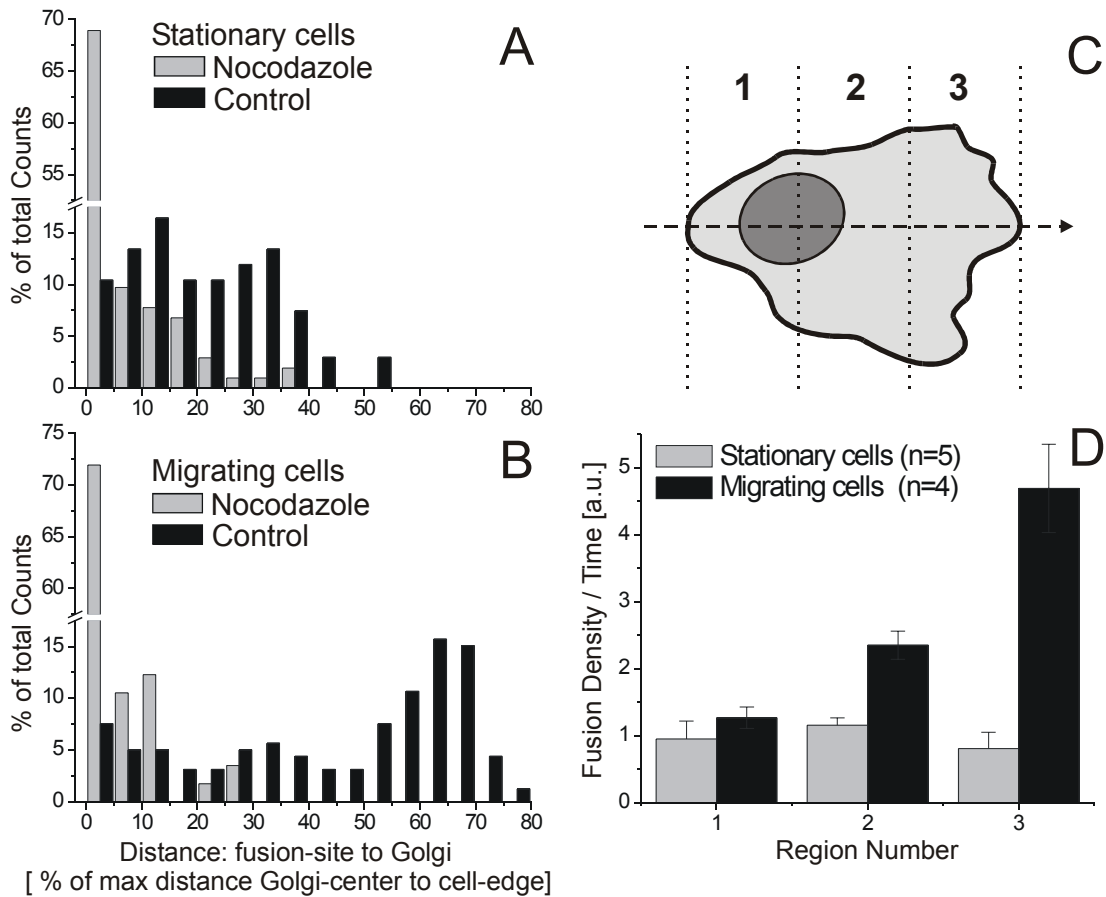


Figure 4.8. Comparison of fusion site distribution between stationary and migrating fibroblasts in untreated and nocodazole-treated cells.

(A, B) Histogram displaying the distances of the fusion sites of post-Golgi carriers from the nearest Golgi-signal in NRK fibroblasts. The distance from each fusion site (Fig. 4.7) to the closest Golgi-element (before the release of the Golgi block) were measured for stationary cells (A) and migrating cells (B). The data from untreated and nocodazole-treated cells are coded in black and gray, respectively. To normalize for cell size, the distance values are displayed as the percentage of the maximal distance between the Golgi-center and the furthest edge of the cell. Frequencies are expressed as % of total (Note the axis break).

(C, D) Distribution of the fusion density in stationary and migrating NRK fibroblasts. For each cell the long axis was defined as the furthest distance from edge to edge through the center. The total region of the cell was then divided into three orthogonal parts with equal width along the long axis (C). To compare migrating and stationary cells, we chose region 1 to be at the end of each cell, which was closest to the nucleus. For each cell, the number of fusion sites were counted in each region (1-3) and the area of each region was measured. For the purpose of comparing different cells, both fusion number and area were normalized as percent of total. The fusion density was determined by dividing the normalized number of fusions per region by the normalized area of each region. To account for the higher fusion frequency in migrating cells (~22 fusions/min) compared to stationary cells (~8 fusions/min), the values for the migrating cell were multiplied by factor 2.75. Mean fusion density values (+/- SEM) for each cell (stationary: 5 cells, 176 fusions and migrating: 4 cells, 375 fusions) were plotted (D).

4.2.5. Nocodazole alters the dynamics of post-Golgi carrier fusions with the plasma membrane

In stationary cells that were not treated with nocodazole, partial fusions were detected ~14% of the time (181 fusions in 4 cells) for both spherical and tubular carriers (representative example Fig. 4.7a). The distribution of “complete” (yellow crosses) and “partial” (cyan stars) fusions was mapped across the plasma membrane. The distribution of partial fusions was indistinguishable from that of complete fusions (Fig. 4.7a). For the short-term (1hr) incubation in nocodazole ~55% of all fusions (n=185) were partial and for the longer-term (3.5hr) incubation ~49% of all fusions (n=68) were partial. This is more than a 3-fold increase compared to the untreated cells. Rather than follow the distribution of complete fusions, the partial fusions were more heavily clustered in areas near the Golgi/TGN (Fig. 4.7b). The partial fusions in nocodazole-treated cells qualitatively differed from other fusions. In nocodazole-treated cells, we observed very large and static fluorescent spots close to the cell center. These compartments, which are potentially parts of the dispersed Golgi, were visible in TIR-FM and showed frequent partial fusion with the plasma membrane (Fig. 4.9). Interestingly, we observed many cases with multiple rounds of fusion at the same locations, without a complete emptying of the compartment. Nocodazole treatment also quantitatively changed the amount of cargo delivered during each fusion. In untreated cells the average amount of fluorescent membrane cargo delivered was ~2500 +/- 1700 fluorescent units (n=33), whereas in nocodazole-treated cells the distribution broadened and the average value increased to ~3900 +/- 2300 fluorescent units (n=30) (unpaired Student’s T-test: $p < 0.01$). Interestingly, we observed that the emptying of the dispersed Golgi stacks was incomplete in cells with completely disrupted MTs, leaving a significant amount of fluorescent cargo behind after more than 80min at 32°C. In contrast, the Golgi of untreated cells was emptied completely by this time (data not shown).

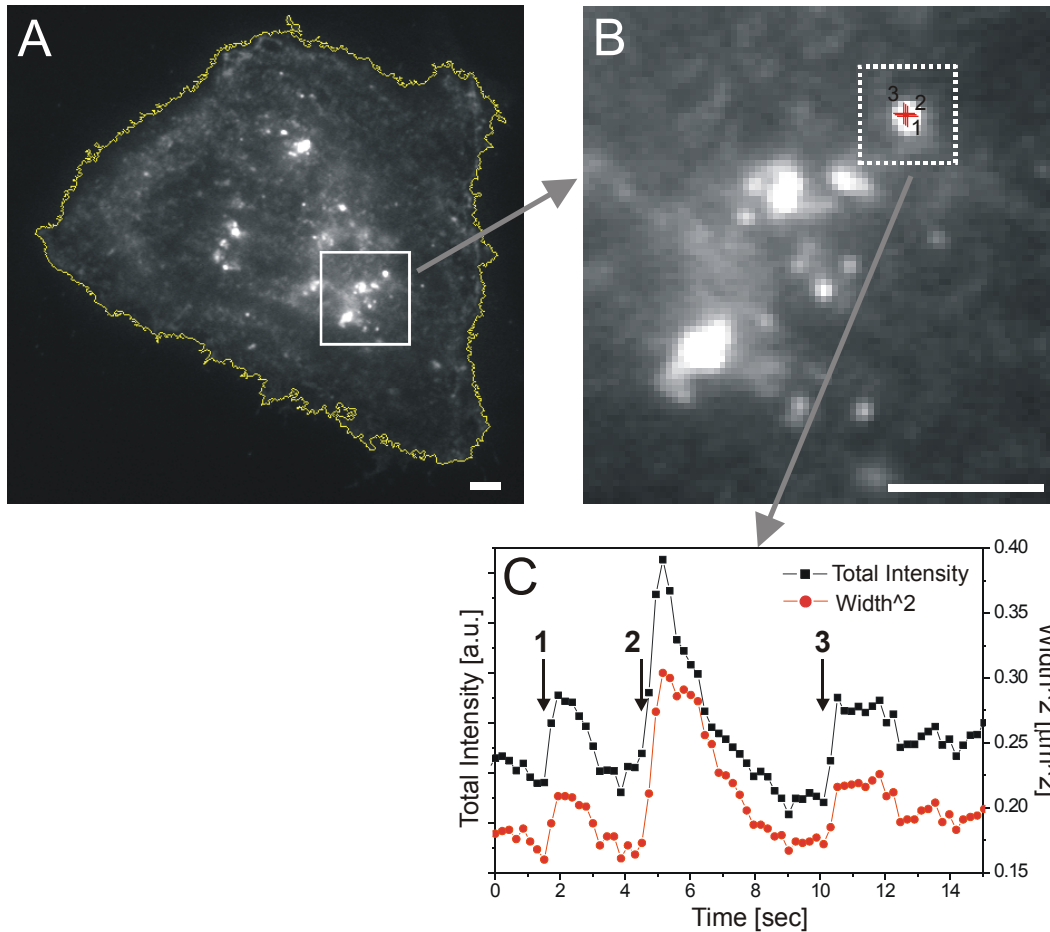


Figure 4.9. Partial fusion under nocodazole treatment (see video). NRK fibroblasts were microinjected with cDNA encoding LDLR-GFP and treated with $10\mu\text{M}$ nocodazole during the last hour of the Golgi block. The cell was then imaged in TIR-FM (~ 5 frames/sec) after release of the Golgi block. (A) The cell is outlined in yellow. The bright spots are most likely dispersed Golgi mini-stacks close to the cell surface. (B) Enlarged area from (A). The location of the fusions (1, 2, 3) are indicated by red crosses. (C) The total and the width² of the fluorescence intensity of these fusions are plotted. Each fusion start is indicated (arrows). Scale bars = $3\mu\text{m}$.

4.2.6. Migrating fibroblasts show polarized delivery of post-Golgi membrane carriers to the leading edge

It has been previously proposed that one of the mechanisms contributing to migration in cells is enhanced addition of membrane by exocytosis to the leading edge of a cell (Bergmann et al., 1983). Normal rat kidney (NRK) fibroblasts are a widely studied model for studying cell migration (Nagasaki et al., 1992). In a confluent monolayer, they exhibit symmetric shapes with a centered nucleus (Fig. 4.7e). Since their migration is contact inhibited, they are stationary in this

state. When part of the monolayer is removed (methods) they start extending large lamellopodia into the free space, leading to an asymmetric cell shape with the nuclei positioned at the trailing end of the cells. Ultimately they close the wound by migrating into the free space.

To test whether the delivery of post-Golgi cargo (LDLR-GFP) in migrating fibroblasts differs from that in stationary cells, we measured the frequency and the distribution of fusion events in cells at the edge of an experimental wound of an NRK monolayer. Only cells that underwent the morphological polarization typical for migrating fibroblasts were chosen for imaging. The criteria used were large lamellipodium towards the locus of the wound (referred to as the front of the cell) and the nucleus in the back. Similar to previous observations, ~ two thirds of these cells had their Golgi oriented towards the front of the cell (Palazzo et al., 2001). Thus, Golgi re-orientation was not used as a criterion for migration.

The post-Golgi traffic of migrating cells differed from that of stationary cells in various ways. Migrating cells exhibited a higher fusion frequency (~22 fusions/min, 353 fusions in 4 cells) compared to stationary cells (~8 fusions/min, 181 fusions in 4 cells). Most strikingly, many fusion sites were clustered at the leading edge of migrating cells (representative example Fig. 4.7c). This polarized distribution was quantified in two ways. First, the fusion density per time within three equally spaced areas along the axis of migration (methods) of the cell were determined (Fig. 4.8c). Clearly, compared to the stationary cells (n=5), the migrating cells (n=4) show strongly biased exocytosis within the region of the cell which includes the leading edge (Fig. 4.8d). Second, the distribution of the distances between the fusion sites and the closest Golgi elements were significantly shifted to higher values (peak at ~65%, average at ~44%) compared to stationary cells (peak at ~15%, average at ~21%) (Fig. 4.8b compared to 4.8a). Approximately half of all fusion sites were mapped at a position greater than 50% of the distance between the Golgi and the cell periphery. Mapping the complete and partial fusions separately showed that in the migrating cell, similar to the stationary cell, only a few evenly distributed partial fusions (~13%, 353 fusions in 4 cells) were observed (Fig. 4.7c). The number of fusions occurring at

the leading edge is likely to be underestimated because many carriers were transported to the leading edge and disappeared abruptly without obvious fusion, just before they reached the edge. The lamellipodia may not be close to the coverslip and it is possible that these 'lost' carriers fused with regions of the plasma membrane outside the evanescent field. This is consistent with the observation of a sharply bordered exclusion of fusion sites $\sim 1\text{-}2\mu\text{m}$ before the end of the leading lamella. Alternatively, the carriers might not be transported into the dense actin meshwork at the leading edge.

When migrating NRK fibroblasts were treated with nocodazole for one hour prior to release of the Golgi block, the fusion sites were observed clustered around the partially dispersed Golgi (Fig. 4.7d), similar to the distribution in nocodazole-treated stationary cells (Fig. 4.7b). The distribution of the distances between the fusion sites and the closest Golgi element shifted dramatically to lower values (Fig. 4.8b). Again, $\sim 70\%$ of all fusion sites are clustered between 0 % and 5 % of the maximal distance from Golgi-center to cell-edge (note the break in the vertical axis). Also, as in stationary cells, the ratio of partial versus complete fusions increased compared to the untreated cells and the partial fusions were exclusively clustered around the Golgi elements.

4.2.7. Inhibition of myosin ATPases and depolymerization of the actin cytoskeleton slightly effects the docking time of post-Golgi carriers

Two pharmacological treatments were used to test whether the actin cytoskeleton plays a role in constitutive exocytosis. First, we used the drug butanedione-monoxime (BDM), which has been shown to inhibit the myosin-II and -V light chain kinases and lead to inhibition of postmitotic cell spreading in fibroblasts (Cramer and Mitchison, 1995). Second, we depolymerized the actin cytoskeleton with the drug cytochalasin-D.

Treatment with either 10mM BDM or 1 μ M cytochalasin-D had no detectable qualitative effect on the transport and fusion of post-Golgi intermediates carrying LDLR-GFP in NRK cells. In addition, the distribution of fusion sites was unaffected by BDM treatment (Fig. 4.10). The actin cortex has been suggested to play several roles in regulated exocytosis, including the capture and transport of secretory granules and synaptic vesicles close to the plasma membrane. The time between the cessation of directed transport and the start of fusion should be

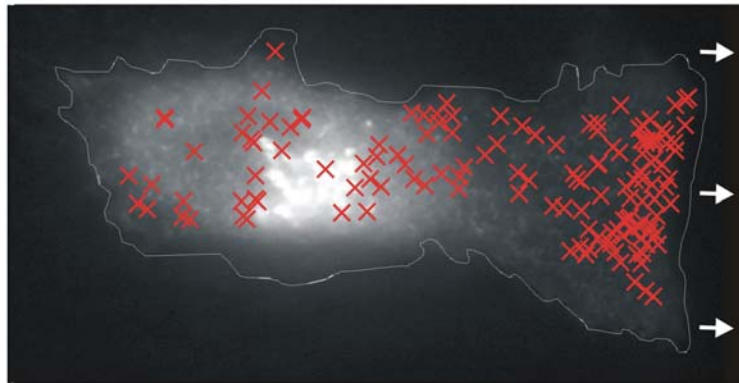


Figure 4.10. Map of fusion sites of post-Golgi carriers in BDM-treated NRK fibroblasts. NRK fibroblasts at the edge of an experimental wound were microinjected with cDNA encoding LDLR-GFP and imaged in TIR-FM in the presence of 10mM BDM (~5 frames/sec) after release of the Golgi block. An epifluorescence image was taken just before release of the Golgi block (gray scale image) to indicate Golgi location. The cell is outlined in white. The sites of fusion accumulated over time are indicated by red crosses. The arrows indicate the direction of the wound.

a characteristic parameter for this phase. For simplicity we call this the ‘docking’ time, even though this term is sometimes used to describe specific molecular interactions, which are completely unknown in the case of constitutive exocytosis in vivo. To probe for potential changes of the docking time under drug treatment, we measured the time during which the carriers remained stationary at one spot within a few pixels (~200nm radius) before they fuse. In control cells the docking time of post-Golgi carriers was found to have a broad distribution with a mean of 15.1 +/- 12.4 sec (n = 57) (Fig. 4.11). The docking time was slightly decreased when 10mM BDM was present in the recording medium (10.6 +/- 6.7 sec, n=61, unpaired Student’s T-test: p<0.05). Treatment with 1 μ M cytochalasin-D, when added at least 10min prior to start of acquisition, also slightly decreased the

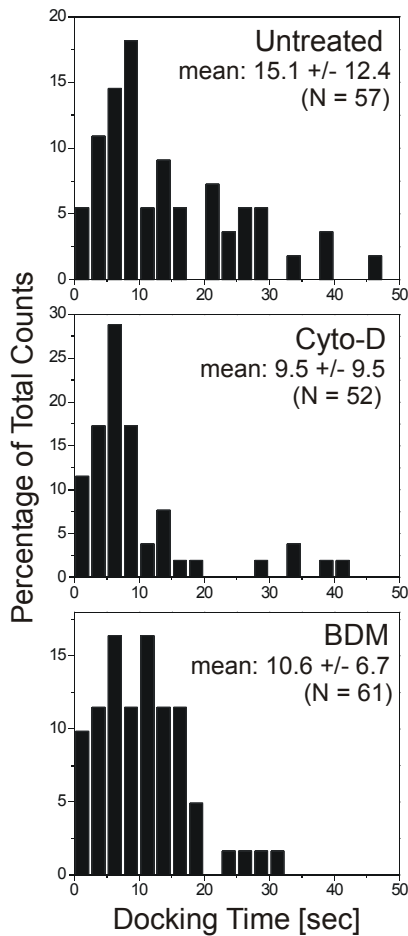


Figure 4.11. Histogram of docking times measured for post-Golgi carriers in untreated, Cytochalasin-D- and BDM-treated NRK fibroblasts. NRK fibroblasts were microinjected with cDNA encoding LDLR-GFP and imaged in TIR-FM. The docking times (see text for definition) of post-Golgi carriers (N>50) were measured for untreated, cytochalasin-D-treated and BDM-treated cells. The frequencies were normalized as percent of total.

docking time compared to untreated cells (9.5 +/- 9.5 sec, n=52, unpaired Student's T-test: p<0.01). Fusion could be monitored for up to 60 minutes in the presence of cytochalasin-D application without observing major retractions of the cell body under TIR-FM.

Depolymerization of the actin cortex with cytochalasin-D can result in changes of the cell morphology and adhesion pattern, which poses potential problems for TIR-FM. In these experiments, treatment with 1 μ M cytochalasin-D for 10min was sufficient to depolymerize many of the stress fibers and filamentous actin as observed by immunofluorescence (Fig. 4.12). However, since the cells were still attached to the coverslip, we assume that at least some of the actin filaments and structures were still intact.

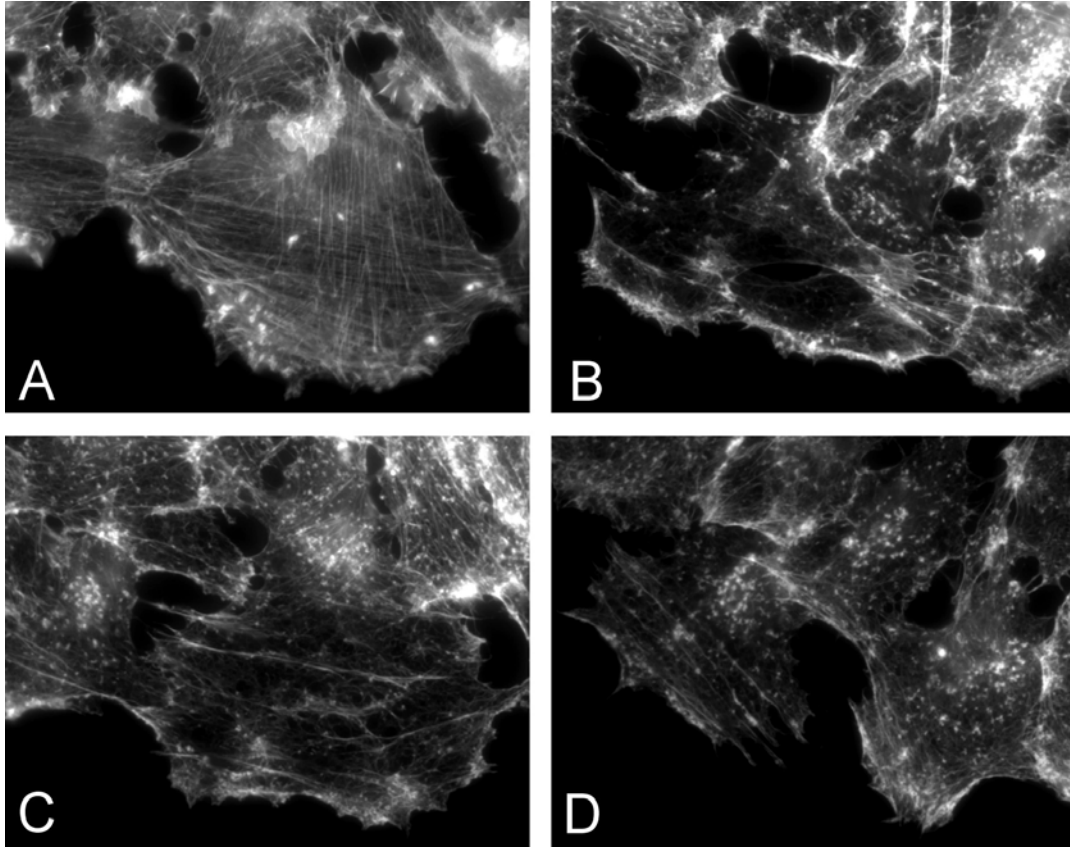


Figure 4.12. Depolymerization of actin with cytochalasin-D. NRK fibroblasts at the edge of an experimental wound were treated with 1 μ M cytochalasin-D for B) 5min, C) 10min and D) 40min. Most of the fine filamentous actin structures seen in the untreated cell (A) are depolymerized increasingly in (B) to (D). The treatment did not cause the cells to round up.

5. Targeted Exocytosis of Apical Proteins and Distribution of Syntaxin-3 is Microtubule-Dependent in polarized MDCK Cells

5.1. Introduction

Epithelial cells are tightly bound together in sheets that form barriers to the movement of water, solutes, and cells from one compartment of the body to the other. They perform polarized transport and secretion essential for the growth and maintenance of the organism. To perform these vectorial functions, epithelial cells segregate their plasma membrane proteins into apical and basolateral domains, separated by tight junctions.

Most of the current understanding of epithelial cells is based on model systems grown in tissue culture. Here, we used the widely studied epithelial cell line, Madin-Darby Canine Kidney (MDCK), which shows all phenotypic characteristics of an epithelial cell (Rodriguez-Boulan and Nelson, 1989). Most importantly, MDCK cells form tight monolayers when grown to confluency and establish an apical and basolateral plasma membrane domain, separated by the tight junctions (Fig. 5.1). This transition from the non-polarized (sub-confluent, no tight junctions) to the polarized (confluent) phenotype was the subject of this study. The main goal was to elucidate the mechanism of targeted delivery of secretory membrane proteins to both apical and basolateral membrane.

Apical and basolateral membrane proteins are synthesized in the endoplasmic reticulum, transferred to the Golgi apparatus and segregated into different post-Golgi transport intermediates (carriers) for export to the cell surface (Rodriguez-Boulan and Nelson, 1989; Simons and Wandinger-Ness, 1990; Keller et al., 2001). Segregation is thought to occur in the TGN and is mediated by sorting signals embedded within the protein structure. Apical sorting signals include N- and O-linked glycans in the ectodomain, glycoposphatidyl inositol and transmembrane anchors, and amino-acid stretches in the cytoplasmic domain (Chuang and Sung, 1998; Rodriguez-Boulan and Gonzalez, 1999). In

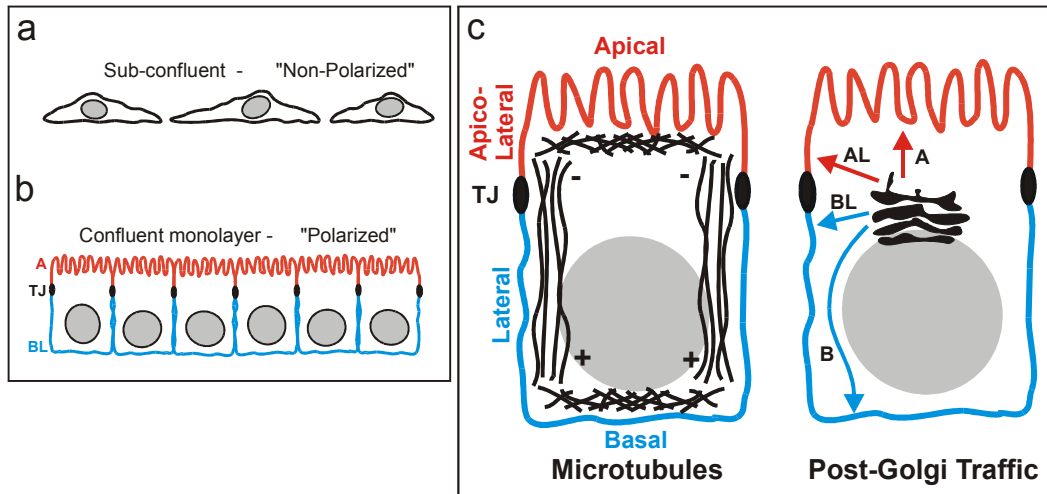


Figure 5.1. Polarized epithelial cells: membrane domains, MTs and post-Golgi traffic.

In the sub-confluent state (a), MDCK cells are “non-polarized” and resemble flat fibroblasts. In a confluent monolayer (b), MDCK cells are “polarized”. They have distinct apical (A, red) and basolateral (BL, blue) plasma membrane domains, separated by tight junctions (TJ, black).

(c) In the polarized state, the MTs are organized into (i) longitudinal bundles oriented with minus ends toward the apical membrane in parallel with the lateral membrane and (ii) arrays of mixed polarity underlying the apical pole and overlying the basal membrane. Post-Golgi traffic could happen in various ways: Carriers delivering apical cargo could fuse with the apico-lateral (AL) or the apical membrane (A). Basolateral carriers could fuse with either the lateral (L) or the basal (B) membrane.

contrast, basolateral sorting signals typically comprise amino acid stretches in the cytoplasmic domain that include tyrosine, dileucine and monoleucine motifs, as well as clusters of acidic amino acids (Le Gall et al., 1995; Ikonen and Simons, 1998). Apical or basolateral membrane proteins exit the Golgi in vesicular or tubular carriers (Toomre et al., 1999; Kreitzer et al., 2000; Keller et al., 2001). The formation of post-Golgi carriers depends on the direct or indirect interaction of sorting signals with cytoplasmic adaptors and coat proteins (Kirchhausen et al., 1997; Ohno et al., 1998; Bonifacino and Dell'Angelica, 1999). Adaptors can mediate binding of cargo to specific microtubule (MT) (Nakagawa et al., 2000; Setou et al., 2000; Noda et al., 2001) motors, which might modulate the budding as well as the morphology of Golgi-derived transport intermediates (Kreitzer et al., 2000).

Research on this subject in the past two decades suggests that MTs play an important role in the establishment of epithelial polarity. During epithelial polarization, MTs reorganize from centrosomally nucleated, radial arrays into (i)

longitudinal bundles (minus-ends toward the apical surface) oriented in parallel with the lateral membrane and (ii) arrays of mixed polarity underlying the apical pole and overlying the basal membrane (Fig. 5.1c) (Bacallao et al., 1989; Gilbert et al., 1991). This MT reorganization is accompanied by the relocation of the Golgi complex to apico-nuclear regions of the cytoplasm (Bacallao et al., 1989). Time-lapse studies on fibroblasts and sub-confluent Ptk₂ cells have shown that vesicular and tubular post-Golgi carriers of both apical and basolateral cargo move through the cytoplasm along MTs for delivery to the plasma membrane (Chapter 4 and (Toomre et al., 1999)). Injection of anti-kinesin antibodies completely inhibits post-Golgi transport indicating that MTs are essential for post-Golgi trafficking under physiological conditions (Kreitzer et al., 2000). Experiments in polarized MDCK cells assaying the bulk delivery of biosynthetic membrane proteins suggested that MTs play an important role in the targeting of apical, but not basolateral membrane proteins. For instance, MT disruption reduces delivery of apical, but not basolateral proteins, to the correct target membrane, and leads to mistargeting of apical, but not basolateral proteins (Rindler et al., 1987; Achler et al., 1989; Eilers et al., 1989; Matter et al., 1990; Breitfeld et al., 1990; Lafont et al., 1994; Saunders and Limbird, 1997; Grindstaff et al., 1998a). However, luminal proteins normally secreted to the basolateral medium appear in the apical medium upon MT disruption (Boll et al., 1991; de Almeida and Stow, 1991).

A key event in epithelial polarization is the establishment of polarized transport routes to apical and basolateral regions of the plasma membrane. The establishment of the polarized phenotype, including polarized exocytosis, correlates in time with the reorganization of the MT network (Grindstaff et al., 1998a). However, the mechanism by which apical and basolateral carriers reach the target membrane is still unclear. In principle, there are two possible transport routes for each type of cargo (Fig. 5.1c, apical: A or AL, basolateral: B or BL). It is currently thought that a determinant of polarized exocytosis in epithelial cells is the asymmetric distribution of docking and fusion machinery for post-Golgi carriers. Basolateral exocytosis appears to depend on an evolutionarily

conserved “tethering” complex known as the exocyst (Hsu et al., 1996; Grindstaff et al., 1998b; Vega and Hsu, 2001). In polarized MDCK cells the exocyst immunolocalizes to the apico-lateral membrane beneath the tight junction. Antibodies against two exocyst components sec6 and sec8 block basolateral transport and overexpression of a third component, sec10, leads to enhanced basolateral transport (Grindstaff et al., 1998b; Lipschutz et al., 2000). In polarized MDCK cells, the t-SNAREs syntaxin 3 and 4 localize exclusively to the apical and basolateral plasma membranes, respectively (Low et al., 1996). In semi-intact MDCK cell transport assays, cleavage of the t-SNARE component, SNAP23, with botulinum E toxin or the addition of anti-SNAP antibodies reduced delivery of apical and basolateral markers while anti-syntaxin 3 antibodies selectively inhibited apical transport (Low et al., 1998; Lafont et al., 1999). In intact cells, overexpression of syntaxin 3 results in decreased apical transport and a 2-fold accumulation of vesicles under the apical plasma membrane (Low et al., 1998). These data suggest a critical role for SNARE-mediated fusion events in polarized exocytosis. In other cell systems, i.e. yeast and neurons, t-SNAREs do not localize exclusively to sites of active exocytosis, suggesting that SNAREs may not be sufficient for secretory vesicle targeting in these systems (Hunt et al., 1994; Garcia et al., 1995; Hsu et al., 1996).

In the experiments reported here we monitored changes in targeted exocytosis, of both apical and basolateral membrane proteins in MDCK cells, as a function of polarization. In addition, we studied the role of MTs in this process, as well as in establishing the three-dimensional distribution of tethering or fusion complexes in polarized cells. We used time-lapse TIR-, epi and confocal fluorescence microscopy to analyze the intracellular distribution of post-Golgi carriers and their sites of fusion at the cell surface in non-polarized and polarized MDCK cells. Our results demonstrate that carriers containing both apical and basolateral proteins fuse to the basal surface in non-polarized cells. In polarized MDCK cells, apical and basolateral carriers have characteristic localizations in the apical cytoplasm, and fuse with restricted areas of the plasma membrane. The results implicate a role of MTs in the establishment of the apical exocytic

route. To our knowledge, this is the first time-lapse analysis of post-Golgi carrier trafficking and site-specific fusion in polarized epithelial cells.

5.2. Results

5.2.1. Apical or basolateral post-Golgi carriers fuse with the basal membrane in non-polarized MDCK cells

We used total internal reflection fluorescence microscopy (TIR-FM) to study where at the plasma membrane fusion of apical and basolateral post-Golgi carriers occurs, before and after MDCK cell polarization. We expressed GFP-tagged apical (p75 = neurotrophin receptor) and basolateral (NCAM = neuronal cell adhesion molecule and LDLRa18 = internalization-defective LDL-receptor) membrane proteins, by injecting cDNA into the nucleus of non-polarized or polarized MDCK cells (same method as illustrated in Fig. 4.4). During a 20°C incubation, newly synthesized membrane proteins accumulated in a perinuclear compartment (Fig. 5.2, epi) defined as Golgi/TGN by colocalization with newly synthesized galactosyl transferase (GalT), a Golgi-resident enzyme, fused to cyan fluorescent protein (CFP) (not shown). Following release of the temperature block, all three markers acquired a homogeneous distribution in non-polarized cells, and distinctive apical or basolateral distributions in polarized cells.

As discussed earlier, carriers containing GFP-tagged fusion proteins are detected in TIR-FM only when they are within ~125nm (methods, 60x NA1.45 objective) of the plasma membrane domain making contact with the coverslip (hereafter referred to as the “basal” plasma membrane). In sparsely-seeded, non-polarized MDCK cells, we detected numerous vesicular and tubular carriers moving near the basal membrane after release of the 20°C Golgi/TGN block. Using the previously described quantitative criteria for fusion of post-Golgi carriers (Chapter 3) we identified fusion of vesicular and tubular carriers for all fluorescent marker proteins. In representative time-lapse recordings (500 frames, ~5 frames/sec, 3 independent experiments) carriers containing p75-GFP (n=57 in Fig. 5.2a), LDLR-GFP (n=42 in Fig. 5.2b) or NCAM-GFP (n=27) fused with the

basal membrane (white circles). Fig. 5.2c shows fusion of a tubular (p75-GFP) and a vesicular (LDLR-GFP) carrier. Fusion of post-Golgi carriers began within 5 min after release of the Golgi block and continued for 60-70 min (NCAM-GFP) or up to 2h (LDLR-GFP or p75-GFP). In all cases, the cessation of plasma

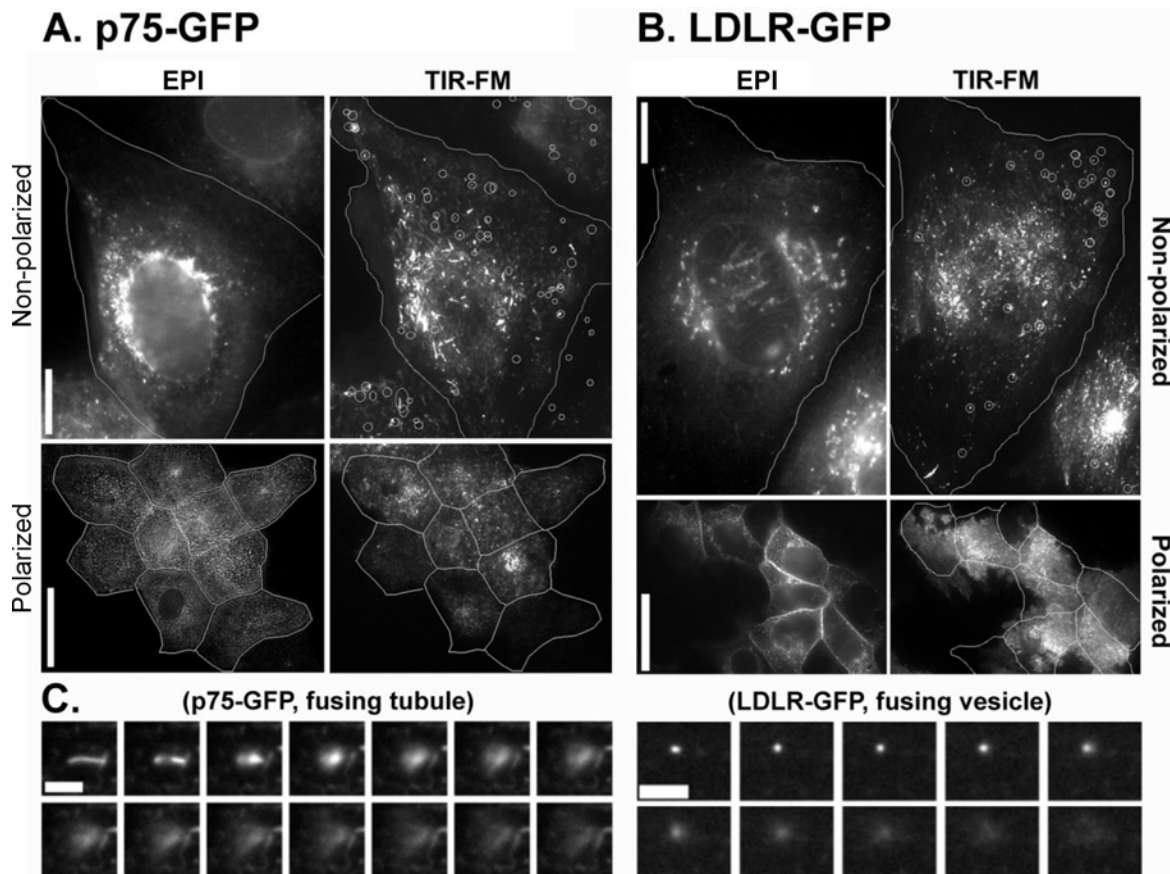


Figure 5.2. Fusion of post-Golgi carriers with the basal membrane in MDCK cells (see videos). Non-polarized and polarized MDCK cells were microinjected with cDNA encoding (A) p75-GFP and (B) LDLR-GFP and the basal membrane was monitored in TIR-FM (~5 frames/sec) after release of the 20°C Golgi block.

Non-polarized cells: EPI images show the total intracellular distribution of GFP-tagged membrane proteins just after release of the Golgi block. TIR-FM images (B, C) show time-lapse overlays (every 20 frames) from recordings made in cells expressing p75-GFP (21min after release of the Golgi block) or LDLR-GFP (19 min after release of the Golgi block). Fusion events are mapped (white circles). Selected sequential frames show examples of individual tubular (p75) or vesicular (LDLR) carriers fusing with the membrane (C).

Polarized cells: No fusions were detected in TIR-FM for carriers containing p75-GFP or LDLR-GFP at the basal membrane at any time after release of the Golgi block (A, B). The corresponding EPI images (~60min after release of the Golgi block) show that p75-GFP and LDLR-GFP emptied from the Golgi and localized to the apical and basolateral plasma membranes, respectively. Scale bars represent 2µm (A) and 15µm (B, C).

membrane fusion correlated directly with the emptying of GFP-markers from the Golgi as detected using epi-illumination. The map of the fusion events (Fig.5.2, TIR-FM, white circles) shows areas of sparse and areas of more clustered fusion events within individual cells, similar to data described previously (Chapter 4, (Keller et al., 2001)). This bias likely reflects a high concentration of MTs reaching the cell surface in the clustered areas. This idea is consistent with our results on fibroblasts showing that post-Golgi carriers move along MTs to their fusion site with the plasma membrane (Chapter 4). As seen in the fibroblasts, most of the carriers were transported away from the central Golgi towards the periphery of the cell until they fused.

5.2.2. Fusion of post-Golgi carriers with the basal membrane is abrogated by cell polarization

In contrast to the non-polarized MDCK cells, we did not detect any fusion of apical or basolateral carriers with the basal membrane in polarized cells (Fig. 5.2a,b, TIR-FM, polarized). Despite the lack of detectable fusion events using TIR-FM, epi-illumination clearly showed that p75-GFP (Fig. 5.2a, epi, polarized) was delivered to the apical membrane while both LDLR-GFP (Fig. 5.2b, epi, polarized) and NCAM-GFP (not shown) were delivered to the lateral membrane. Although we detected no fusion of any carriers, TIR-FM revealed that some carriers moved in close proximity with the basal membrane, similar to the carrier movements observed in non-polarized cells (video 5.2). This suggests that the basal membrane is simply not fusion competent in polarized cells. These results show that fusion of post-Golgi carriers is restricted to regions of the plasma membrane other than the basal domain after epithelial cell polarization.

5.2.3. Targeted delivery of apical and basolateral cargo correlates with the distribution of syntaxin 3 and 4

We next studied whether changes in the distribution of the targeting and fusion machinery correlate with the abrogation of basal fusion upon polarization of MDCK cells. To this end, we analyzed the surface localization of the t-SNARES syntaxin 3 and 4, and the exocyst component sec6, in sub-confluent and fully

polarized MDCK cells. In sparsely seeded cells both syntaxin 3 and syntaxin 4 localized to all plasma membrane surfaces (Fig. 5.3). In polarized cells, however, neither syntaxin was present at the basal membrane. Instead, syntaxin 3 localized exclusively to the apical membrane while syntaxin 4 was highly enriched in the lateral membrane of polarized cells (Low et al., 1996). In non-polarized cells, epifluorescence imaging revealed that sec6 localized to both the cytoplasm and punctate foci distributed throughout the plasma membrane (not shown). Additionally, we found that sec6 foci were abundant at the basal membrane when imaged by TIR-FM (Fig. 5.3). In polarized cells, however, we found that sec6 localized exclusively in the lateral membrane. Thus, fusion, or lack thereof, of apical and basolateral carriers with the basal membrane may be attributed to the presence or absence of exocyst components and/or syntaxins 3 and 4 in the basal membrane of non-polarized and polarized cells, respectively.

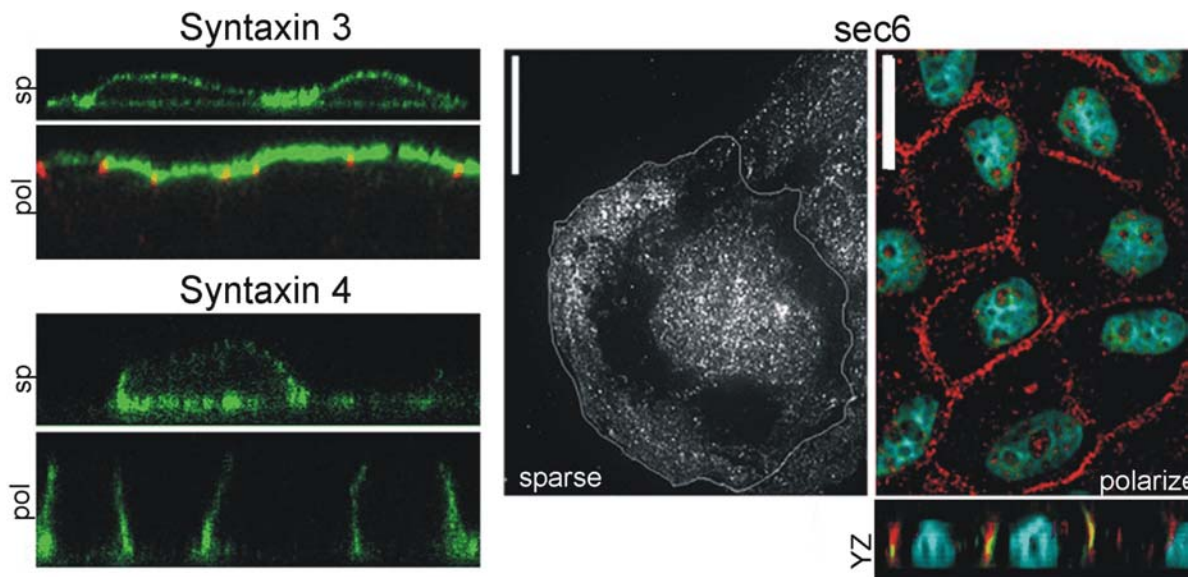


Figure 5.3. Localization of syntaxins 3 and 4 and sec6 in MDCK cells. Steady-state, surface distribution of syntaxins 3 and 4 (green) in sparse (sp) and polarized (pol) MDCK cells was determined by immunostaining for the extracellular myc epitope-tag fused to syntaxins 3 and 4. Images are z-sections of confocal series. Note that syntaxins 3 and 4 were detected throughout the cell surface of non-polarized cells but were enriched in the apical and lateral membranes, respectively, of polarized cells. The tight junction marker, ZO-1 (red) was co-immunostained as a reference for cell-cell boundaries in syntaxin 3 expressing cells. In non-polarized cells, sec6 immunolocalized to discrete puncta near the basal membrane by TIR-FM (gray scale image). In polarized cells, sec6 (in red) was present in the lateral membrane (xy-view, top panel) and colocalized throughout the lateral membrane with e-cadherin (green, yz-view, bottom panel). Dapi-stained nuclei are shown in blue. Scale bars = 20 μ m.

5.2.4. Post-Golgi carriers localize predominantly to the apical half of polarized MDCK cells and fuse with the lateral membrane

The complete loss of basal fusion raises the question as to where at the plasma membrane post-Golgi carriers are being delivered in polarized cells. To address this issue we made time-lapse recordings, using either epi or confocal fluorescence microscopy, of multiple focal planes in polarized cells expressing p75-GFP, NCAM-GFP or LDLRa18-GFP. In all our experiments, MDCK cells were grown on glass coverslips, and polarized cells reached an average height of 10-12 μ m. In time-lapse images from serial Z-axis sections we found that post-Golgi carriers containing NCAM-GFP (Fig. 5.4a) and LDLRa18-GFP (not shown) were concentrated in the cytoplasm in focal planes between 4-8 μ m above the basal plasma membrane. Carriers containing the apical marker, p75-GFP, were further restricted in the cytoplasm to between 1.5-3 μ m below the apical membrane (Fig. 5.4b). Here, we observed numerous carriers emerging from the Golgi and moving immediately beneath the apical membrane. Very few carriers were observed in the bottom and middle portions of polarized cells. These results demonstrate that apical and basolateral carriers are restricted to different regions of the apical cytoplasm in polarized MDCK cells.

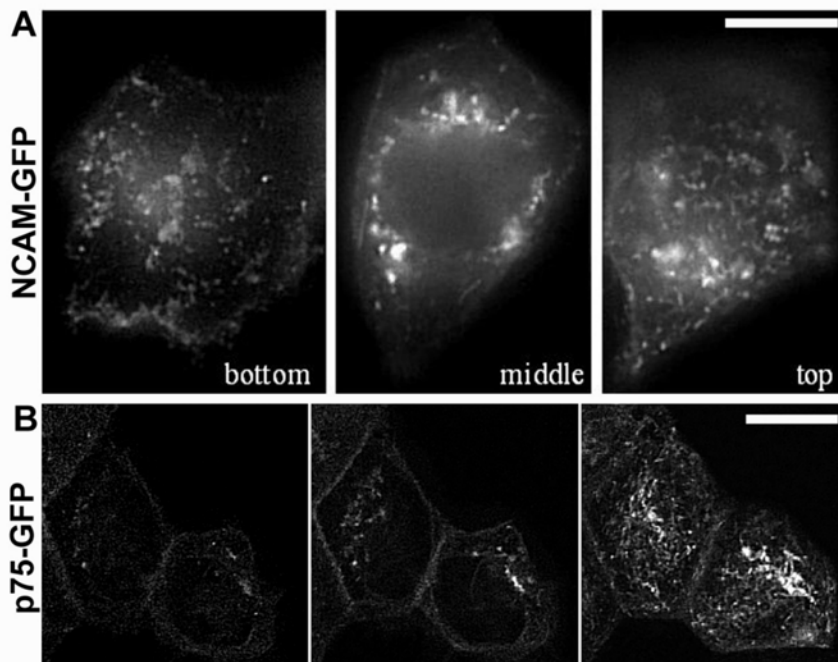


Figure 5.4. Post-Golgi carriers are restricted within the apical cytoplasm (see videos). The spatial distribution of post-Golgi carriers in polarized cells was determined using epi or confocal time-lapse imaging in sequential z-axis planes. Single time-points from recordings taken at the cell “bottom”, “middle” (z-position = 3-5 μ m from bottom) or “top” (7-10 μ m from bottom) are shown for (A) NCAM-GFP and (B) p75-GFP. Scale bars = 10 μ m.

We developed a colorimetric fusion assay to analyze whether fusion of post-Golgi carriers occurred within the lateral membrane of polarized cells. In this assay we defined fusion by a transient green-to-yellow color change of a GFP-containing carrier as it merged with the red fluorescently labeled (DiIC¹⁶) plasma membrane (methods). To determine the spatial distribution of fusing carriers we acquired confocal time-lapse sequences in sequential Z-axis planes throughout the cell depth. In cells expressing NCAM-GFP (Fig. 5.5) or LDLR-GFP (not shown), we were able to detect individual carriers translocating through the cytoplasm toward the DiIC¹⁶-labeled lateral membrane. While many carriers moved out of the confocal focal plane (~1.5 μ m) before being delivered to the plasma membrane, we were able to isolate and record individual carriers containing basolateral cargo as they approached, and subsequently merged with the lateral plasma membrane (Fig. 5.5). The NCAM-GFP labeled carrier (green)

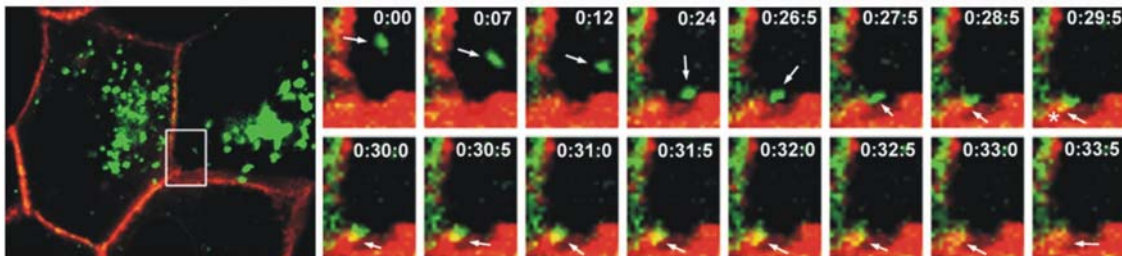


Figure 5.5. Fusion of a basolateral post-Golgi carrier with the lateral membrane in polarized MDCK cells (see video). Polarized MDCK expressing NCAM-GFP (green) were incubated with DiIC¹⁶ (red) to fluorescently label the plasma membrane. Transport and delivery of NCAM-GFP to the plasma membrane was monitored by time-lapse confocal microscopy (2 frames/sec). Selected frames (time-lapse panel) show a region of the lateral membrane (white box) where fusion of a carrier occurs. Fusion was defined as a transient color change from green to yellow. The moving carrier is marked by white arrows. Time stamps represent (min : sec : 100ms). The asterisk in frame (0:29:5) marks the point at which the carrier begins to turn yellow. Then the yellow color intensifies as NCAM-GFP is absorbed into the membrane. Finally (frame 0:33:0), the yellow color reconverts to red, marking the diffusion of NCAM-GFP throughout the lateral membrane.

approached, contacted (*, time 0:29:5) and merged into the DiIC¹⁶ labeled (red) plasma membrane. The transition to yellow suggests that the contents of the carrier mixed with the DiIC¹⁶ labeled membrane. Within 3.5 seconds, the yellow NCAM-GFP spread within the membrane and rapidly became red again. This color change was most likely due to the carrier delivering all its cargo and the

NCAM-GFP diffusing in the plasma membrane. These presumptive lateral fusion events were only observed within 4-8 μ m above the basal membrane, which corresponds to cytosolic regions containing the highest density of carriers.

Although post-Golgi carriers containing p75-GFP were abundant in apico-lateral regions of the cell, we could not detect any examples of these carriers fusing with the lateral membrane using our colorimetric criteria. The majority of the p75-GFP carriers was localized just below the apical membrane, such that they were in a separate focal plane than the DiIC¹⁶-labeled apical cell surface. Thus it was not possible to determine whether p75-GFP is delivered directly to the apical plasma membrane using the confocal microscope.

5.2.5. MTs are required for the targeted fusion of apical but not basolateral membrane proteins in polarized MDCK cells

We showed that in polarized MDCK cells neither apically nor basolaterally targeted post-Golgi carriers fuse to the basal surface. It is known that MT disruption perturbs the polarized distribution of many apical, but not basolateral membrane proteins. To investigate the role of MTs in restricted targeting in polarized cells, we tested whether carriers containing apical or basolateral membrane cargo fused with the basal membrane when the MTs were disrupted.

To depolymerize all MTs we incubated cells on ice in the presence of 20 μ M nocodazole for 60min prior to microinjection. Cells were kept in 10 μ M nocodazole for the duration of experiments to prevent re-assembly of MTs. Nocodazole treatment resulted in fragmentation of the Golgi apparatus into numerous Golgi mini-stacks dispersed throughout the cell but affected neither expression nor Golgi accumulation of reporter proteins (Fig. 5.6a). After incubation at 20°C, Golgi mini-stacks containing either apical or basolateral GFP-tagged membrane proteins were visible in close proximity to the basal membrane by TIR-FM (Fig. 5.6b). This is in stark contrast to polarized cells with an intact MT array where the Golgi localizes to a supra-nuclear position and cannot be detected by TIR-FM (compare with Fig. 5.2). Additionally, in nocodazole-treated cells that were co-injected with p75-CFP and LDLR-YFP, apical and basolateral markers

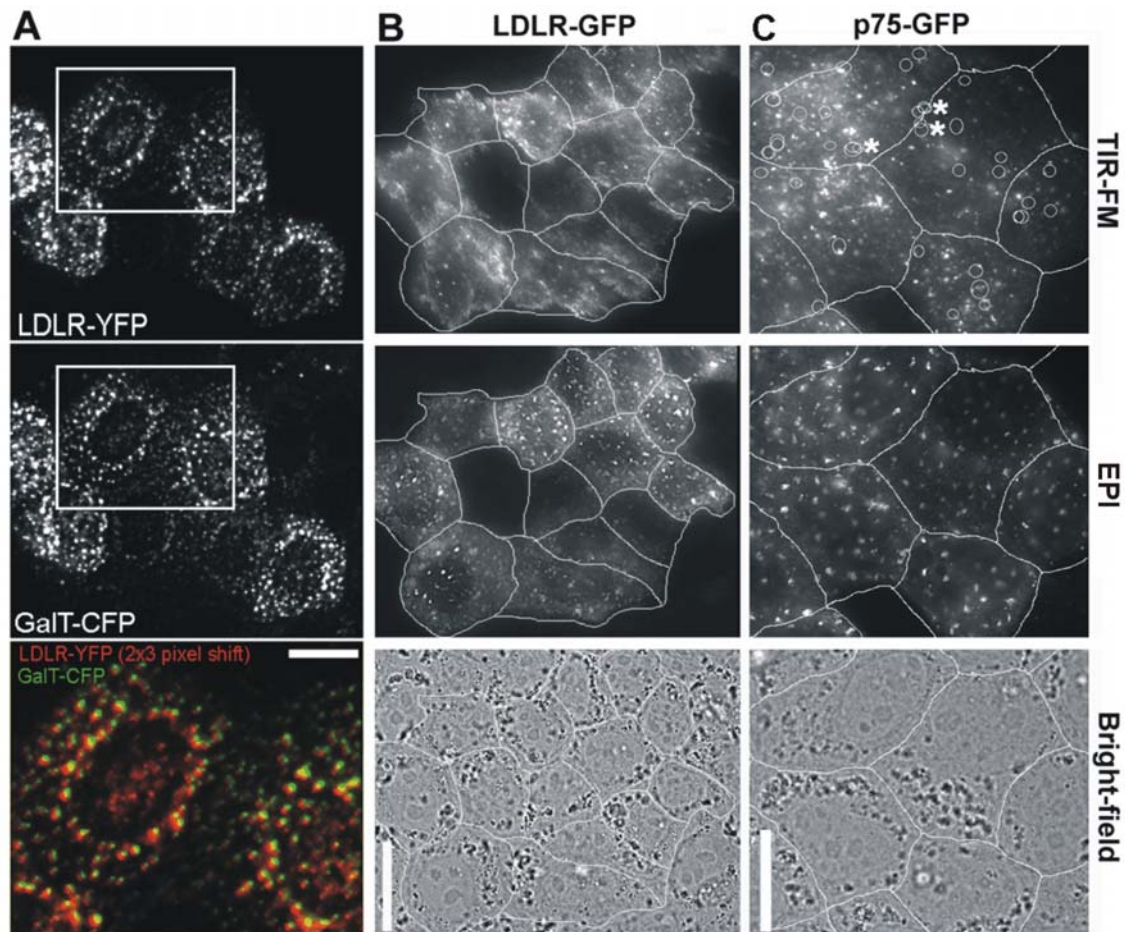


Figure 5.6. Delivery of apical and basolateral post-Golgi carriers in nocodazole-treated, polarized MDCK cells (see videos). (A) Nocodazole induced fragmentation and scattering of the Golgi/TGN labeled by GaIT-CFP. GaIT-CFP and LDLR-YFP colocalize after incubation at 20°C (color overlay); the LDLR-YFP image was shifted down and left (2x3 pixels) to best illustrate the degree of colocalization. Golgi fragmentation after nocodazole-treatment did not block accumulation of newly synthesized LDLR-YFP (A, epi), LDLR-GFP (B, epi) or p75-GFP (C, epi) in the Golgi elements during a 20°C block.

(B) The basal plasma membrane was monitored by TIR-FM. White circles mark the fusion sites. Note that only p75-GFP-containing carriers fused with the basal membrane. Asterisks (C, TIR-FM) mark the position of repeated partial fusion events. The epi images show maximum projections of serial z-axis images of p75 (2min after release of Golgi block) and LDLR (14min after release of the Golgi block). Cell boundaries were marked using the bright-field image as a reference (bright-field). Scale bars = 15µm.

colocalized in Golgi mini-stacks during the 20°C block. However, both markers emptied from the Golgi at different rates after release of block (data not shown), indicating that the protein sorting activity of the Golgi/TGN is maintained in the absence of MTs.

After release of the Golgi block, neither carriers containing LDLR-GFP (Fig. 5.6) nor NCAM-GFP (not shown) could be detected fusing with the basal plasma

membrane in the absence of MTs. In striking contrast, carriers containing p75-GFP fused with the basal membrane under these conditions (Fig. 5.6b).

Consistent with the results obtained from fibroblasts (Chapter 4), in the absence of MTs, the sizes of the carriers seen in TIR-FM were often much larger than in untreated cells (compare videos 5.6c to 5.2a). Again similar to the fibroblast results, we observed an increase in “partial” fusion events wherein carriers released some, but not all, of their cargo into the plasma membrane. Some partial fusions occurred at the same spot during the course of a single recording (asterisks in Fig. 5.6) suggesting that individual carriers can repeatedly deliver cargo to the plasma membrane. Additionally, structures containing GFP-tagged cargo did not move laterally along the cell surface in the absence of MTs. This suggests that in the absence of MTs, other cytoskeletal elements, e.g. actin filaments, are not sufficient for carrier movement at the cell-substratum interface.

5.2.6. Mistargeting of p75-GFP after MT-disruption corresponds with appearance of syntaxin 3 at the basal membrane

To investigate a possible correlation between mistargeting of p75-GFP and any proposed component of the fusion machinery in polarized cells, we tested whether the distribution of syntaxin 3, syntaxin 4 and sec6 were altered by MT-disruption. Nocodazole treatment resulted in dramatic redistribution of syntaxin 3 from the apical surface to both apical and basolateral membranes. However, neither syntaxin 4 nor sec6 were relocated upon MT-disruption (compare Fig. 5.3 and Fig. 5.7, polarized cells). These results suggest that redistribution of syntaxin 3 plays a role in effecting the mistargeting of apical cargo to basolateral membranes after MT-disruption.

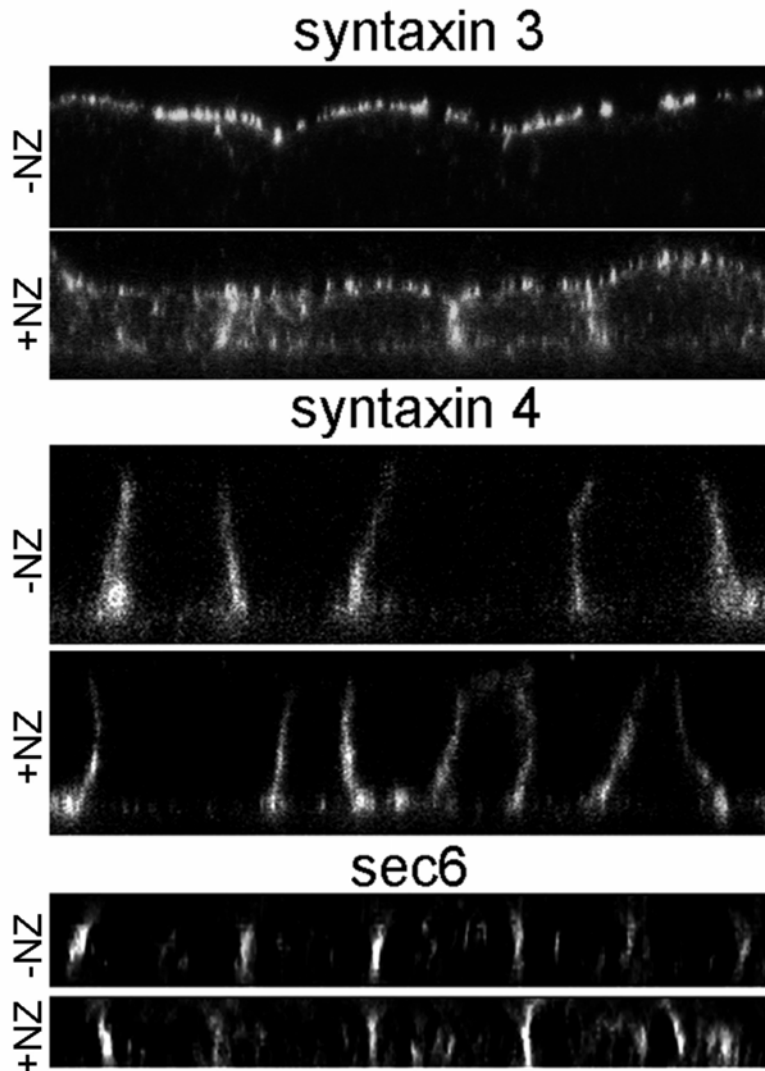


Figure 5.7. MT-disruption results in the non-polarized distribution of syntaxin 3, but not syntaxin 4 or sec6, in polarized MDCK cells. MTs were depolymerized as described (methods). Cells stably transfected for myc-tagged syntaxins 3 or 4 were surface-labeled with anti-myc antibody. The images show xz-sections taken by confocal microscopy. Syntaxin 3 partially re-localizes to the basolateral membrane after nocodazole-treatment (+NZ) whereas the distribution of syntaxin 4 is unaffected. Immunolabeling of endogenous sec6 revealed that the distribution of this exocyst component is unaffected by MT disruption.

6. Discussion

6.1. Quantitative detection of single fusion events during constitutive exocytosis

In the past, the optical detection of single exocytic events was problematic. It was necessary to simultaneously apply additional techniques, such as capacitance measurements, to ensure that a fusion event was monitored. Furthermore, all efforts to image single fusion events was limited to regulated secretory systems. We have used a highly sensitive TIR-FM setup for the quantitative detection of single constitutive fusion events at the plasma membrane (Chapter 3). The use of an integral membrane protein rather than a luminal protein as a vesicle marker provided a novel method to clearly distinguish the behavior of a fusing carrier from that of all other carriers.

6.1.1. Summary of quantitative criteria for fusion:

The following quantitative criteria were established to distinguish between (i) fusing carriers, (ii) carriers moving perpendicular to the membrane, and (iii) carriers undergoing photolysis (Fig. 3.2 and 3.3).

(i) Fusion of a carrier with the plasma membrane is detected by the simultaneous rise of the total, peak and width of its fluorescence intensity. The rise of the total intensity describes the flattening process of the carrier into the plasma membrane, during which the fluorescent membrane cargo moves deeper into the evanescent field. When the cargo has been fully delivered, the total fluorescence intensity reaches a plateau. The fluorescence intensity is detected to have a Gaussian distribution in the moment of fusion start. Upon fusion start the area $[(width)^2]$ of the carrier fluorescence increases linearly after fusion start as the membrane proteins diffuse into the plane of the plasma membrane. The slope of this increase is the diffusion constant of the membrane protein.

(ii) In contrast, a carrier that moves perpendicular to the plasma membrane is detected as a change in total and peak intensity while the width of the intensity

remains constant.

(iii) A carrier that lyses would not deliver all its cargo to the plasma membrane, resulting, if at all, in a much smaller rise of the total intensity. Importantly, the cargo would disperse into the cytoplasm and not diffuse into the plasma membrane. This would lead to a rapid decrease rather than a plateau in the total fluorescence. The width might increase transiently as the cargo disperses and then become noisy during the loss of carrier fluorescence.

These quantitative criteria could not have been established with the more common techniques of wide-field epifluorescence or laser scanning confocal microscopy. In both these approaches the whole cell body is illuminated, whereas only the contact surface is illuminated in TIR-FM. It is because of the exponentially decaying evanescent field that we observe an increase in the total intensity during the flattening of the carrier. In epifluorescence or confocal microscopy, on the other hand, the total intensity of a post-Golgi carrier would not show any changes except when the carrier leaves the focal plane. Lastly, compared to the other techniques, TIR-FM does not cause any photo-bleaching and photo-damage in deeper parts of the cytosol. Thus, TIR-FM is extremely well suited for live imaging of surface events like exocytosis over extended periods.

6.1.2. Detection of fusion: Microscopic versus electrophysiological approach

Historically, exocytosis has been monitored with a variety of methods, including amperometry, biochemical secretion assays and electrophysiology. Of these, electrophysiology is the only method for the detection of single events. Electrophysiology has been used to study the formation and widening of the fusion pore. For that purpose two values have been measured: (i) the initial increase in conductance between the inside of a vesicle and the outside of the cell as the fusion pore opens, and (ii) the increase in capacitance as the vesicle membrane becomes continuous with the plasma membrane. The initial pore opening was found to be reversible and to occur within a few milliseconds (Spruce et al., 1990).

TIR-FM has allowed us to image and quantify, for the first time, the flattening

of the vesicle into the plasma membrane (Chapter 3), which occurs over a time scale ranging from hundreds of milliseconds to a few seconds (Table 3.1). Therefore, these two techniques complement each other by monitoring two different steps in the fusion process: the electrophysiological experiment monitors the opening of the fusion pore, while the optical experiment described here measures the time course of the carrier membrane flattening down.

Moreover, electrophysiological experiments do not provide accurate, if any, spatial information about exocytic events. In contrast, TIR-FM can be used to study the exact localization of fusion events, an advantage used extensively in this work.

6.1.3. Limitations of TIR-FM for monitoring exocytosis

While the inherent optical property of the evanescent field – to *only* illuminate the cell surface in tight contact with the substrate (coverslip) – is an advantage for the detection of fusion events, it can be a limitation in some applications. Using TIR-FM, we cannot detect fusion events in areas of either ‘loose’ contact, or at the opposite surface of the cell, simply because these areas are outside the evanescent field. In our experiments, we had to assume that the carrier fusions detected at the contact (basal) surface in the non-polarized cells (fibroblast, sub-confluent epithelial cells) are representative for the whole cell surface. In polarized epithelial cells, for example, the lateral and the apical membranes are far out of reach of TIR-FM. Therefore, we do not detect any fusion using TIR-FM in polarized MDCK cells (Chapter 5), because fusion occurs at the lateral or apical membrane. Here, techniques like confocal sectioning must be applied to follow the carrier dynamics. However, as discussed earlier, the quantitative microscopic detection of fusion is very limited with techniques other than TIR-FM.

Further, quantification of absolute fluorescence intensity values, for instance, to determine the total delivered membrane cargo during fusion (Chapter 3, Table 3.1), is problematic using TIR-FM. Each cell has a certain adhesion pattern, with some areas of the plasma membrane being closer and others further away from the coverslip. Therefore, the intensity of the evanescent field at the plasma

membrane can vary substantially between different areas of the contact surface. In our quantification, a statistical approach, i.e. the analysis of a large numbers of events from multiple cells, can compensate for such effects.

A possible way to overcome this limitation and to be able to quantitatively compare intensity values from different areas of the contact surface, is to simply know the relative intensity of the evanescent field in these areas. Since we are unable to easily measure the actual distance from coverslip to plasma membrane, we cannot simply calculate the intensity even if we know the decay constant of the evanescent field (Chapter 2). Dual-color TIR-FM could provide a solution to this problem. A permanent and uniform plasma membrane stain, imaged in a separate color channel simultaneously with the carrier channel, would provide an intensity map for the excitation of the evanescent field. According to this 'plasma membrane standard' the intensity values obtained from each carrier fluorescence could be easily compared. However, this experiment is limited to short time periods (minutes), because over longer time periods (> 30min) any plasma membrane stain (e.g. a fluorescent lipid analogue, such as Dil) will be endocytosed and recycled back to the surface, which could result in a confounding of the relative intensity values.

6.2. Structure of post-Golgi carriers

6.2.1. Morphology of post-Golgi carriers ranges between small spherical and long tubular carriers

In regulated exocytosis, considerable evidence has accumulated to favor a quantal vesicular model. For example, synaptic vesicles in the presynaptic terminal of neurons are very uniform in size (~40-50nm diameter), and upon stimulation, fuse and expel a quantal amount of neurotransmitter to the postsynaptic cells (Fatt and Katz, 1952; Del Castillo and Katz, 1954). In constitutive exocytosis, two different structures have been proposed as the post-Golgi carriers: small spherical and long tubular carriers (Hirschberg et al., 1998; Toomre et al., 1999). Our experiments, using a variety of biosynthetic membrane

proteins, support the presence of both. However, rather than representing two separate classes of carriers, they describe the two extremes of what we observe as a continuum of carriers of various spherical and tubular shapes and sizes. This was first seen using VSVG-GFP as a membrane protein marker (Table 3.1). Even though the ratio of vesicles to tubules varied between constructs and cell types, the initial findings with the membrane cargo protein VSVG-GFP are consistent with all other constructs used in this work (p75-GFP, LDLR-GFP, NCAM-GFP). As will be discussed later, the existence of tubular post-Golgi carriers was completely dependent on an intact MT cytoskeleton.

As might be expected, we found that a tubular carrier delivers much more membrane cargo to the plasma membrane than a small spherical carrier (Chapter 3). It remains to be determined if the cell is able to regulate the shape or length of the carrier according to the amount of cargo that needs to be transported from the TGN to the plasma membrane. The GTPase dynamin is known to be involved in post-Golgi carrier biogenesis. Expression of a GTPase defective mutant of dynamin allowed the formation of long tubules emerging from the TGN, but completely blocked the release of any post-Golgi carriers (vesicles and tubules) from the TGN (Kreitzer et al., 2000). It is possible that the regulation of dynamin, which is also known to take part in the formation of endocytic vesicles at the plasma membrane (Hinshaw, 2000), might be involved in 'shaping' the post-Golgi carriers.

6.2.2. Post-Golgi carriers can fuse at any point along their length

Recent discussions about the structure of post-Golgi carriers have suggested 'head' or 'tail' domains of tubular carriers (Stephens and Pepperkok, 2001; Toomre et al., 2000). Specifically, previous studies using time-lapse TIR-FM with a temporal resolution of ~0.5 frames/sec has suggested that tubular post-Golgi carriers can undergo "partial" fusions at their tip with the plasma membrane (Toomre, JCB 2000). The temporal resolution in our experiments is about 10x higher (~5 frames/sec). The time-lapse studies of "collapsing and fusing" tubules (Fig. 3.4, 4.4, 4.5) clearly show that the center of fusion is not necessarily at one

end of a tubule. This suggests that the formation of a fusion pore can be achieved anywhere along the tubule. This is consistent with the observation from recent correlative light-electron microscopy studies showing that post-Golgi carriers are highly amorphous structures, rather than simple cylindrical tubes, as seen in light microscopy (Polishchuk et al., 2000). Together these observations suggest that post-Golgi carriers can fuse at any point, wherever they are in close enough contact with necessary components of the fusion machinery at the plasma membrane.

6.3. Mechanism of constitutive exocytosis

6.3.1. Delivery and fusion of post-Golgi carriers occurs along MT

The observation that post-Golgi carriers are transported close to the cell surface along curvilinear paths shortly before they fuse with the plasma membrane (Schmoranzner et al., 2000), raised the question about the cytoskeletal element responsible for this transport just before fusion. Using high resolution time-lapse TIR-FM, we revealed several novel mechanistic aspects about the final delivery of post-Golgi carriers to the plasma membrane:

(i) MTs were labeled using either GFP- β -tubulin or tau-GFP (Chapter 4). Using TIR-FM, dynamic and static MTs were seen to approach the plasma membrane within a distance of <100nm in various tissue culture cell lines. This demonstrated that MTs – ends as well as intermediate sections – get close enough to transport vesicles to the plasma membrane of flat tissue culture cells. This result suggests that the actin cortex, which is thought to be impenetrable for the MTs, is either extremely thin (< 100nm) or can be penetrated by MTs in fibroblasts.

(ii) Using simultaneous dual-color TIR-FM we showed for the first time that post-Golgi carriers were transported to the site of fusion at the plasma membrane via MTs. This conclusion is based on a few observations:

- In all cases the fusion site could not be spatially resolved from the MT. In

other words, post-Golgi carrier fusions largely colocalized with the MTs.

- Tubular carriers were not observed when the MTs were disrupted. This suggests that the tubular shape of the carriers is a consequence of attachment at multiple points to the MTs. Indeed, in cells with intact MTs, tubular carriers were seen to maintain their morphology – and thus were most likely still attached to the MTs – until the initiation of fusion.
- The tubular carriers were seen to collapse into the point of fusion. This collapse followed the trajectory of the MTs. Collapse of the elongated tubule during fusion may coincide with release of putative MT attachments.

Together, these data suggest that transport and docking of post-Golgi carriers occur on the MTs. If this is the case, no other cytoskeletal element need necessarily be involved in the transport and docking prior to fusion.

(iii) Further we showed that post-Golgi carriers are capable of fusing at sites where the MT tracks are continuous. In other words the carriers do not have to reach the end of the MTs in order to fuse.

(iv) Examination of the motion of tubular carriers along MTs indicated that carriers can be attached to multiple MTs at the same time and can frequently switch between different MTs during transport. However, it remains to be resolved if there are certain types of MTs, which are preferred roadways for certain post-Golgi carriers. In migrating fibroblasts, for example, subsets of MTs are distinguished by their post-translational modifications, i.e. detyrosination of α -tubulin (Nagasaki et al., 1992). The observation that kinesin has a ~3-fold higher binding affinity to detyrosinated MTs compared to unmodified MTs suggests that there may be differences in transport rates of secretory vesicles along distinctly modified MTs (Liao and Gunderson, 1998).

6.3.2. Effects of microtubule depolymerization on post-Golgi traffic in fibroblasts

Depolymerization of the microtubule cytoskeleton is known to have multiple effects on the physiology and structure of mammalian cells. Aside from arresting basic cellular processes like mitosis and migration, the disruption of MTs also results in a reorganization of MT-bound organelles, including ER and Golgi. As

shown previously, MT depolymerization is followed by dispersion of the Golgi complex into functional 'mini-stacks' throughout the cytoplasm (Rogalski and Singer, 1984). These mini-stacks redistribute in close proximity to ER-exit sites or intermediate compartments (Cole et al., 1996), resulting in a maintenance of efficient secretory traffic.

We observed fusion in nocodazole-treated cells, in which the MT cytoskeleton was completely depolymerized. This is consistent with previous results showing that the bulk secretory traffic is maintained upon MT disruption. However, nocodazole treatment had multiple effects on the delivery of post-Golgi membrane cargo:

(i) Most importantly, the distribution of fusion sites was significantly altered by MT disruption. In untreated cells, fusion sites were widely distributed over the cell surface. However, after nocodazole treatment fusions were observed primarily in close proximity to the Golgi.

(ii) The nature of the post-Golgi carriers was altered upon disruption of the MTs. In control cells the morphology of the carriers ranged from small spherical to large tubular shapes. However, tubular carriers completely disappeared after nocodazole treatment.

(iii) The frequency of partial fusions (i.e. in which part of the fluorescent cargo remains behind after fusion) is low in control cells (~13% of total), but dramatically increased in nocodazole-treated cells (~54% of total).

(iv) The frequency of fusion decreased ~2-fold after depolymerization of the MTs.

(v) The amount of fluorescent cargo delivered per fusion increased ~2-fold after MT depolymerization.

These changes have further implications for the mechanism of transport and fusion in the absence of MTs. Delivery could be mediated either by direct fusion of Golgi mini-stacks or by tubular extensions off the stacks fusing directly to the plasma membrane. Alternatively, transport intermediates could bud off from the mini-stacks and fuse to the closest part of the plasma membrane. Either way, our results show that the intact MT cytoskeleton is necessary for directing

delivery of post-Golgi carriers away from the Golgi to the periphery of the cell. Further, delivery of post-Golgi cargo seems to be less controlled (more cargo delivered per fusion) and less efficient (lower fusion frequency and less complete fusions) in cells with disrupted MTs.

6.3.3. Is actin involved in constitutive exocytosis?

While the actin cortex has been suggested to play several roles in regulated exocytosis, our results do not indicate a significant role for actin in constitutive exocytosis. Neither the inhibition of myosin ATPases with BDM, nor the depolymerization of filamentous actin with cytochalasin-D, had a gross effect on transport, docking or fusion of post-Golgi carriers. The one change upon actin depolymerization or inhibition of the myosin ATPases was a slight decrease in the average time a carrier was docked adjacent to the membrane prior to fusion. Thus, in flat tissue culture cells like NRK fibroblasts, transport along filamentous actin seems not required for constitutive exocytosis. If it were required, a delay in docking time rather than an acceleration would be expected. This excludes the necessity of a 'dual-transport' mechanism in which single vesicles carry motors enabling transport on both MTs as well as actin filaments, leading to a 'hand-over' from the MTs to actin at the cortex (Bi et al., 1997; Rogers and Gelfand, 1998; Rodionov et al., 1998; Brown, 1999). Further, we propose that the actin cortex does not function as a significant barrier for the post-Golgi carriers to reach the plasma membrane. The slight decrease in docking time might be explained by the removal or weakening of the actin cortex, which is thin in fibroblasts. However, single actin filaments are very difficult to detect by fluorescence microscopy techniques in living cells and it remains possible that an undetectable amount of filamentous actin is sufficient for supporting constitutive exocytosis.

6.3.4. Is membrane tension involved in fusion?

A difference in membrane tension between the vesicle and the plasma membrane has been proposed to drive the fusion of the two membranes (Monck et al., 1990; Solsona et al., 1998; Markosyan et al., 1999; Siegel, 1999). The

ability to quantify the rate of vesicular flattening at high temporal resolution with TIR-FM could allow this model to be tested. Two current observations suggest that membrane tension might be involved in the fusion process of post-Golgi carriers.

First, the rate at which the width of the fluorescence spreads is sometimes faster during the flattening of the vesicle (the rise phase of the fluorescence) than it is during the subsequent diffusion of the marker protein (VSVG-GFP) into the plasma membrane (the spread phase) (see Fig. 3.3b and 3.4b). This suggests that the VSVG-GFP initially spreads into the plasma membrane at a rate faster than expected just by diffusion.

Second, tubular post-Golgi carriers are seen to collapse into the fusion site with a speed faster than any reported kinesin-dependent transport (Fig. 4.6b). This suggests that something other than MT motors plays a role in this process.

It has been proposed that cell surface area may be regulated by the local addition of membrane during exocytosis. In this model, exocytosis is used by the cell to compensate for high plasma membrane tension (Morris and Homann, 2001). High tension in the plasma membrane relative to the tubule membrane at the site of fusion could explain the acceleration of the tubular (or vesicular) carrier collapse. It could explain why large tubular carriers seem to be actively pulled towards their site of fusion. The equilibration of tension gradients, especially for small spherical carriers, would occur extremely quickly, potentially too fast to be resolved by standard imaging techniques.

It may be possible to optically resolve whether the accelerated flattening of the carrier membrane into the plasma membrane indeed results from release of membrane tension. Simultaneous dual-color TIR-FM could be used to image both the fusing carrier and the plasma membrane, the latter labeled with a fluorescent lipid dye, such as Dil. In case of an accelerated flattening process the plasma membrane marker would be excluded from the center of fusion because the flow of the carrier membrane would be faster than the diffusive mixing of the cargo protein into the labeled plasma membrane. To optically resolve this exclusion process, however, extremely high temporal resolution is required. This

is a potentially limiting factor of the microscopic approach.

6.3.5. 'Complete' and 'partial' fusions – 'kiss-and-run' in constitutive exocytosis?

The vesicular model of secretion, which states that secreted content is released in quantal packets by the fusion of membrane-bounded vesicles, was established by interpreting data from regulated systems, such as neurons or endocrine cells. Several years ago, data from capacitance measurements suggested that the fusion of large secretory granules can be a transient phenomenon, which was termed 'flickering fusion' (Fernandez et al., 1984; Breckenridge and Almers, 1987). In more recent years there have been a number of experiments indicating that, in regulated exocytosis, vesicles sometimes only transiently fuse and then move away from the fusion site, in what has been called "kiss and run" (Alvarez de Toledo et al., 1993; Meldolesi, 1998; Palfrey and Artalejo, 1998; Artalejo et al., 1998; Ales et al., 1999; Fesce and Meldolesi, 1999). In this model a fusion pore forms at the vesicle-plasma membrane contact, which then widens enough to allow the release of luminal components, but not the delivery of the whole vesicular membrane. In the case of neurotransmission, this mechanism of "kiss and run" does appear as a more efficient process than complete fusion, in which case endocytic retrieval of the vesicle membrane from the plasma membrane would be required after exocytosis.

In other systems, however, such as constitutive exocytosis of membrane cargo, the major goal may be to add the entire vesicle membrane, including all its lipids, proteins and carbohydrates, to the plasma membrane. Using TIR-FM to monitor constitutive exocytosis of a GFP-labeled membrane protein we observed that carriers deliver variable amounts of membrane protein to the plasma membrane. Our results from experiments on various cell types (COS-1, stationary NRK fibroblasts, sub-confluent MDCK cells) secreting various membrane proteins (VSVG-GFP, p75-GFP, LDLR-GFP, NCAM-GFP) indicated that, in constitutive exocytosis, most of the post-Golgi carriers fully fuse and integrate with the plasma membrane. We call this process 'complete fusion'. Only occasionally (~13% of all cases seen in NRK cells), we observe 'partial

fusions', in which not all of the membrane cargo is delivered, but a part of the carrier fluorescence is seen to remain at the site of fusion. Rarely, this residual fluorescence is seen to move away from the site of fusion, a process that has the characteristics of "kiss-and-run".

The question whether a general "kiss-and-run" mechanism exists in constitutive exocytosis is not possible to answer with our current system. By using a membrane marker only, it is not possible to quantitatively distinguish between, on the one hand, a carrier undergoing partial fusion, and on the other, two (or more) spatially unresolved carriers undergoing subsequent fusions. A method capable of distinguishing these scenarios must monitor both the discharge of luminal content during fusion pore opening (the "kiss"), and the delivery of the vesicle membrane to the plasma membrane (complete fusion). Simultaneous dual-color TIR-FM has these capabilities. In the case of complete fusion, both the luminal and the membrane cargo would diffuse away from the site of fusion, presumably at different rates (Fig. 3.1). In the case of "kiss-and-run", the luminal cargo would again rapidly dissipate, but at least part of the membrane cargo would remain in the vesicle membrane and then move away from the site of fusion. As discussed earlier, imaging of rapidly diffusing luminal cargo is expected to require high temporal resolution. However, preliminary results on various luminal markers (i.e. constitutively secreted insulin-GFP, fluorescent dextrans chased into lysosomes) show that it is possible to monitor the discharge with the current single-color setup. Further experiments will show whether it is possible to image both luminal and membrane cargo in simultaneous dual-color TIR-FM.

Other labs have combined the superior temporal resolution of electrophysiological capacitance measurements with imaging by TIR-FM. As an alternative method, the fusion pore opening could be resolved by capacitance measurements, while the flattening could be resolved by TIR-FM. However, these combined capacitance-fluorescence measurements on whole cells are very difficult and so far, have been performed only on regulated systems such as endocrine cells (Chow et al., 1994).

6.4. Domain-specific targeting of post-Golgi membrane cargo

A central problem in membrane traffic lies in the questions of how transport vesicles find and fuse to their target membrane (Rothman, 1994; Ferro-Novick and Jahn, 1994; Schekman and Orci, 1996; Jahn and Sudhof, 1999; Pelham, 2001). From the complexity and variety of intracellular organelles and the large number of possible trafficking routes between these organelles it is apparent that a system providing a high degree of specificity in membrane targeting is absolutely essential for maintaining cellular organization. In very basic terms, all membrane traffic involves a) the making (or budding) of a vesicle at the donor membrane, b) the transport of the vesicle to the target membrane and c) the fusion of the vesicle to its target membrane.

Simply stated, specificity could be independently achieved at any of these basic steps. During budding, the vesicle could be equipped with a specific protein necessary for fusion of the vesicle to its cognate target membrane. Alternatively, the budded vesicle could be bound to only a certain type of adapter-, motor- or cytoskeletal-protein, any of which could enable specific transport to only its target membrane. Lastly, specificity could be achieved via proteins that specifically tether the vesicle at the target membrane to enable docking and fusion. In fact, the wealth of current data on this subject suggests that all these trafficking steps are highly regulated and that specificity is introduced at many of these steps. Altogether this ensures a high degree of efficiency in correct membrane traffic.

During this work we studied targeted delivery of various membrane proteins from the Golgi to the plasma membrane in (i) migrating fibroblasts and (ii) polarized epithelial cells.

6.5. Targeted delivery in migrating fibroblasts

6.5.1 Migrating fibroblast have a MT-dependent mechanism for polarized exocytosis close to the leading edge

Directed membrane delivery has been proposed to be a critical component in cell growth, phagocytosis and cell migration (Lawson and Maxfield, 1995; Zakharenko and Popov, 1998; Bajno et al., 2000; Mellman, 2000). Specifically, directed membrane delivery to the leading edge has been suggested to be the driving force in cell migration (Bretscher, 1996). In this model, sites of endocytosis are thought to be randomly distributed over the cell surface, whereas both recycling as well as secretory vesicles are proposed to be directly delivered to the leading edge. This way, a net “forward” membrane transport would result in the extension of the leading edge, a process necessary for migration.

Early experiments demonstrated by immunofluorescence microscopy that newly synthesized VSVG is first delivered to the leading edge of motile fibroblasts (Bergmann et al., 1983). We confirmed this in experiments on living cells by showing directly that post-Golgi carriers containing LDLR-GFP are delivered preferentially close to the leading edge of migrating NRK fibroblasts (Chapter 4). Further we demonstrated that this polarized secretion is MT-dependent. Disruption of MTs dramatically restricts fusion to an area in close proximity to the Golgi/TGN thus making it impossible to distinguish between stationary (discussed below) and migrating cells based on distribution of fusion sites.

It is known that fibroblast migration (which includes pseudopodial activity, polarization of cell shape and redistribution of intracellular organelles) is suppressed as a result of either MT disruption or inhibition of MT-based transport with a function-blocking anti-kinesin antibody (Bershadsky et al., 1991; Rodionov et al., 1993). Our finding that polarized membrane delivery in migrating fibroblasts is also MT-dependent strongly suggests that this polarized delivery is a critical component for migration in fibroblasts. Thus, we provide support for the model proposing directed membrane flow to be the driving force in migration

(Bretscher, 1996). Our results do not resolve the question of whether membrane flow or actin polymerization is the primary driving force for migration. However, they demonstrate that localized exocytosis, which is required for the membrane flow hypothesis, occurs in migrating fibroblasts. Thus, the membrane flow model remains valid. Still, force generation during migration may be a result of both actin polymerization and membrane flow.

Recently, we demonstrated that single fusion events of vesicles originating from the endosomal recycling compartment could be detected by TIR-FM (Lampson et al., 2001). Thus, future experiments with TIR-FM could test the hypothesis that, in addition to the Golgi, the endosomal recycling compartment is a source for membrane cargo being sent in directed fashion towards the leading edge during migration.

6.5.2. No domain-specific exocytosis in stationary fibroblasts

We mapped the exocytic sites at the contact surface of stationary NRK fibroblasts (Chapter 4). In contrast to the migrating fibroblasts, fusion sites of post-Golgi carriers were distributed all over the cell surface of these non-polarized cells. We did not observe preferred sites or domains for constitutive exocytosis. Slight biases in some regions of individual cells were most likely due to a higher concentration of MTs in those regions. This idea is consistent with the results from Chapter 4, showing that post-Golgi carriers are transported along MTs to their fusion sites. Moreover, depolymerization of MTs in stationary cells results in redistribution of fusion sites to areas of plasma membrane close to the Golgi.

6.6. Targeted delivery in polarized epithelial cells

In this study we have used time-lapse TIR-, epi- and confocal fluorescence microscopy in live cells to address questions about post-Golgi trafficking events in the three-dimensional environment of polarized epithelial monolayers (Chapter 5). The main goal was to monitor changes in targeted exocytosis, of both apical and basolateral membrane proteins in MDCK cells, as a function of polarization. In addition, we investigated possible molecular effectors of these changes. Our results provide new insight into the current view of how epithelial cells organize their exocytic machinery during the establishment of polarity.

6.6.1 Targeted exocytosis of apical and basolateral membrane proteins changes upon polarization of MDCK cells

Using TIR-FM we detected exocytosis of either apical (p75) or basolateral (LDLR, NCAM) post-Golgi carriers at the basal membrane of non-polarized MDCK cells. Similar observations have been made in other non-polarized cells, for instance our experiments on stationary NRK fibroblasts (Chapter 4) as well as recently published observations that both apical (GPI anchored protein) and basolateral (VSVG) carriers fuse with the basal surface in sub-confluent PtK₂ cells (Keller et al., 2001).

Further we made the novel observation that exocytosis of both apical and basolateral membrane proteins at the basal membrane is completely abrogated in polarized MDCK cells. Since epifluorescence imaging revealed that apical and basolateral proteins accumulated in the correct plasma membrane domain, the loss of basal fusion indicated that carrier exocytosis was redirected, upon cell polarization, to other domains of the plasma membrane. Indeed, by imaging the 3-dimensional distribution of post-Golgi trafficking, we observed that carriers containing p75-GFP (apical) were confined to the uppermost 1.5-3 μ m of cells, whereas carriers containing LDLR or NCAM (basolateral) were more broadly distributed throughout the upper half of the cytoplasm. The narrow, sub-apical distribution of apical carriers suggests an association with the sub-apical MT array. In contrast, the wider distribution of basolateral carriers in the apical

cytoplasm could reflect their emergence from an apically localized Golgi complex and association with cytoskeletal elements other than MTs.

Using dual-color confocal microscopy we were able to directly visualize the fusion of basolaterally-targeted carriers with the lateral membrane. Consistent with movements of carriers being restricted to the most apical half of the cytoplasm, all of the lateral membrane fusion events we detected were also confined to the apico-lateral membrane. These experiments are, to our knowledge, the first direct demonstration of targeted exocytosis to the lateral plasma membrane of polarized cells. Technical limitations hampered direct observation of apical carrier fusion. However, our results show that carriers containing p75-GFP do not fuse either with the basal membrane or with regions of the lateral membrane where basolateral carriers exocytose.

6.6.2 The t-SNAREs syntaxin 3 and 4 spatially correlate with apical and basolateral membrane cargo, respectively.

Abrogation of exocytic events at the basal plasma membrane and redirection to the lateral membrane upon cell polarization correlated with changes in the distribution of presumed molecular components of the apical and basolateral fusion machineries. Basal fusion of post-Golgi carriers occurs only in non-polarized cells, when syntaxins 3 and 4 are present at the basal membrane. However, basal fusion stops completely after polarization, when both syntaxins no longer localize to the basal membrane. In polarized cells, syntaxin 3 and 4 localize exclusively to the apical and lateral membrane, respectively. These results suggest that syntaxins 3 and 4 are required at the target membranes for fusion of apical and basolateral carriers to occur. In neurons, for example, the t-SNAREs syntaxin 1A localize throughout the cell surface, yet secretion selectively occurs at the axon terminal (Foletti et al., 2000). Similarly, syntaxin 4 localizes throughout the lateral membrane in polarized MDCK cells yet we only observed fusion of basolateral carriers within the top 1/2 - 1/3 of the lateral membrane. Our data are consistent with the idea that t-SNAREs are necessary for fusion of carriers but additional factors are involved in domain-specific targeting (Hazuka et al., 1999; Waters and Pfeffer, 1999; Lowe, 2000). One of

these additional factors could be the exocyst, which localizes to apical regions of the lateral membrane and was recently demonstrated to have an important role in basolateral membrane trafficking in MDCK cells (Hazuka et al., 1999; Lipschutz et al., 2000; Lowe, 2000). Thus, our data support the concept that the exocyst acts in concert with the SNARE machinery to specify sites of basolateral exocytosis in polarized MDCK cells. Possibly, proteins implicated in establishing apical membrane domains during *Drosophila* and *C. elegans* development could act as targeting/tethering sites at which syntaxin 3 mediated apical fusion can be activated (Bilder et al., 2000; Bilder and Perrimon, 2000).

6.6.3 The delivery of apical, but not basolateral, cargo is MT-dependent.

Another striking finding we made was that, in polarized cells, apical post-Golgi carriers regained the ability to fuse with the basal membrane upon depolymerization of MTs. This was paralleled by the relocalization of syntaxin 3 to the basal membrane upon MT disruption. It is possible that the mistargeting of p75-GFP to the basal membrane is a direct consequence of syntaxin 3 mislocalization to the basal membrane in response to MT-antagonists.

In contrast, MT depolymerization did not promote fusion of carriers containing either LDLR-GFP or NCAM-GFP with the basal membrane. Furthermore, the lateral distribution of sec6 and syntaxin 4 were preserved under these conditions. Our results are consistent with studies showing that MT-disruption preferentially affects apical targeting pathways in epithelial cells (Hugon et al., 1987; Achler et al., 1989; Gilbert et al., 1991). The results demonstrate that MTs are not required for maintenance of the polarized basolateral exocytic machinery.

In summary, these time-lapse studies of polarized exocytosis in MDCK cells document striking changes in the organization of post-Golgi trafficking during epithelial differentiation and provide evidence for how protein targeting may be achieved. Our data advances the current understanding of how apical and basolateral membrane proteins are delivered to their correct target membrane in

polarized MDCK cells in several ways:

(i) We show that after polarization, apical and basolateral carriers become spatially segregated in the cytoplasm when they emerge from the Golgi. This confirms the idea that apical and basolateral proteins are sorted at the TGN for transport to separate plasma membrane domains. It remains to be clarified, whether epithelial cells in general possess this sorting ability even in a non-polarized state, or whether polarization itself effects this segregation.

(ii) Apical and basolateral carriers never fuse to the basal membrane in polarized cells. From this observation we can eliminate the possibility that basolateral carriers, at least for LDLR and NCAM, are transported directly to the basal membrane ('B' in Fig. 5.1c). Instead, basolateral carriers are delivered directly to sites at the lateral membrane ('BL'). It remains to be resolved whether apical carriers are delivered to either sites at the apico-lateral membrane ('AL') or to sites of the apical membrane close to the microvilli ('A').

(iii) The restricted delivery of post-Golgi carriers in polarized cell is in contrast to non-polarized cells, where extensive fusion of carriers containing either apical or basolateral cargo is seen at the basal membrane.

(iv) The t-SNAREs, syntaxin 3 and 4, are present at the target membranes of post-Golgi carriers loaded with apical and basolateral proteins, respectively. This suggests that the t-SNAREs selectively effect the fusion of apical and basolateral post-Golgi carriers.

(v) After MT-disruption, apical carriers fuse with the basal membrane, while basolateral carriers are still targeted to the lateral membrane.

(vi) In parallel, after MT-disruption the t-SNARE syntaxin 3 (apical) become mislocalized to the basal membrane, while syntaxin 4 (lateral) stays on the lateral membrane. This suggests that MTs mediate the delivery of both syntaxin 3 and apical carriers to the apical membrane, but not syntaxin 4 and basolateral carriers to the lateral membrane. The mechanism by which basolateral targeting remains intact in the absence of MTs is unresolved.

6.7. Post-Golgi traffic in fibroblasts and epithelial cells – A similar mechanism ?

Non-polarized (sub-confluent) epithelial cells and stationary (confluent) fibroblasts are similar in their morphology, MT-organization and post-Golgi traffic. Both cell types show a rather central nucleus and perinuclear MTOC from which a polarized radial MT array extends with its plus end towards the periphery of the cell. Further, these cells show similarities in their post-Golgi traffic. In both cell types we observed the fusion of carriers containing either apical or basolateral membrane cargo with the membrane which is in contact with the coverslip⁷. In non-polarized MDCK cells, this observation is paralleled by the non-targeted distribution of the t-SNAREs, syntaxins 3 and 4. This suggests that the 'random' fusion is due to the 'random' distribution of syntaxins. Currently, it is not known which t-SNAREs (syntaxins) are involved in the fusion of post-Golgi carriers in fibroblasts. It is also unclear whether the fusion of carriers loaded with specific membrane proteins is mediated by specific t-SNAREs, in these cells.

Using biochemical methods, it has been proposed that non-polarized cells, like fibroblasts, have – similar to polarized epithelial cells – cognate post-Golgi routes for apical and basolateral membrane proteins (Musch et al., 1996; Yoshimori et al., 1996). Recent results based on dual-color live cell microscopy on non-polarized PtK₂ cells underline this idea by showing that apical (GPI-anchor) and basolateral (VSVG) proteins leave the TGN in separate post-Golgi carriers (Keller et al., 2001). However, whether this observation can be generalized for all non-polarized cells and whether there is a certain degree of promiscuity in the sorting of different proteins for post-Golgi traffic in non-polarized cells has still to be clarified. The current observations have to be tested

⁷ Apical and basolateral are defined by the exclusive localization of a protein to either the apical or basolateral membrane in fully polarized epithelial cells. These terms are also used to describe the same proteins in a non-polarized cell, even though it is clear that a non-polarized cell does not have separate apical and basolateral membrane domains. For simplicity, the contact surface of a non-polarized cell is often called the 'basal' surface. In fact, the term 'basal' is defined in epithelial cells as the surface that is in contact with the extra-cellular matrix and that contains all the basolateral proteins.

using many different proteins expressed in different cell types. Recent results suggest that the apical sorting machinery is more complex than expected – even post-TGN sorting of two different apically targeted proteins can occur (Jacob and Naim, 2001). In future experiments the protein-specific exit and sorting kinetics must be studied in more detail to give a clearer picture of the sorting efficiency at the TGN or post-TGN level.

It is currently unresolved whether migrating fibroblasts, which indeed have a polarized cell shape, do in fact deliver apical and basolateral membrane cargo to different domains of the plasma membrane. Our experiments show that migrating fibroblasts execute polarized post-Golgi membrane traffic towards the leading edge, which is likely to facilitate, if not mediate, migration. We demonstrate this with LDL receptor as a reporter, which is exclusively localized to the basolateral surface of polarized epithelial cells. It has been suggested that apical cargo in migrating fibroblasts could be segregated away from basolateral cargo, and delivered to random places or even to distinct sites away from the leading edge (Keller and Simons, 1997). Preliminary data suggests that the apical marker (p75-GFP) is also directed toward the leading edge in migrating fibroblasts. Therefore, it seems unlikely that fibroblasts actually have a functional separation of ‘apical’ and ‘basolateral’ membrane proteins, as epithelial cells do. Dual-color TIR-FM can be used to determine whether apical and basolateral membrane cargo are in fact sorted into separate carriers at the TGN before they fuse with the plasma membrane.

Details of the mechanism that leads to enhanced exocytosis close to the leading edge of migrating fibroblasts remain to be resolved. It may be that the MT cytoskeleton provides a preferred “highway” system for the post-Golgi carriers toward the leading edge. Alternatively, the domain around the leading edge could be preferentially equipped with necessary components of the docking and fusion machinery. Again, this could be mediated by the MT cytoskeleton, as seems to be the case with syntaxin 3 in polarized epithelial cells. It will be of great importance to identify the components of the fusion machinery involved in constitutive traffic to the plasma membrane.

6.8. Imaging components of the fusion machinery

During the last decade, studies on membrane traffic have provided a wealth of knowledge about the possible molecules involved in specific membrane fusion (Jahn and Sudhof, 1999; Pelham, 2001; Chen and Scheller, 2001). For the most part, two families of molecules, the rab/ypt GTPases and the SNAREs (soluble NSF attachment protein receptor, where NSF stands for N-ethyl-maleimide-sensitive factor) stand out. Recent *in vitro* studies on yeast proteins in purified membrane systems provide data supporting the hypothesis that cognate SNARE pairs mediate specificity and that the fusion complex is made up of target (t) and vesicle (v) SNAREs (Fukuda et al., 2000; Parlati et al., 2000; McNew et al., 2000). A strict 3:1 ratio of t-/v-SNARE-helices seems accepted, at least *in vitro* (Pelham, 2001). How far these *in vitro* data resemble the more complex *in vivo* situation is far from being resolved. Most likely, rab GTPases play an important role for the initial tethering of the vesicles, and SNARE proteins, being able to form very tight helical complexes, are likely to be involved in the fusion process itself. However, the necessary and sufficient components of the fusion machinery *in vivo* are still not known.

TIR-FM in live cells could play an important role in resolving the question of specificity. The colocalization of GFP-tagged SNAREs, rabs and cargo molecules in TIR-FM could provide *in vivo* evidence for the localization of these proteins during fusion. In this work, TIR-FM was used solely to image constitutive exocytosis. As shown previously, it can be used to image regulated exocytosis as well, the advantage being that the exocytic event can be triggered within a short time. For example, the fusion machinery during the release of secretory vesicles in neuron-like cells (PC-12 cells) or the Ca^{2+} -dependent secretion of lysosomes during wound healing could be studied. As shown in Chapter 7, TIR-FM can also be used for detecting the arrival of vesicles at the surface during the recycling of endosomal cargo.

By imaging the colocalization of various components of the fusion machinery

in time-lapse TIR-FM, the *in vivo* assembly of the tethering/fusion machinery could be imaged. Important questions are: Do the carriers/vesicles always bring along their v-SNAREs? Which tethering molecules (rabs) are involved and when relative to the SNARE core complex are they recruited? Are the t-SNAREs already locally assembled (clustered) in the target membrane or must they be 'collected' by the v-SNAREs of the vesicle moving in close proximity to the target membrane? On this note, initial imaging studies on cell free membrane sheets derived from PC12 cells suggest that there are submicron clusters of syntaxins pre-assembled at the plasma membrane which are preferred docking and fusion sites for secretory granules (Lang et al., 2001).

One major challenge for *in vivo* experiments is to construct functional GFP-tagged members of the trafficking/fusion machinery, which do not perturb complex intracellular membrane traffic. Initially, colocalization studies on fixed cells might provide important insight into the SNARE or rab proteins that are associated with specific cargo molecules, including membrane and luminal cargo. Ultimately, FRET (Fluorescence Resonance Energy Transfer) experiments could reveal detailed molecular interactions, e.g. the formation of the core complex. Given the current discussions about specificity of membrane traffic, it would not be surprising if identical SNARE proteins are used for multiple pathways, while the specificity is achieved by additional factors involved in domain-specific transport and tethering of vesicles.

7. Insulin-Regulated Release from the Endosomal Recycling Compartment is Regulated by Budding of Specialized Vesicles

7.1. Introduction

Reversible retention in the endosomal system is a mechanism for cells to rapidly modulate levels of proteins on the cell surface. For any protein recycling through the endocytic pathway, the kinetics of internalization and recycling determine the distribution between the plasma membrane and intracellular compartments. A change in either of these rates causes a rapid redistribution. Several specialized cell types exploit this mechanism to move enzymes and transporters to the cell surface (Cannon et al., 1985; Bradbury and Bridges, 1994). Examples include translocation of aquaporin-2 in collecting duct cells of the kidney (Knepper and Inoue, 1997; Ward et al., 1999) and of an H⁺K⁺-ATPase in gastric parietal cells (Forte and Yao, 1996), which are important for water and acid secretion, respectively.

One of the most intensively studied examples of hormone-induced translocation is the effect of insulin on surface levels of the GLUT4 glucose transporter in muscle and fat cells (Czech, 1995; Rea and James, 1997). GLUT4 is dynamically retained inside cells because it is rapidly internalized and slowly recycled. Insulin stimulation reverses the retention by increasing the recycling of GLUT4 to the plasma membrane, thereby effecting an increase of GLUT4 on the surface and a concomitant increase of glucose transport (Jhun et al., 1992; Satoh et al., 1993; Yang and Holman, 1993). In fat and muscle, GLUT4 recycles back to the cell surface through a specialized insulin-responsive compartment that is distinct from the general endosomal recycling system (reviewed in (Rea and James, 1997; Pessin et al., 1999)). When GLUT4 is expressed in fibroblasts, it is also retained intracellularly and redistributes to the surface in response to insulin, which demonstrates that non-specialized cells have the capacity for insulin-regulated recycling (Kanai et al., 1993; Lampson et al., 2000). Although the physiological significance of regulated endocytic traffic in fibroblasts is not

clear, the insulin-regulated pathway may be functionally important in many cell types for translocation of the insulin responsive aminopeptidase (IRAP), which is the only other protein known to traffic like GLUT4 in fat and muscle cells (Kandror and Pilch, 1994; Keller et al., 1995; Ross et al., 1996; Malide et al., 1997; Martin et al., 1997; Sumitani et al., 1997; Garza and Birnbaum, 2000). Unlike GLUT4, IRAP is expressed in many cell types. IRAP's physiological function is unknown, but one possibility is that insulin stimulation exposes IRAP to extracellular substrates.

We used three reporter molecules to investigate the retention mechanism in CHO cells (Fig. 7.1). The first is the transferrin (Tf) receptor (TR), a widely used marker for the general endocytic pathway, which recycles rapidly from the endosomal recycling compartment (ERC) to the plasma membrane. The second, vpTR, has the transmembrane and extracellular domains of the TR and the cytoplasmic domain of IRAP (Subtil et al., 1999; Johnson et al., 2001). Thus, vpTR also binds Tf, but it recycles slowly because of the trafficking information encoded in the cytoplasmic domain of IRAP (Johnson et al., 1998). The third reporter is a GLUT4 construct with an exofacial HA epitope and a C-terminal GFP (HA-GLUT4-GFP) (Lampson et al., 2000). We have previously shown that both vpTR and HA-GLUT4-GFP follow the reversible, insulin-regulated dynamic retention pathway in CHO cells (Johnson et al., 1998; Lampson et al., 2000; Johnson et al., 2001). In this study we used HA-GLUT4-GFP as a marker for the

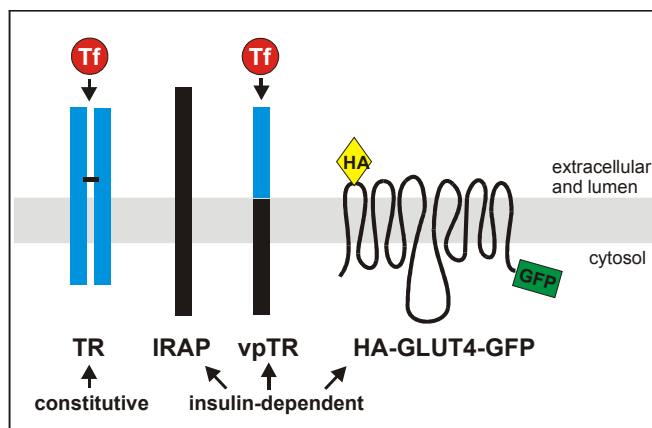


Figure 7.1. Constructs used to study insulin-dependent recycling. Illustrated are the constitutively recycled transferrin receptor (TR), the insulin-responsive aminopeptidase (IRAP), the chimera of the extracellular domain of TR and the transmembrane and intracellular domains of IRAP (vpTR), and the glucose transporter 4 (GLUT4) with an HA-tag at the extracellular loop and GFP on the cytoplasmic C-terminus.

retention pathway, and either the TR or vpTR to deliver fluorescent Tf-conjugated probes. The advantage of this combination of reporters is that the insulin-dependent reporter GLUT4 can be directly compared to the insulin-independent reporter TR and to the insulin-dependent reporter vpTR.

TIR-FM has been shown to be suitable for direct detection of surface delivery of membrane cargo in living cells (Chapter 3, (Schmoranzner et al., 2000)). Using dual-color TIR-FM in combination with the above described reporter proteins we address a fundamental questions about the insulin-regulated retention pathway in CHO cells. How are these proteins (TR, vpTR, GLUT4) delivered to the plasma membrane with different kinetics from a single compartment? Analysis of individual transport vesicles by TIR-FM demonstrates that GLUT4 and vpTR traffic in the same vesicles, while the TR is in separate vesicles. Using an independent fluorescence quenching assay, we showed previously that GLUT4, vpTR, and the TR are all contained in the ERC (Lampson et al., 2001). Together, these observations provide the first evidence for separate budding events from the ERC that generate two classes of vesicles directed to the plasma membrane. These data support a single model for the reversible insulin-regulated retention mechanism in fibroblasts.

7.2. Results

In an independent set of experiments it was shown that, (i) co-expression of the insulin-regulated HA-GLUT4-GFP in CHO cells does not affect the trafficking of TR and vpTR, (ii) all reporter proteins (GLUT4, vpTR and the TR) are contained in the endocytic recycling compartment in CHO cells, and, (iii) recycling along the retention pathway (vpTR) occurs as a single kinetic pool from a peri-nuclear retention compartment. All the experiments leading to the above conclusions are described in detail previously (Lampson et al., 2001).

Given that the ERC is the retention compartment, there are two possible models for recycling of the TR and vpTR/GLUT4 at different rates from a single compartment. In the first model (Fig. 7.2a) two distinct classes of transport

vesicles bud from the ERC, one rapidly and one slowly. vpTR and GLUT4 are concentrated in the slowly-budding vesicles, while the TR recycles in the rapidly-budding vesicles. Insulin would increase the recycling of vpTR and GLUT4 by increasing the budding rate of the slow vesicles. This model does not require active concentration of the TR in the rapid vesicles. Because they bud more frequently, any molecule not actively excluded or concentrated elsewhere would recycle primarily in these vesicles. In the second model (Fig. 7.2b) only one class of transport vesicles exists, and the slow recycling of vpTR and GLUT4 is achieved by excluding these molecules from the budding sites. The recycling rate of vpTR and GLUT4 would be determined by the efficiency of sequestration, and insulin would act by releasing the retention, allowing vpTR and GLUT4 to recycle with the TR.

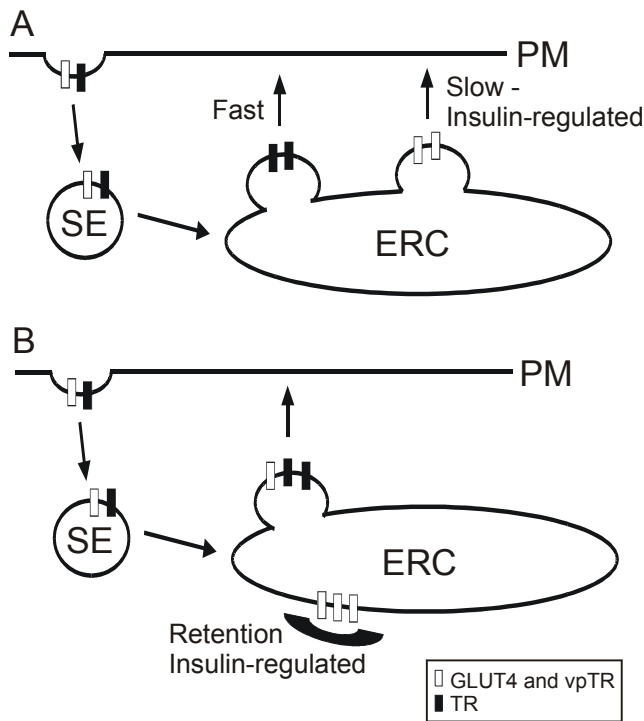


Figure 7.2. Models for retention in the endocytic recycling compartment.

(A) Two classes of vesicles bud from the ERC. The TR recycles in rapidly-budding vesicles ("Fast"), while GLUT4 and vpTR are concentrated in separate, slowly-budding vesicles. Insulin increases the budding rate of the slow vesicles. (B) Only one class of vesicles buds from the ERC. GLUT4 and vpTR are retained in the ERC by exclusion from these vesicles. However, slow recycling of GLUT4 and vpTR does occur due to inefficient retention. Insulin releases the retention, allowing GLUT4 and vpTR to recycle with the TR. (ERC = endocytic recycling compartment, SE = sorting endosome, PM = plasma membrane)

The two models make different predictions about the contents of vesicles recycling from the ERC: either GLUT4 and the TR are separate (first model) or together (second model). To test these predictions, we used dual-color total internal reflection fluorescence microscopy (TIR-FM) to analyze the contents of

transport vesicles (Chapter 2, methods). With this technique only fluorophores within the evanescent field, which extends up to ~125nm from the glass surface into the aqueous media, are excited, so only compartments or transport intermediates close to the plasma membrane are observed. This method has been used previously to analyze fusion of post-Golgi transport intermediates with the plasma membrane (Chapter 3).

Cells expressing HA-GLUT4-GFP (green) and either the TR or vpTR were imaged by TIR-FM following uptake of Cy3-Tf (red). Both color channels were imaged simultaneously using the emission splitter described in chapter 2. Post acquisition image processing resulted in the co-aligned dual-color images (methods). vpTR and GLUT4 are clearly co-localized near the plasma membrane, indicated by yellow/orange structures (Fig. 7.3a). As both of these molecules follow the slow recycling pathway, we expect colocalization in transport intermediates. There is no reason to expect the intensities of the two probes to be at a constant ratio; therefore, the structures do not all appear equally yellow. The TR and GLUT4, however, are in distinct red and green structures (Fig. 7.3c). These data suggest that the TR and GLUT4 are delivered to the plasma membrane in separate transport intermediates.

Time-lapse TIR-FM (~5 frames/sec) showed static structures, vesicles and tubules moving parallel to the plasma membrane, and vesicles appearing and disappearing (see video 7.3). The static structures may either be docked vesicles or parts of the ERC that are within the evanescent field. To further analyze the data we quantified the co-distribution of probes in transport intermediates, which we defined as moving vesicles.

Moving vesicles containing one of the fluorophores were selected by looking at a single color, so that the selection would not be biased by knowledge of the other color. Vesicles selected for GLUT4 (i.e., green) are designated here as GLUT4 vesicles, and those selected for Tf content (red) are Tf vesicles. The fluorescence intensity of each color was averaged over all the pixels in the vesicle in a single image. A population of these vesicle intensities is shown graphically, plotted as average green versus average red fluorescence for each

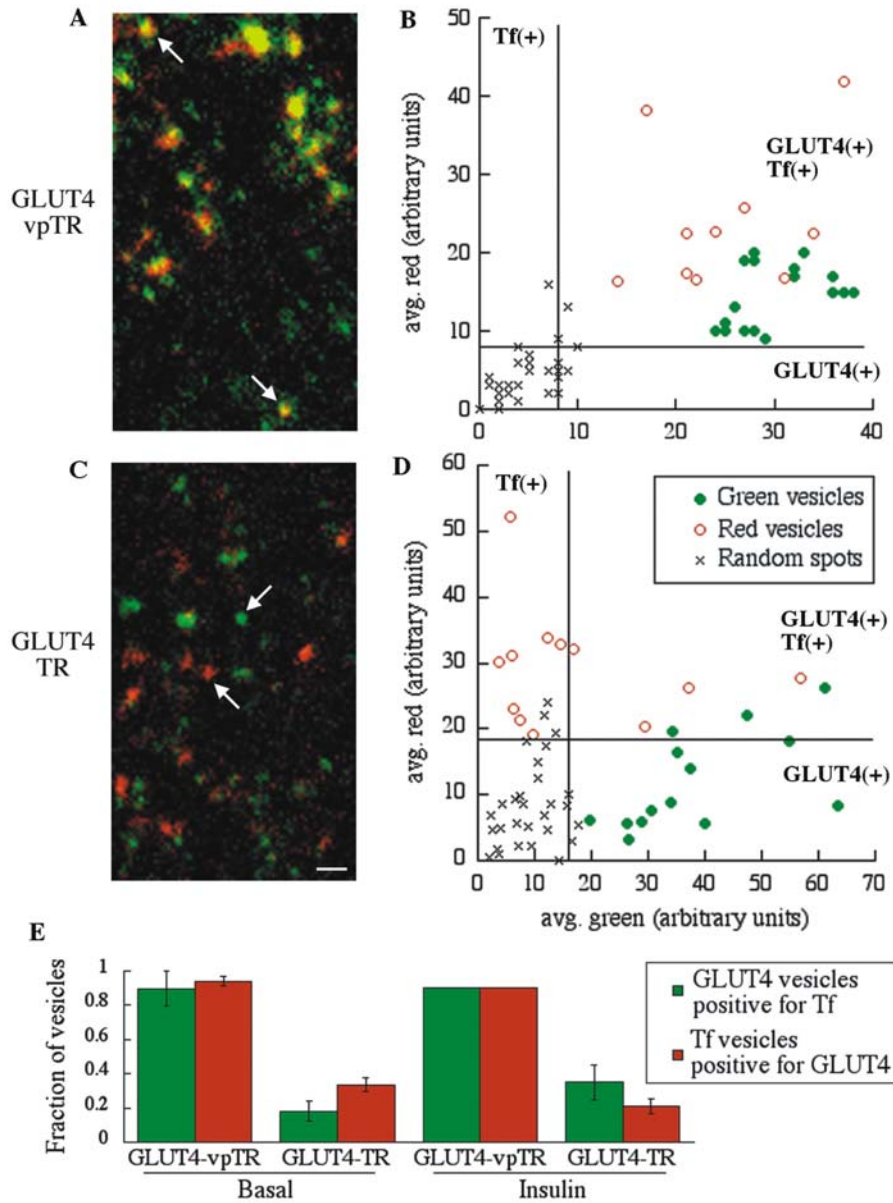


Figure 7.3. The TR is segregated from GLUT4 in transport vesicles imaged by TIR-FM (see videos). Cells expressing HA-GLUT4-GFP and either vpTR (A,B) or the TR (C,D) were loaded with Cy3-Tf and imaged by time-lapse TIR-FM. (A,C) Representative images showing structures containing GLUT4 (green), Tf (red), or both (yellow). Structures in (A) do not all contain the same ratio of vpTR to GLUT4, so they do not all appear completely yellow. Scale bar = 1 μ m.

(B, D) Moving vesicles were selected for either GLUT4 content (solid green circles) or Tf content (open red circles). For each vesicle the average green intensity is plotted against the average red intensity, calculated over all the pixels in the vesicle. The intensities units are not comparable between the two plots. Spots randomly placed throughout the image represent background (x). Lines indicate threshold intensities, calculated from the random spots, to separate signal from background. Based on these thresholds, the quadrants are labeled as GLUT4(+) or Tf(+) to indicate where the intensities are higher than background.

(E) The fraction of GLUT4 vesicles positive for Tf and Tf vesicles positive for GLUT4 is shown for the two cell types, both with and without insulin. The fractions are averaged over multiple videos in all cases, with at least 15 vesicles analyzed from each video. Error bars represent either the SEM of three or more determinations or the difference between two determinations.

vesicle (Fig. 7.3b and d). To represent the background fluorescence, red and green intensities were also calculated for randomly placed spots of the same average size as the vesicles. In cells expressing vpTR (Fig. 7.3b), the green and red intensities in all vesicles are higher than the background, by comparison to the random spots, which implies that the GLUT4 vesicles contain Tf and vice-versa. In cells expressing the TR (Fig. 7.4d), however, the GLUT4 vesicles generally have background levels of Tf, and the Tf vesicles have background levels of GLUT4. These data show graphically that vpTR and GLUT4 are delivered to the plasma membrane together, as expected, while the TR is segregated in separate vesicles. The segregation is not complete, as some vesicles contain both the TR and GLUT4.

We classified each vesicle as positive or negative for each fluorophore, based on a threshold intensity determined from the random spots (methods). We calculated the percentage of GLUT4 vesicles positive for Tf and the percentage of Tf vesicles positive for GLUT4, and the percentages were averaged over multiple cells (Fig. 7.3e). In cells expressing the TR, few of the GLUT4 vesicles contain Tf and few of the Tf vesicles contain GLUT4; but in cells expressing the vpTR, nearly all of the vesicles contain both probes. Finding a near complete overlap of vpTR and GLUT4 vesicles is important since it demonstrates that the vast majority of GLUT4-containing vesicles we observe are derived from the endosomal system (i.e., labeled by Tf internalized from the plasma membrane) rather than from the biosynthetic pathway.

These data support the model proposed in Fig. 7.2a, in which GLUT4 and vpTR are trafficked in vesicles distinct from those that transport the TR. These findings are inconsistent with the model in Fig. 7.2b, which predicts that the slow recycling of GLUT4 is due to inefficient retention, so that some “leaks out” in vesicles with the TR. In this case some of the TR vesicles could contain detectable GLUT4, as observed (Tf vesicles positive for GLUT4), but all the GLUT4 vesicles should contain TR (GLUT4 vesicles positive for Tf). As only a small fraction of the GLUT4 vesicles contain TR, this model can be eliminated.

Insulin does not alter the distribution of GLUT4 and the TR (Fig. 7.3e), which

suggests that although insulin increases the recycling of GLUT4 and vpTR, it does not do so by redistributing these proteins to the rapidly recycling TR-containing vesicles. These data also argue against the model in Fig. 7.2b, which predicts that GLUT4 and the TR should recycle in the same vesicles following insulin stimulation.

In the two-color TIR-FM we frequently observed vesicles appearing and disappearing in the evanescent field. However, we were unable to score these as fusion events if we applied the criteria for vesicle fusion previously developed (Chapter 3). In the previous studies the post-Golgi carriers were more intensely labeled, allowing detailed quantitative analysis of the vesicular flattening and the diffusion of the membrane cargo into the plasma membrane. In this current study, to avoid possibly saturating the retention mechanism for GLUT4 and vpTR, we have used stable cell lines expressing the proteins at moderate levels. At these expression levels of the constructs and the current technical limitations of two-color TIR-FM imaging, we were unable to distinguish fusion events from vesicles rapidly disappearing from the evanescent field.

To establish that the TR, vpTR and GLUT4 vesicles fuse with the plasma membrane, we used single-color TIR-FM. With single-color imaging the fluorescence signal is brighter, so we were able to acquire images at a higher rate and with a higher signal-to-noise ratio. We used GFP to examine the HA-GLUT4-GFP-containing vesicles, and Alexa⁴⁸⁸-Tf to label the TR or vpTR in CHO cells expressing only the TR or vpTR. In all three cases the intensity of the signal in single-color TIR-FM was sufficient to observe fusion (see Fig. 7.4 for examples). As shown previously, fusing vesicles were identified by a simultaneous increase in total and width of the fluorescent intensity, as the vesicles flatten into the plasma membrane and the membrane cargo diffuses. This characteristic pattern was observed for each of the probes used in this study. These data indicate that at least a portion of the moving vesicles observed in the dual-color TIR-FM are transport intermediates between the ERC and the plasma membrane.

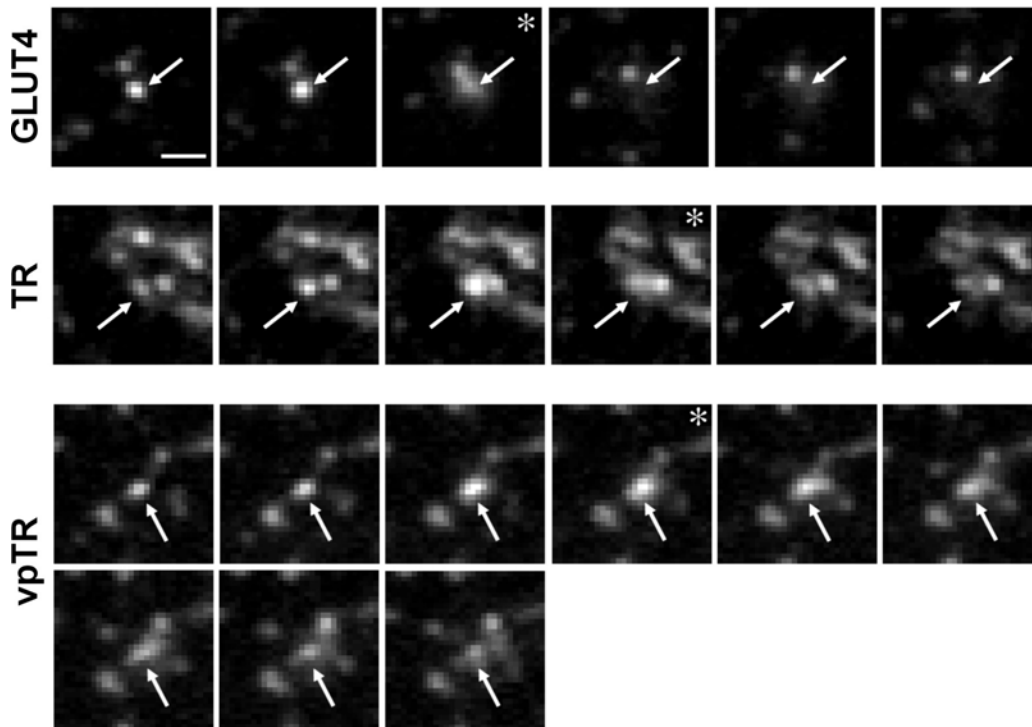


Figure 7.4. Fusion of transport vesicles imaged by TIR-FM. Cells expressing either HA-GLUT4-GFP, the TR, or vpTR were imaged by TIR-FM. Cells expressing the TR or vpTR were first loaded with Alexa⁴⁸⁸-Tf. Sequential frames (6-10 frames/sec) are shown for each probe. Arrows indicate vesicles that fuse during the sequence. Asterisks mark the frames of the fusion start, identified by a simultaneous increase in total and width of the fluorescence intensity. Scale bars = 1 μ m.

7.3. Discussion

We have shown previously that TR and vpTR are recycled from the same compartment, the ERC, as single kinetic pools with different rates in CHO cells. This suggests two possible models for the different recycling kinetics of the insulin-independent recycling TR and the insulin-dependent recycling GLUT4 and vpTR. In one case there are two classes of vesicles, one carrying the TR and one carrying vpTR and GLUT4, that transport cargo from the ERC to the plasma membrane at different rates (Fig. 7.2a). Alternatively, there is a single class of vesicles, but vpTR and GLUT4 are slowly recycled because they are sequestered in the ERC and excluded from these vesicles (Fig. 7.2b). Based on the TIR-FM data, we can eliminate the second possibility because we find the TR

and GLUT4 in separate vesicles (Fig. 7.3). Thus, the data are consistent with a single model in which the budding rates of distinct transport intermediates from the ERC determine the kinetic differences observed between the recycling of the TR and vpTR. In this model the TR recycles in rapidly-budding vesicles, while GLUT4 and vpTR are concentrated in distinct, slowly-budding vesicles. Insulin would reverse the retention of GLUT4 and vpTR by increasing the budding rate of the slow vesicles.

Our data provide the first direct evidence for sorting of proteins into distinct transport intermediates in the ERC of non-polarized cells. This process may be similar to the sorting that occurs in endosomes of polarized cells, in which proteins internalized from apical or basolateral membranes are delivered to a common endosomal compartment (Futter et al., 1998; Gibson et al., 1998; Orzech et al., 2000; Wang et al., 2000). In these cells sorting into separate vesicles is required for delivery of recycling proteins to distinct membrane domains, rather than for the kinetic purpose described here. Clathrin-coated pits and γ -adaptin have been implicated in this process (Futter et al., 1998; Gibson et al., 1998), but the mechanism has not been well characterized and the required trafficking motifs are unknown.

We have recently identified the motifs required for dynamic retention of vpTR as a di-leucine sequence and a cluster of acidic residues (Johnson et al., 2001). These motifs serve as a specific signal for vpTR to escape the bulk-flow recycling pathway followed by the TR (Mayor et al., 1993). We proposed that an adaptor protein recognizes the motifs and links the cargo, vpTR, to the appropriate coat proteins. The results reported here support a model in which this recognition occurs in the ERC and serves to concentrate vpTR in distinct vesicles. Several observations are consistent with the idea of specialized vesicles budding from a common endosomal compartment in non-polarized cells. Both clathrin and COP-1 coat proteins, as well as the AP-1 complex, have been localized to endosomes (Whitney et al., 1995; Aniento et al., 1996; Le Borgne et al., 1996; Stoorvogel et al., 1996; Dell'Angelica et al., 1998). Different rab proteins, which are known to regulate trafficking, have also been localized to distinct endosome domains

(Sonnichsen et al., 2000). The roles of these proteins are not well understood, but one possibility is that they regulate the formation and release of distinct classes of vesicles.

Sorting of proteins into separate transport vesicles has been extensively studied along the biosynthetic pathway. Polarized cells are thought to sort proteins for delivery from the TGN to the apical or basolateral plasma membrane (reviewed in (Keller and Simons, 1997; Ikonen and Simons, 1998)), and a similar sorting process has been proposed in non-polarized cells (Musch et al., 1996; Yoshimori et al., 1996; Keller et al., 2001). Our data suggest that the ERC may play an analogous role as a sorting station in the endocytic pathway by retaining vpTR and GLUT4 while allowing other proteins to recycle rapidly. Supporting this role of the ERC, there is evidence that proteins can be sorted to specific intracellular compartments, as TGN38 traffics from the ERC to the TGN (Ghosh et al., 1998). Further characterization of the adaptor and coat proteins involved in trafficking from the ERC and from the TGN will allow a more detailed comparison of the sorting events at these two compartments.

8. Materials and Methods

This section is organized into a general section about the TIR-FM system and cell culture used in all experiments, followed by separate sections that describe the materials and methods specifically used in each chapter.

8.1. TIR-FM setup

The objective-type TIR-FM system consists of a modified inverted epifluorescence microscope (IX-70, Olympus America Inc., Melville, NY) equipped with high numerical aperture (N.A.) objectives (Apo 100x 1.65 N.A. and Apo 60x 1.45 N.A., Olympus) (see photograph in appendix). The main modification necessary for single-color TIR-FM was the laser beam delivery system (Fig. 2.4). The beam from an air-cooled Argon-ion laser (Omnichrome, model 543-AP A01, Melles Griot, Carlsbad, CA) is coupled into a single-mode optical fiber (SM, OZ Optics LTD, Ontario, Canada) and remotely delivered to the setup, which is located in the adjacent room to prevent acoustical and mechanical noise. The beam diverging from the end of the fiber is passed through a mechanical shutter (S), collimated by a convex lens L1 ($f = 10\text{cm}$) to yield a Gaussian spot size of $\sim 2\text{cm}$. This beam is then cropped by a field diaphragm (FD) to control the illuminated area in the plane of the sample, attenuated with neutral density filters (ND), and reflected off two mirrors (M1, M2) to the dichroic mirror (DM) of the microscope. A convex lens L2 ($f = 20\text{cm}$) in the beam path is used to focus the laser beam onto the back focal plane (BFP) of the objective, so that it emerges collimated from the lens. This ensured that all rays are incident upon the sample at the same angle. The mirrors (M1, M2) are tilted to change the incident angle of the laser beam onto the TIR interface.

The focusing lens L2 is attached to the microscope stage with an x-y-z translator for convenient alignment of TIR. Further, the whole setup – illumination system and microscope – is mounted on an optical anti-vibration table. The field diaphragm to adjust the illumination area is positioned in the back focal plane of L2. This way the position of the beam in the image plane did not change during

repositioning of the laser beam in the BFP. All optical mounts (including reflective mirrors and lenses) were obtained from Thorlabs Inc. (Newton, NJ).

8.1.1. Alignment and verification of TIR-FM

The successful alignment of the TIR-illumination was established and tested qualitatively using fluorescent beads (~100nm diameter, Molecular Probes) suspended in distilled water. The following procedure was used:

- The objective was focused onto the plane of the coverslip in epi-illumination.
- The laser beam was moved with M1 and M2 such that it passed straight through the objective and the sample. Viewed from above the sample, the beads lit up along the path of the beam.
- The laser beam was focused by L2 such that it emerged collimated from the objective. Visually, the fluorescent path is collimated i.e. not diverging.
- The 'Bertrand lens' was inserted to monitor the back focal plane (BFP), which in this laser position is a bright circle. The beam appears as a spot in the center of the BFP.
- Looking at the BFP, M2 was tilted such that the beam moved towards the rim of the BFP. TIR was achieved when the beam entered the outer rim of the objective. At this point the center area of the BFP darkened and the rim lit up. In addition, a second beam occurred at the opposite side of the BFP. This was the total internally reflected beam reentering the objective.
- The beam was positioned in the outer 1/2 of the rim. If the beam is moved too far to the outside of the objective, it hits interior mounting material resulting in uncontrolled scattering and a perturbation of the TIR. Depending on the objective, the width in which TIR was achieved varied. As discussed in Chapter 2, the NA 1.65 objective has a wider range than the NA 1.45 objective.
- The 'Bertrand' lens was removed such that the beads could be monitored.
- In TIR-FM, two types of fluorescent spots (beads) were observed:
 - **Static spots:** These were the beads stuck to the coverslip and continuously illuminated by the evanescent field (EF).

- **Blinking spots:** These were the beads that bounced in and out of the evanescent field (EF) as a result of diffusion in the aqueous environment.
- As a simple test for TIR, the objective was defocused to a plane above the EF. In correct TIR-illumination, the image (the adherent beads) immediately appeared out-of-focus and became blurry and dark. If the TIR illumination was 'clean', no beads were visible in focal planes other than the plane of the EF. The beads in the suspension were outside the EF, therefore no continuous motion of diffusing beads was observed. In cases where these criteria were not reached, the TIR-beam was readjusted by switching back and forth between the BFP and the sample image.

8.1.2. Estimation of the evanescent field depth

The setup was aligned in TIR-FM mode. The aqueous medium was replaced with a right angled prism (hypotenuse facing up). The prism was coupled with immersion liquid (100x objective $n=1.78$, 60x objective $n=1.51$) to the sample side of the coverslip. Since the refractive index of the prism ($n=1.55$) is much higher than the refractive index of water ($n=1.33$), the critical angle was not reached. A screen was positioned vertically beside the setup, such that it was hit by the laser beam refracted through the prism. The horizontal and vertical distances between the center of the objective and the point where the beam hit the vertical screen were measured. From these distances the incident angle at which the beam leaves the objective was determined by applying Snell's law. The position of the incident beam in the BFP of the objective was adjusted to estimate the range of incident angles over which TIR occurred. The decay constants were calculated from the incident angles according to the formula discussed in Chapter 2.

8.1.3. Switching between TIR and EPI illumination

For most experiments on live cells, both illumination types, epi (beam straight through the sample, EPI) and total internal reflection (TIR) are required. EPI was used to check the total level of fluorescence inside a cell, for example the expression level of the GFP probe in ER and Golgi, and TIR was used for looking

at the signal at the coverslip contact surface only. We facilitated both types of illumination by raising the stage of the microscope to introduce a custom-made manual slider for an additional TIR dichroic mirror (prototype Olympus). Currently, the switch between both illumination types is manual. Efforts are underway to install a shutter-controlled EPI/TIR illuminator (Olympus).

8.2. Multi-color TIR-FM

The multi-color TIR-FM system was described in Chapter 2. It includes the single-color setup, the multi-laser combiner and the emission splitter. The specifications are:

Lasers: All lasers were obtained from Melles Griot (Carlsbad, CA): HeCd 442nm (Omnichrome, model 4056-S-A02), Argon Ion (Omnichrome, model 543-AP A01), HeNe 534nm (model 05-LGR-193), HeNe633 (model 05-LHR-991).

Lenses: The lenses and optical mounts were obtained from Thorlabs Inc. (Newton, NJ). L1 and L2 were replaced with achromatic lenses, Ach1 (f = 11cm) and Ach2 (f = 20cm), respectively.

Emission splitter: The emission splitter (W-view, Hamamatsu Photonics, Japan) was described in Chapter 2 (Fig. 2.5b). After the acquisition the two channels were separated and aligned using off-line software (methods of Chapter 4).

8.2.1. Fluorescence filters

The filters used for all the single-color and dual-color TIR-FM experiments are listed in Table 8.1. All filters for single and dual-color TIR-FM were obtained from Chroma Technologies Corp. (Brattleboro, VT).

Table 8.1: Summary of filter combinations used in single and dual-color TIR-FM

Fluoro-phore	Excitation [nm]	Excitation Di(poly)chroic	Emission Dichroic	Emission Bandpass
GFP	488	490dclp	--	HQ525/50M
CFP/YFP	442/514	442/514pc	510dclp	HQ480/40M / HQ550/50M
GFP/Cy3	488/(543)	488/543pc	550dclp	HQ525/50M / HQ570lp

8.2.1.1. Single-color: GFP

Excitation: GFP was excited using the 488nm line of the Argon-laser. The line was reflected off a dichroic mirror (490dclp).

Emission: The GFP emission was collected through emission band pass filters (HQ525/50M or HQ550/100M).

EPI illumination: For EPI illumination of GFP, the light from a Xenon arc lamp (Opti-Quip Inc., Highland Mills, NY) was passed through a heat filter and a bandpass filter (HQ488/10X). The emission was viewed through either a bandpass (HQ525/50M) or a long pass (500lp) emission filter.

8.2.1.2. Dual-color TIR-FM

For simultaneous dual-color imaging of CFP/YFP (Chapter 4) and GFP/Cy3 (Chapter 6), two separate laser lines were combined using the multi-laser combiner and the emission was split in two separate channels onto the same CCD.

CFP/YFP

Excitation: CFP was excited by the 442nm line of a HeCd laser. YFP was excited by the 514nm line of the Argon laser. The laser lines were combined via a dichroic mirror (455dclp). Both lines (442nm and 514nm) were reflected off a polychroic mirror (442/514pc).

Emission: The CFP/YFP emissions were separated using the emission splitter equipped with dichroic mirrors (510dclp) and emission band pass filters (CFP: HQ480/40M, YFP: HQ550/50M).

EPI illumination: For EPI illumination of YFP, we used the same filters as for GFP excitation. For EPI illumination of CFP, a bandpass filter (D430/25) and a polychroic mirror (442/514pc) were used.

GFP/Cy3

Excitation: GFP and Cy3 were both excited using the 488nm line of the Argon-laser. In some experiments the 543nm line from the HeNe 543 laser was used in addition to the 488nm line to excite Cy3. In that case, both lines

(488/543) were reflected off a polychroic mirror (488/543pc).

Emission: The GFP/Cy3 emission were collected simultaneously through an emission splitter equipped with dichroic mirrors to split the emission (550dclp) and emission band pass filters (GFP, HQ525/50M, YFP, HQ570lp).

EPI illumination: For EPI illumination, we used the same filters as for GFP excitation.

During dual-color experiments, all emission filters essential for capturing separate emissions on the camera were installed in the emission splitter, which is positioned between the microscope and camera. For viewing the emission by eye during such a dual-color experiment, additional emission bandpass filters were inserted just after the dichroic turret to cut out the excitation light reaching the eyepiece (not listed).

8.3. Image acquisition

Images were acquired with a 12-bit cooled CCD (either Orca I, C4742-95, pixel-size = $(6.7\mu\text{m})^2$, or ORCA-ER, pixel-size = $(6.45\mu\text{m})^2$, Hamamatsu, Bridgewater, NJ). Both CCD arrays had 1024x1280 pixels. The camera, the NI-IMAQ 1424 image acquisition card (National Instruments, Austin, TX) and a mechanical shutter (Uniblitz, Vincent Associates, Rochester, NY) were controlled by in-house software written in LABVIEW™5.1 using the IMAQ Vision package (National Instruments). The maximum speed of image acquisition during continuous illumination of the sample depended on the binning mode for both cameras. For Orca I: 30 frames/sec (4x4 binning), 18 frames/sec (2x2 binning) or 9 frames/sec (no binning). For the Orca-ER: 29 frames/sec (4x4 binning), 17 frames/sec (2x2 binning) or 8 frames/sec (no binning). The Orca ER, which has a higher sensitivity than the Orca I, was used for the experiments described in Chapters 4, 5 and 7. The acquisition speed used in each experiment was chosen such that post-Golgi carriers were clearly visible above background. Most data in chapter 3 were acquired at full speed (~30 frames/sec) in 4x4 binning mode. Most data in chapters 4, 5 and 6 were acquired at ~5 frames/sec at full resolution (no

binning).

Images containing a region of interest of the cell were streamed to memory on a PC during acquisition and then saved to hard disk. The reviewed data was copied onto CD ROM for data storage. Since the fast and continuous image acquisition creates an extremely large amount of data (~100-500 kB per image, depending on size of ROI and the binning mode of the camera), the number of frames acquired per continuous sequence was limited by the size of the memory.

8.3.1. Temperature control and light protection

Live cell imaging requires the conditions to be as 'physiological' as possible. One major parameter is temperature. The sample temperature needs to be above 32°C for traffic to proceed at roughly physiological rates. There are various ways of reaching physiological temperature of the sample. First, the sample holders can be heated. This can result in inaccurate temperature distribution across the sample, especially if the objective itself functions as a large heat sink through the immersion oil. An additional heater for the objective can prevent this, but it can also result in damaging temperature gradients within the objective.

Problems related to temperature-control were prevented using a home-built microscope enclosure made of inexpensive material (see photograph in appendix). A metal rod scaffold above the microscope was covered with thermally insulating and optically opaque foam sheets (McMaster-Carr, New Brunswick, NJ). In addition to this hood, all metal parts of the microscope body exposed to the outside were insulated as well. The focus knob and stage translator remained accessible from the outside. The temperature was controlled by an air-stream heater (Air Therm, World Precision Instruments, Sarasota, FL) blowing hot air into the lower right corner of the enclosure. This enclosure is similar to the setup described in (Inouye and Spring, 1997) and resulted in stable temperature control ($\pm 0.1^\circ\text{C}$) with minimal focal drift after 30min of preheating time. Each time a new sample is mounted onto the stage, slight focal drifts might occur for a couple of minutes depending on the initial temperature of the sample.

8.4. Cell culture

COS-1 (African Green Monkey, American Type Culture Collection, Rockville, MD), Normal rat kidney (NRK) fibroblasts, Madin-Darby Canine Kidney (MDCK) cells were maintained in DMEM (Mediatech Cellgro, Va, AK) with 10% FBS (BCS for NRK) at 37°C in a humidified 5% CO₂ incubator. For imaging, cells were plated 48 hrs prior to transfection or nuclear microinjection on either pre-cleaned special coverslips (LAFN21 or SF11) for imaging with the 100x NA 1.65, or on glass bottom dishes for imaging with the 60x NA 1.45 objective. The glass bottom dishes were either homemade by gluing (RTV Sealant, Dow Corning) a coverslip (Fisher Scientific, Pittsburgh, PA) onto a hole drilled into a 35mm tissue culture dish, or pre-made (MaTek Corp., Ashland, MA). To promote adherence on glass of COS-1 cells, the coverslips were coated with fibronectin (Life Technologies, Rockville, MD) according to the manufacturer's protocol. For NRKf and MDCK cells this step was found to be unnecessary.

8.5. Chapter 3: Detection of single fusion events

8.5.1. Transfection and ER exit block

COS-1 cells were transiently transfected with the plasmid VSVG-GFP ts045 (Presley et al., 1997) using FuGENE™ 6 (Boehringer Mannheim, Mannheim, Germany) according to the manufacturer's protocol. At 12h post transfection, cells were shifted from 37°C to 40°C for 24-36h to accumulate the VSVG-GFP in the endoplasmic reticulum. For imaging the temperature was shifted to 32°C. Cells were imaged in modified MEM without phenol red (Sigma, St. Louis, MO) with 10% FBS.

8.5.2. Image processing and quantitative analysis

All image processing and analysis was done using in-house software written in LABVIEW™5.1 using the IMAQ Vision package (National Instruments). Image analysis to obtain the total intensity, peak intensity and the width of the carrier

was performed with in-house software. For analysis of single fusion events, each acquired sequence (1000-2000 frames) was reviewed multiple times on screen at various settings of the intensity look-up table to pick out all visible events. The coordinates for each fusion event were determined by identifying the local maximum of fluorescence intensity. Only a small region of interest around each fusion site was used for further analysis. These were selected such that they were both large enough to yield a good Gaussian fit of the carrier fluorescence, and small enough to prevent the influence of other fluorescent particles on the analysis. All fusion sequences were analyzed in the following manner:

- The **center of mass** of the carrier was tracked for the entire sequence within a manually selected circular region.
- The radial intensity distribution $I(r)$ of the carriers was fit for each frame with a non-linear Levenberg-Marquardt routine to the **Gaussian: $I(r) = I_0 \exp(-r^2/w^2) + BG$** where r is the distance of each pixel to the **center of mass**. The fitting parameters are I_0 , w and BG , where I_0 is the peak intensity, BG is the background intensity, and w is the measure of the Gaussian width.
- The **total intensity of the vesicle** was computed by integrating the background-subtracted intensity over the entire region of interest.
- The **fusion start** was defined as the frame at which the second derivative of the smoothed total intensity was maximal.
- The **rise time** of the total intensity was the time difference between the fusion start and the frame where the smoothed total intensity reached its maximum within 5%.
- The **diffusion constant** was calculated by taking the carrier at the fusion start to be an instantaneous point source for diffusive material (Crank, 1995). The intensity profile as a function of time is then given by:

$$I(r,t) = \frac{I_0}{2\pi Dt} \exp\left(-\frac{r^2}{4Dt}\right).$$

- The square of the **width of this Gaussian**, $4Dt$, is linear over time t , with the slope proportional to the diffusion constant D .

8.5.3. Calculation of the ratio $TI_{\text{flat}}/TI_{\text{spherical}}$

The total fluorescence intensities for a flattened (TI_{flat}) and a spherical ($TI_{\text{spherical}}$) vesicle are directly proportional to the excitation intensity of the evanescent field $I(z)$, which decays exponentially from the coverslip into the cell: $I(z) = I_0 \exp(-z/d)$. Here, z is the distance from the coverslip, I_0 is the intensity in the plane at $z = 0$ and d is the decay length of the evanescent field. The total intensities for the flat and spherical configurations are calculated by integrating the excitation field $I(z)$ over a circular disk of radius R (flat) and a sphere of radius r (spherical; note that $2r=R$), respectively:

$$TI_{\text{flat}} = cI_0(4\pi R^2) \quad TI_{\text{spherical}} = c2\pi R \int_0^{2R} dz I_0 \exp(-z/d)$$

The constant c depends on the quantum yield and extinction coefficient of the fluorophore and the collection efficiency of the lens. After evaluating the integral and taking the ratio we find:

$$\frac{TI_{\text{flat}}}{TI_{\text{spherical}}} = \frac{2R}{d} \frac{1}{1 - \exp(-2R/d)}$$

8.6. Chapter 4: Post-Golgi traffic in fibroblasts

8.6.1 Cell culture and experimental wound

For microscopy on stationary NRK fibroblasts, cells were plated at a high enough density such that they reached confluency within 1-2 days. Only cells in contact with their neighboring cells were chosen for microscopy. For imaging migrating fibroblasts, an experimental wound was scraped through a densely confluent monolayer with a sterile pipette tip. Cells at the edge of the wound were allowed to recover for 2-3 h at 37°C. Only cells with clearly polarized morphology, large lamellipodium and nucleus away from the edge, were chosen for microinjection. MDCK cells were microinjected before they reached confluence.

8.6.2. Plasmids

All constructs made using PCR methods were checked by sequencing.

p75-GFP: The cDNA encoding the neurotrophin receptor p75 fused to GFP (in the vector pEGFP-N1, Clontech) was provided by G. Kreitzer and has been described previously (Kreitzer et al., 2000).

p75-YFP: The cDNA encoding p75 was subcloned from p75-GFP into the vector pEYFP-N1 (Clontech) using Apa1 and EcoR1 digestion.

LDLRa18-GFP: The cDNA encoding LDLRa18-GFP was obtained from Geri Kreitzer (see methods Chapter 5).

GFP- β -tubulin: The cDNA encoding GFP- β -tubulin was obtained from Clontech.

tau-GFP, tau-CFP: The plasmids encoding neuronal tau fused to GFP and CFP were a gift from Mombaerts lab (Rockefeller University, NY).

8.6.3. Nuclear microinjection and Golgi exit block

Before plating cells for nuclear microinjection, the coverslips were carefully marked with a cross by scratching the surface with a diamond tip. This facilitated localization of microinjected cells for imaging. Cells were microinjected using micropipettes pulled from borosilicate glass (1mm outer diameter, 0.78mm inner diameter) (Sutter, Novato, CA) on a P-87 puller (Sutter). The cDNA for various fluorescent chimeric proteins was diluted (p75 - 5 μ g/ml; LDLRa18 - 15 μ g/ml; β -tubulin - 10 μ g/ml; tau - 10 μ g/ml) in nuclear injection buffer (140mM KCl, 10mM HEPES pH 7.4), back-loaded into the micropipette, and injected into cell nuclei under constant pressure. The micropipette was positioned using a micromanipulator (Narishige, Greenvale, NY). After injection cells were maintained at 37°C in a humidified CO₂ environment for 60 min to allow for expression of injected cDNAs (“pulse”, Fig. 4.4). Newly synthesized protein was accumulated in the Golgi/TGN by incubating cells for ~3h at 20°C in bicarbonate-free DMEM supplemented with 5% serum and 100 μ g/ml cycloheximide (“chase”, Fig 4.4). Cells were transferred to recording medium (Hanks Balanced Salt Solution, supplemented with 20mM HEPES, 1% serum, 4.5 g/L glucose, 100 μ g/ml cycloheximide). After shifting to the permissive temperature for

transport out of the Golgi (32°C), the arrival of post-Golgi carriers labeled with p75-GFP or LDLRa18-GFP was monitored by time-lapse total internal reflection fluorescence microscopy.

8.6.4. Drug treatments

Cycloheximide, nocodazole, 2,3-butanedione-monoxime (BDM) and cytochalasin-D were obtained from Sigma (Sigma Chemicals, St. Louis, MO). Stock and working concentrations are listed below.

Drug	Solvent	Stock conc.	Working conc.
Cycloheximide	Water	1 mg/ml	100 µg/ml
Nocodazole	DMSO	10 mg/ml	10 µM
BDM	Water	0.5 M	10 mM
Cytochalasin-D	DMSO	1 mM	1 µM

8.6.5. Image processing and quantitative analysis

Processing and analysis of the time-lapse sequences was done either with in-house software written in LABVIEW™6.1 using the IMAQ Vision package (National Instruments, Austin, TX) or with MetaMorph (Universal Imaging, Downingtown, PA).

Temporal pseudo-color processing (Fig. 4.5b): Since the MT motion is slow compared to the movement of carriers, we separated the two fluorescent objects temporally by using a running average algorithm as part of in-house software written in Labview. A running average with a half width of 20 frames was performed on the original sequence. The resulting sequence was called the MT channel, because most of the carrier motions were averaged out and only MTs remained. Further processing was done in MetaMorph. The MT channel was subtracted from the original sequence to yield the carrier channel, showing only the fast moving objects. The MT channel was independently processed with the function 'Sharpen', yielding clear MT tracks. Both channels were pseudo-

color encoded (carrier = red, MT = green) and the maximum signal of each pixel over the entire sequence was merged into one image, resulting in the overlay of the carrier tracks on the MT tracks.

Quantification of colocalization of fusion sites with MT tracks in temporal dual-color TIR-FM (Fig. 4.5b): To confirm colocalization of fusion sites with MT tracks we measured the average intensity of the MT channel in small regions (3x3pixels) around each fusion site (n = 14). As a control we measured the average intensity in the MT fluorescence channel within regions that were devoid of MTs. The ratio of the MT signal at the fusion sites to the background MT signal was ~50, indicating a clearly positive correlation between carrier fusion sites and MTs.

Dual-color processing (Fig. 4.5c): The original dual-color sequences were acquired through the emission splitter such that the separated channels appear side by side on the camera chip. Processing was done in MetaMorph. Identical regions were cut out of the whole frame to yield separated image sequences. The two channels (CFP and YFP) were aligned within accuracy of one pixel by using a brightfield image of the same cell. The YFP channel was corrected for the amount of bleed-through from the CFP channel, which was found to be roughly 50% of the CFP signal. The noise was reduced by performing background subtraction, sharpening and running average. Finally, the separate channels were pseudo-color encoded and combined to an RGB sequence.

Quantification of co-localization of fusion site of tubular carrier (p75-YFP) with MT tracks (tau-CFP) in simultaneous dual-color TIR-FM (Fig. 4.5e): To quantify the colocalization of the tubular carrier (Fig. 4.5c, red) with the MT tracks (green) just before fusion, we calculated the average correlation coefficient between both channels for the whole region. To test the quality of correlation, the channels were shifted relative to each other in single pixel steps (~110nm) up to a maximum shift of about +/-1.1 μ m in x- and y-direction. The resulting values for the correlation coefficient of all four shift-directions were averaged and plotted (Fig. 4.5e).

Mapping of fusion sites: The sites of fusion were mapped manually by

using in-house software written in LABVIEW™6.1. By systematically cropping the whole field of view into small easily viewable areas the time-lapse sequences were viewed repeatedly with different look-up tables to localize the fusion events. The times of docking and fusion start, as well as the coordinates of the fusion sites were catalogued. The coordinates were plotted in Origin® (OriginLab Corp., Northampton, MA) and then overlaid with the epifluorescence image of the cell taken just after shift to 32°C.

8.7. Chapter 5: Post-Golgi traffic in epithelial cells

8.7.1. Cell Culture

For analysis of non-polarized MDCK cells, cultures were seeded at a density of ~13,000 cells/cm² onto heat sterilized 25mm round coverslips and grown for 36hr prior to microinjection. For polarized cell analyses, cells were seeded at a density of ~130,000 cells/cm² and grown for 4-5 days to insure the formation of a fully polarized monolayer prior to microinjection. The intranuclear microinjection of the cDNA (p75-GFP, LDLRa18-GFP, 20µg/ml for NCAM-GFP) and the accumulation of the proteins in the Golgi/TGN at 20°C were described above (methods Chapter 4).

8.7.2. DiIC¹⁶ plasma membrane labeling

Cells were microinjected as described. Fluorescently labeled DiIC¹⁶ (Molecular Probes, Eugene, OR) was added (final concentration, 50µM) to bicarbonate-free DMEM without serum, supplemented with 20mM HEPES and 100µg/ml cycloheximide. DiIC¹⁶-containing medium was added to the cells during the final 30 minutes of the 20°C Golgi block. Cells were then washed 3x with recording medium prior to time-lapse imaging.

8.7.3. Microtubule depolymerization

Prior to microinjection, cells were incubated in bicarbonate-free DMEM supplemented with 5% FBS and 20mM HEPES on ice for 30 minutes to

depolymerize the cold-labile, nocodazole-resistant MT population. Nocodazole was added to a final concentration of 20 μ M and the cells were incubated another 30min on ice. This treatment completely depolymerized all MTs (not shown). cDNAs were then microinjected and cells were treated as described above except that they were maintained in 10 μ M nocodazole for the remainder of each experiment to prevent re-assembly of the MT cytoskeleton.

8.7.4. Plasmids

All constructs made using PCR methods were checked by sequencing.

p75-GFP: p75-GFP cDNA has been described previously (Chapter 4, (Kreitzer et al., 2000)).

NCAM-GFP: The cDNA encoding full length neural cell adhesion molecule (NCAM) in pBKCMV was a gift from J. Bruses (Memorial Sloan Kettering Cancer Center, NY, NY). The construct encoding NCAM-GFP in pEGFP-N1 (Clontech) was prepared by G. Kreitzer (Cornell University, NY).

LDLa18R-GFP: The cDNA encoding full length, endocytic recycling defective low density lipoprotein receptor (LDLR-a18) in pCB6 was provided by Karl Matter (University College of London, London, England). The cDNA encoding the fusion protein LDLR-a18-GFP was prepared by Yunbo Gan (Cornell University, NY).

Syntaxin 3 and 4: MDCK cell lines stably transfected with human syntaxins 3 or 4 were provided by Seng Hui Low, Zhizhou Zhang and Thomas Weimbs (Lerner Research Institute and Urological Institute, Cleveland Clinic, Cleveland, OH). The syntaxin cDNA had been subcloned into a modified pcDNA4/ pcDNA4/TO vector (Invitrogen) to add two C-terminal myc epitope tags in tandem and one hexahistidine tag to the C-termini. The additional epitope-tags did not interfere with the correct polarized targeting of the syntaxins and allowed detection at the plasma membrane by surface immunolabeling.

8.7.5. Time-lapse TIR-FM

The single-color TIR-FM system has been described above. For these experiments the 60 \times 1.45 NA objective was used. Time-lapse sequences were acquired at a frame rate of ~5 frames/sec with full resolution of the CCD.

8.7.6. Time-lapse epifluorescence microscopy

After microinjection and subsequent Golgi block, cells were transferred to a Sykes-Moore thermal-controlled chamber (Bellco Glass Inc, Vineland, NJ) mounted on a Nikon E-600 upright microscope (Nikon Inc., Melville, NY) at 20°C and the temperature was then shifted to 32°C. The cells and culture medium were allowed to equilibrate to 32°C for 5 min prior to beginning the time-lapse recordings. GFP fluorescence was imaged directly with a fluorescein filter cube (B-2E/C DM 505, Chroma). Images were collected using a back-illuminated, cooled CCD camera with 15µm pixels (CCD1000-PB, Princeton Instruments) and were transferred to a computer workstation running MetaMorph imaging software (Universal Imaging, West Chester, PA). To monitor transport of the GFP-fusion proteins, cells were imaged using either a 60x or 100x lens (plan apochromat, NA 1.4, Nikon) and images were collected at 1.5-3 second intervals for 2-5 minutes. z-series stepping intervals were controlled through MetaMorph using a z-axis motor (model H128Z, Prior Scientific Instruments Ltd., Irvine CA). Unless otherwise noted, accumulated xy-planes in a z-series are displayed as a projection of all focal planes.

8.7.7. Time-lapse confocal microscopy

Confocal microscopy was performed on a Zeiss Axiovert 100 (Carl Zeiss, Oberkochen, Germany) using the LSM510 with a 63x objective. GFP, illuminated at 488nm (Argon laser), and DiIC¹⁶, illuminated at 543nm (HeNe laser) images were acquired simultaneously in Zeiss' "single-track mode". 200 frames were acquired for each time-lapse recording. The focal depth was set to 1.5µm to facilitate tracking of individual carriers, which moved in 3-dimensions within the cytoplasm. For sequential Z-axis time-series the bottom of the cells were imaged first. Time-lapse recordings were then made, at 1.5µm z-axis intervals, throughout the entire cell depth. Post-acquisition processing of confocal images was performed using MetaMorph.

8.8. Chapter 7: Insulin-regulated recycling

8.8.1. Cell lines and cell culture

The CHO cells expressing HA-GLUT4-GFP and either the human TR or the vpTR chimera have been described previously (Lampson et al., 2000). These cells are derived from TRVb CHO cells, which do not express any endogenous TR (McGraw et al., 1987). Cells were cultured in McCoy's 5A medium containing 5% fetal bovine serum, penicillin-streptomycin (Life Technologies, Inc., Gaithersburg, MD), 220 mM sodium bicarbonate, and 0.2 mg/ml G418 (Mediatech, Inc., Herndon, VA). Translocation of HA-GLUT4-GFP was demonstrated in the clonal lines, using the assay described previously (Lampson et al., 2000). Translocation was shown to be the same after uptake of the Cy3-labeled anti-HA antibody, using a similar assay with a Cy5-labeled anti-mouse antibody to measure surface levels of the anti-HA antibody. This result demonstrates that binding of the antibody does not alter the trafficking of HA-GLUT4-GFP. Expression of the TR and vpTR, measured by uptake of ^{125}I -Tf, was similar in the clonal lines used here.

8.8.2. Time-lapse dual-color TIR-FM

The dual-color TIR-FM system has been described above. For these experiments the 60 \times 1.45 NA objective was used. Images were acquired at ~3-4 frames/sec using full resolution of the CCD. The fluorescent signals from our probes were not bright enough for a higher rate. Because of this limited time resolution, we were unable to characterize fusion events as has been done previously (Chapter 3). In many cases vesicles appeared in the evanescent field and quickly disappeared. As endocytic vesicles may be smaller or less densely loaded with probes than post-Golgi carriers, we speculate that the diffusion of probes in the plasma membrane may be too fast for our time resolution. Consistent with this possibility, we found that resolution of many of the endocytic vesicles, but not of the post-Golgi carriers, was lost by 2 \times 2 binning of the images, which changes the pixel size from (112nm)² to (224nm)². We selected only

moving vesicles, assuming that these are transport intermediates, to analyze colocalization of the fluorescent probes. With single-color TIR-FM we were able to observe fusion of vesicles with the plasma membrane. Because of the increased signal intensity, time-lapse sequences were acquired at a rate of 6-10 frames/sec.

8.8.3. Labeling the ERC with Cy3-Tf

Cells were incubated for at least 1 hour at 37 °C with Cy3-Tf to label the TR or vpTR. To strip Tf from the surface, cells were incubated for 2 min with 0.2 M NaCl, 50 mM MES, pH 5.0 and washed with Hank's Balanced Salt Solution (HBSS) with 10 mM HEPES, pH 7.4. Removal of surface-bound Tf ensured that we did not image Tf-containing vesicles internalized from the plasma membrane. The cells were incubated in the same buffered HBSS at 32 °C for imaging. Some experiments were done at 37 °C with similar results. For experiments with insulin, cells were incubated with 170nM insulin.

8.8.4. Image analysis

First a local background was subtracted from each pixel, using the 20th percentile intensity in a 30×30 pixel area around that pixel. Vesicles moving either parallel or perpendicular to the membrane were selected manually, and the average pixel intensity of each probe was calculated over the vesicle area in a single image. To estimate the background intensity, spots of the same average size as the vesicles (5-10 pixels) were randomly placed throughout the image. Average red and green fluorescence was calculated for these spots. After removing obvious outliers (from cases in which the random spots overlapped with labeled structures), the 90th percentile from the population of random spots was used as a threshold for each color. Vesicles were classified as positive for red or green if the average fluorescence was above the threshold for that color. The same procedure was followed using the 85th or 95th percentile from the random spots for the threshold, with little change in the results, so the conclusions are not sensitive to this parameter.

9. List of Videos

All videos have corresponding figures. They are labeled identically to the figures. For example: *Video 5.2a non-pol p75* shows the fusion of p75-GFP carriers in non-polarized cells, similar to what is shown in *Fig. 5.2a non-polarized*. If not otherwise noted, the time-lapse sequences were acquired at ~5 frames/sec with a pixel size of (112nm)².

Video 3.3 : Post-Golgi carriers containing VSVG-GFP imaged in TIR-FM.

The sequence (30 frames/sec, pixel size 268nm) shows a part of the cell surface imaged in TIR-FM. The cell edge is on the upper left, the Golgi is on the lower right corner. As discussed in Chapter 3, three types of carriers can be seen: (1) stationary carriers, (2) carriers that move but do not fuse, and (3) carriers that fuse to the plasma membrane. Examples of fusing carriers can be seen at the extreme left and right of the field by a local burst and spread of the fluorescence signal. The carrier on the extreme left was imaged during its transport, docking and fusion phases. The carriers on the right did not move significantly before they fused.

Video 3.3b : Spherical post-Golgi carrier (VSVG-GFP) fusion.

This sequence (30 frames/sec, pixel size 268nm) shows a highly enlarged region containing a medium sized spherical carrier fusing to the plasma membrane. The fusion can be seen as a local increase and spread of the fluorescence signal.

Video 3.4a : Large tubular post-Golgi carrier (VSVG-GFP) fusion.

This sequence (10 frames/sec, pixel size 134nm) shows a long tubular carrier undergoing transport, docking and fusion. During transport, the intensity of the tubule changes slightly. Most likely, this is due to movement in and out of the evanescent field. Note that the tubule rounds up to a dot just at the onset of fusion. Fusion occurs with a huge burst of fluorescence followed by a spread of the fluorescence.

Videos 4.3b,e : Microtubule dynamics in TIR-FM.

NRK fibroblasts expressing (b) tau-GFP (2h post microinjection) or (e) GFP- β -tubulin (24h post microinjection) were imaged in TIR-FM (2 frames/sec, pixel size

112nm). The sequences show regions of the images in Fig. 4.3b (tau-GFP) and 4.3e (GFP- β -tubulin). Both videos show distinct microtubules undergoing phases of growth, shortening and pause, typically called dynamic instability. Also, there are microtubules that move sideways and bend. The MT movements seen with tau-GFP are very similar to the movements seen with GFP- β -tubulin.

Videos 4.5b,c : Transport, docking and fusion of post-Golgi carriers along microtubules imaged in simultaneous dual-color TIR-FM.

(b) NRK fibroblasts were microinjected with cDNA encoding p75-GFP and tau-GFP and imaged in TIR-FM. The sequence was processed according to the protocol for 'temporal' pseudo-color TIR-FM to separate the fast moving carriers (green) from the slow motion of the MTs (red). The transport of membrane cargo along the microtubules occurred in the typical saltatory fashion, alternating between fast and slow movements. The carriers frequently switched between different microtubule tracks in the dense microtubule meshwork. Some carriers reached the edge of the cell (see left margin at the end of the sequence). After stopping for various lengths of time on the microtubule tracks, the carriers appeared to fuse with the plasma membrane, as detected by an increase and spread of the fluorescence intensity. White arrows appear 5 frames before each fusion start to indicate the fusions. Note that, due to the 'temporal' pseudo-color processing, a green signal remains at the center of each fusion after dispersal of the cargo.

(c) Sparse MDCK cells were microinjected with cDNA encoding p75-YFP and tau-CFP and imaged in simultaneous dual-color TIR-FM. The sequence was processed as described (methods), including bleed-through correction and contrast enhancement. A tubular post-Golgi carrier loaded with p75-YFP (red) is seen to track along the continuous meshwork of microtubule tracks (green). It bends while switching tracks, moves back a small distance, until it collapses and fuses along the microtubule track.

Videos 4.6a,b : Collapse and Fusion of tubular post-Golgi carriers imaged in TIR-FM.

Sparsely plated MDCK cells were microinjected with cDNA encoding p75-GFP and imaged in TIR-FM after release of the Golgi block. The sequences show

collapse and fusion of a tubular carrier that (a) completely fuses in one single step or (b) fuses in two steps to the plasma membrane. Note, that the center of both fusions is not at one end of the tubular carrier, but rather close to the center of the tubule.

The long tubular carrier (b) enters the evanescent field with an upward movement while still apparently held on its bottom end. Its swaying movements suggest that it is partially attached to the cytoskeleton. At the onset of the first fusion the tubule undergoes an abrupt shortening and delivers a part of its cargo to the plasma membrane. This partial fusion and shortening is followed by a 3 - 4 sec stationary phase. Before the start of the second fusion, the center of the carrier fluorescence moves about 0.5 μ m. During the second fusion event, all remaining cargo is delivered to the plasma membrane.

Videos 4.7a,b,c : Transport, docking and fusion of post-Golgi carriers in stationary and migrating NRK fibroblasts.

NRK fibroblasts were microinjected with cDNA encoding LDLR-GFP and imaged in TIR-FM after the release of the Golgi block. The sequences show sub-regions of the cells. The fusions are indicated by white arrows that appear 10 frames before the fusion start.

(a) Untreated stationary cell: Post-Golgi carriers are seen to fuse in the periphery of the cell.

(b) Nocodazole-treated stationary cell: Typically, large highly fluorescent static spots are seen rather than small moving carriers (compare to videos 4.5a and c). These large spots are most likely Golgi mini-stacks in the evanescent field. They appear to partially fuse in multiple rounds with the plasma membrane. Some small carriers are seen to be transported over short distances. This movement could be due to nocodazole-resistant microtubules.

(c) Untreated migrating cell, leading edge: Many post-Golgi carriers are transported to the leading edge before they dock and fuse with the plasma membrane just a few micrometers before the cell edge.

(c) Untreated migrating cell, trailing end: Many post-Golgi carriers are seen close to the plasma membrane of the trailing end of the cell. However, only few

of them are detected to fuse.

Videos 5.2a,b,c : Movement and fusion of carriers at the basal membrane in MDCK cells.

Non-polarized (non-pol) and polarized (pol) MDCK cells were microinjected with cDNA encoding (a) p75-GFP, (b) LDLR-GFP and (c, only non-pol) NCAM-GFP. The basal membrane was monitored in TIR-FM after release of the 20°C Golgi block. Sequences show the movement and the fusion (white circles) of the post-Golgi carriers.

Videos 5.4a,b : Post-Golgi carriers are restricted within the apical cytoplasm.

The spatial distribution of post-Golgi carriers in polarized cells was determined using epi or confocal time-lapse imaging in sequential z-axis planes. The time-lapse series were taken from the cell “bottom” (left), “middle” (middle, z-position = 3-5 μm from bottom) and “top” (right, 7-10 μm from bottom) for (a) NCAM-GFP (0.7 frames/sec), and (b) p75-GFP (confocal, 2 frames/sec). The maximum readout rates of the CCD (epi) and the photomultiplier detectors (confocal) limited the speed of the acquisition.

Video 5.5 : Transport and fusion of a basolateral post-Golgi carrier with the lateral membrane in polarized MDCK cells.

Polarized MDCK expressing NCAM-GFP (green) were incubated with DiIC¹⁶ (red) to fluorescently label the plasma membrane. Transport and delivery of NCAM-GFP to the plasma membrane was monitored by time-lapse confocal microscopy (2 frames/sec). Fusion was defined as a transient color change from green to yellow. After delivery, the yellow color reconverts to red, marking the diffusion of NCAM-GFP throughout the lateral membrane.

Video 5.6b,c : Delivery of apical and basolateral post-Golgi carriers in nocodazole-treated, polarized MDCK cells.

The basal plasma membrane of nocodazole-treated polarized MDCK cells expressing either (b) LDLR-GFP or (c) p75-GFP was monitored by TIR-FM. White circles mark the fusion sites. Note that carriers containing only p75-GFP (c), but not LDLR-GFP (b), fused with the basal membrane. The black regions mark saturation of the CCD due to extreme brightness of static carriers.

Video 7.3a,c : Transferrin Receptor (TR) is segregated from GLUT4 in transport vesicles imaged in TIR-FM.

Cells expressing HA-GLUT4-GFP (green) and either vpTR (a) or the TR (c) were loaded with Cy3-Tf (red) and imaged by time-lapse TIR-FM (~4 frames/sec).

(a) Most of the GLUT4 vesicles (green) colocalize with the vpTR vesicles (red).

(c) Most of the GLUT4 vesicles (green) do NOT colocalize with the TR vesicles (red).

10. Summary

The last stage of the constitutive secretory pathway is the delivery and fusion of post-Golgi transport vesicles (carriers) to the plasma membrane. However, it is still unclear where at the plasma membrane these carriers fuse, in a living cell. In this work we used total internal reflection fluorescence microscopy (TIR-FM) to study the delivery and fusion of post-Golgi carriers, as well as of recycling vesicles from the endosomal compartment, to the cell surface in live cells. TIR-FM is suited to image fluorescent molecules near the cell-substrate interface, since it selectively illuminates the contact surface of cells.

One aim of this work was to establish a quantitative method for the microscopic detection of single exocytic fusion events. Following the localization of fusion we answered basic, previously unresolved, questions in the field of membrane traffic.

1. Imaging fusion of single post-Golgi carriers. A TIR-FM system was optimized to image exocytosis of single post-Golgi carriers. By labeling the carriers with a GFP-tagged membrane protein (vesicular stomatitis virus glycoprotein, VSVG), quantitative criteria for the microscopic detection of single carrier fusion events were established for the first time. Quantitative analysis of time-lapse images could clearly distinguish fusion of the carriers from both movement of carriers relative to the plasma membrane as well as lysis of carriers. The flattening of the carriers into the plasma membrane as well as the subsequent diffusion of the membrane cargo into the plasma membrane was resolved. The duration of the flattening process was found to depend on the size of the carrier, distinguishing small spherical from large tubular carriers.

2. Role of microtubules in post-Golgi traffic of fibroblasts. The simultaneous imaging of post-Golgi carriers and microtubules using a novel dual-color TIR-FM system showed that post-Golgi carriers are transported along microtubules to the fusion sites at the plasma membrane. The data strongly

suggested that the carriers are capable of undergoing fusion while still attached to the microtubules and that the carriers do not have to reach the end of the microtubules in order to fuse. In contrast to stationary fibroblasts, migrating fibroblasts were shown to have a microtubule-mediated mechanism for polarized insertion of post-Golgi carriers (here LDL-receptor-GFP) close to the leading edge. Disrupting the microtubules restricted this directed delivery of the carriers to regions of the plasma membrane close to the Golgi complex, making the distribution of fusion sites in stationary and migrating cells indistinguishable. Disrupting the microtubules also decreased the overall fusion frequency, increased the frequency of 'partial' fusions, and increased the amount of cargo delivered per fusion. We conclude that the microtubule cytoskeleton is necessary for the domain-specific delivery of post-Golgi membrane cargo in fibroblasts.

3. Role of microtubules in post-Golgi traffic of polarized epithelial cells.

Time-lapse fluorescence microscopy was used to analyze the delivery of apical and basolateral membrane proteins to the cell surface in both non-polarized and polarized epithelial cells. We demonstrated that post-Golgi carriers containing either apical or basolateral membrane proteins fuse to the basal membrane in non-polarized cells. Upon polarization, exocytosis of all carriers to the basal membrane was abrogated. Basolateral carriers were seen to fuse to sites at the lateral membrane, while apical carriers presumably fused to the apical membrane. This selective targeting is concomitant with redistribution of the t-SNAREs, syntaxin 3 and 4, upon polarization. Furthermore, we showed that both the targeted exocytosis of apical proteins and the exclusive localization of syntaxin 3 at the apical plasma membrane are dependent on intact microtubules in polarized epithelial cells. In contrast, targeted exocytosis of basolateral proteins and the basolateral distribution of syntaxin 4 and sec6 are maintained independently of microtubules in polarized cells.

4. Insulin-regulated recycling of glucose transporter. We studied the insulin-regulated release of the glucose transporter (GLUT4) from the endosomal

recycling compartment (ERC) in live cells. We show that GLUT4 is retained within the transferrin receptor-containing general ERC in fibroblasts. Using dual-color TIR-FM, we demonstrate that the transferrin receptor and GLUT4 are transported from the ERC in separate vesicles. This provides the first functional evidence for the formation of distinct classes of vesicles from the ERC. We propose that GLUT4 is dynamically retained within the ERC in fibroblasts because it is concentrated in vesicles that form more slowly than those that transport transferrin receptor.

11. Zusammenfassung

Der Transport von Post-Golgi-Vesikeln und deren Fusion mit der Plasmamembran sind die finalen Prozesse bei der konstitutiven Sekretion in lebenden Zellen. Der Transportweg zum Ort der Fusion dieser Vesikel mit der Plasmamembran wurde bisher nicht ausreichend untersucht. In der vorliegenden Arbeit wurde Totalreflexions-Fluoreszenzmikroskopie (TIR-FM) genutzt, um Transport und Fusion von Post-Golgi-Vesikeln, wie auch von Vesikeln des endosomalen "Recycling" Kompartiments, zu untersuchen. TIR-FM ist speziell dafür geeignet, fluoreszente Moleküle am Zell-Substrat-Übergang bildhaft darzustellen, weil die Kontaktfläche der Zelle selektiv angeregt wird.

Ein Ziel dieser Arbeit war es, eine quantitative Methode zur mikroskopischen Detektion einzelner Ereignisse bei der Exozytose zu etablieren. Aufbauend auf der Lokalisierung der Fusionen von Post-Golgi-Vesikeln wurden grundlegende offene Fragen auf dem Gebiet des Vesikeltransports beantwortet.

1. Mikroskopische Darstellung von Fusionsereignissen einzelner Post-Golgi-Transportvesikel. Ein TIR-FM-System wurde optimiert, um die Exozytose einzelner Post-Golgi-Vesikel zu detektieren. Indem die Vesikel mit einem Membranprotein (vesikuläre stomatische virale Glykoprotein, VSVG), gekoppelt an GFP, markiert wurden, konnten erstmalig quantitative Kriterien für die mikroskopische Detektion von einzelnen Fusionen etabliert werden. Durch quantitative Bildanalyse des zeitlichen Ablaufes konnten die Fusionen sowohl von der Bewegung relativ zur Plasmamembran als auch von der lichtinduzierten Lyse unterschieden werden. Der Einbau der Vesikelmembran in die Plasmamembran und die darauffolgende Diffusion der Membranproteine konnten zeitlich aufgelöst werden. Kleinere, sphärische und größere, tubuläre Vesikel wurden anhand der Dauer des vesikulären Einbauprozesses in die Plasmamembran unterschieden.

2. Funktion von Mikrotubuli im Post-Golgi-Vesikeltransport von Fibroblasten. Die gleichzeitige Beobachtung von Post-Golgi-Vesikeln und Mikrotubuli durch die Verwendung eines neuartigen Zweifarben-TIR-FM-Systems zeigte, daß die Vesikel an Mikrotubuli zum Ort ihrer Fusion transportiert werden. Dabei können die Vesikel noch zur Zeit der Fusion an die Mikrotubuli gebunden sein und müssen für die Fusion nicht notwendigerweise bis an das Ende der Mikrotubuli transportiert werden. Weiterhin zeigten unsere Ergebnisse, daß Exozytose von Vesikeln in wandernden Fibroblasten, im Gegensatz zu stationären Fibroblasten, bevorzugt in der Nähe des führenden Lamellipodiums ("leading edge") stattfindet. Nach Depolymerisierung der Mikrotubuli wurde dieser gerichtete Transport des Membranproteins (hier LDL-Rezeptor-GFP) unterbrochen und wandernde Fibroblasten konnten anhand der örtlichen Verteilung der Fusionen nicht mehr von stationären unterschieden werden. Die Depolymerisierung der Mikrotubuli führte außerdem zur Senkung der Fusionsfrequenz, zum Anstieg 'unvollständiger' Fusionen und zum Anstieg der Menge an Membranproteinen, die während einzelner Fusionen an die Plasmamembran abgegeben wurden. Wir schließen daraus, daß Mikrotubuli für den gerichteten Transport von Membranproteinen in Post-Golgi-Vesikeln in Fibroblasten notwendig sind.

3. Funktion von Mikrotubuli im Post-Golgi-Vesikeltransport von polarisierten Epithelialzellen. Mittels zeitaufgelöster Fluoreszenzmikroskopie haben wir den Transport von apikalen und basolateralen Membranproteinen zur Plasmamembran sowohl in unpolarisierten als auch in polarisierten Epithelialzellen untersucht. Unsere Resultate zeigten, daß in unpolarisierten Zellen sowohl apikale als auch basolaterale Post-Golgi-Vesikel an der basalen Zellmembran fusionieren. Nach Polarisation der Zellen fand die basale Exozytose beider Vesikel nicht mehr statt. Stattdessen fusionierten basolaterale Vesikel direkt zu Regionen an der lateralen Membran, während apikale Vesikel zur apikalen Plasmamembran transportiert wurden. Dieser selektive Transport fand nach der Polarisation der Zellen statt, parallel zur Umverteilung der t-

SNAREs (Syntaxin 3 und 4). Weitere Ergebnisse zeigten, daß die exklusive Lokalisierung von Syntaxin 3 und apikalen Membranproteinen intakte Mikrotubuli benötigt. Im Gegensatz dazu, ist die gerichtete Exozytose von basolateralen Membranproteinen und die Verteilung von Syntaxin 4 und sec6 in polarisierten Zellen unabhängig von dem Zustand der Mikrotubuli.

4. Insulinabhängiges “Recycling” des Glukosetransporters. Die insulinabhängige Freigabe des Glukosetransporters GLUT4 vom endosomalen “Recycling” Kompartiment (ERC für “endosomal recycling compartment”) wurde untersucht. Die Ergebnisse zeigten, daß GLUT4 in Fibroblasten dynamisch in dem generellen ERC zurückgehalten wird, das auch den Transferrin-Rezeptor enthält. Mittels Zweifarben-TIR-FM demonstrieren wir, daß der Transferrin-Rezeptor und GLUT4 in separaten Vesikeln vom ERC zur Plasmamembran transportiert werden. Damit wurde der erste funktionellen Beweis für die Formation separater Vesikel vom ERC geliefert. Der langsame, insulinabhängige Transport der GLUT4-Vesikel kann dadurch erklärt werden, dass GLUT4 in Vesikel konzentriert wird, die sich langsamer bilden als Vesikel, die den Transferrin-Rezeptor beinhalten.

12. Reference List

- Achler,C., Filmer,D., Merte,C., and Drenckhahn,D. (1989). Role of microtubules in polarized delivery of apical membrane proteins to the brush border of the intestinal epithelium. *J. Cell Biol.* *109*, 179-189.
- Albillos,A., Dernick,G., Horstmann,H., Almers,W., De Toledo,G.A., and Lindau,M. (1997). The exocytotic event in chromaffin cells revealed by patch amperometry. *Nature* *389*, 509-512.
- Ales,E., Tabares,L., Poyato,J.M., Valero,V., Lindau,M., and Alvarez,d.T. (1999). High calcium concentrations shift the mode of exocytosis to the kiss- and-run mechanism. *Nat. Cell Biol.* *1*, 40-44.
- Alvarez de Toledo,G., Fernández-Chacón,R., and Fernández,J.M. (1993). Release of secretory products during transient vesicle fusion. *Nature* *363*, 554-558.
- Aniento,F., Gu,F., Parton,R.G., and Gruenberg,J. (1996). An endosomal β COP is involved in the pH-dependent formation of transport vesicles destined for late endosomes. *J. Cell Biol.* *133*, 29-41.
- Artalejo,C.R., Elhamdani,A., and Palfrey,H.C. (1998). Secretion: dense-core vesicles can kiss-and-run too. *Curr. Biol.* *8*, R62-R65.
- Axelrod,D. (1981). Cell-substrate contacts illuminated by total internal reflection fluorescence. *J. Cell Biol.* *89*, 141-145.
- Axelrod,D. (1989). Total internal reflection fluorescence microscopy. *Methods Cell Biol.* *30*, 245-270.
- Axelrod,D. (2001). Selective imaging of surface fluorescence with very high aperture microscope objectives. *J. Biomed. Opt.* *6*, 6-13.
- Axelrod,D. and Wang,M.D. (1994). Reduction-of-dimensionality kinetics at reaction-limited cell surface receptors. *Biophys. J.* *66*, 588-600.
- Bacallao,R., Antony,C., Dotti,C., Karsenti,E., Stelzer,E.H.K., and Simons,K. (1989). The subcellular organization of Madin-Darby canine kidney cells during the formation of a polarized epithelium. *J. Cell Biol.* *109*, 2817-2832.
- Bajno,L., Peng,X.R., Schreiber,A.D., Moore,H.P., Trimble,W.S., and Grinstein,S. (2000). Focal exocytosis of VAMP3-containing vesicles at sites of phagosome formation. *J. Cell Biol.* *149*, 697-706.
- Bergmann,J.E., Kupfer,A., and Singer,S.J. (1983). Membrane insertion at the leading edge of motile fibroblasts. *Proc. Natl. Acad. Sci. U. S. A.* *80*, 1367-1371.
- Bershady,A.D., Vaisberg,E.A., and Vasiliev,J.M. (1991). Pseudopodial activity at the active edge of migrating fibroblast is decreased after drug-induced microtubule depolymerization. *Cell Motil. Cytoskeleton* *19*, 152-158.
- Bi,G.Q., Morris,R.L., Liao,G., Alderton,J.M., Scholey,J.M., and Steinhardt,R.A. (1997). Kinesin- and myosin-driven steps of vesicle recruitment for Ca^{2+} - regulated exocytosis. *J. Cell Biol.* *138*,

999-1008.

Bilder,D., Li,M., and Perrimon,N. (2000). Cooperative regulation of cell polarity and growth by *Drosophila* tumor suppressors. *Science* 289, 113-116.

Bilder,D. and Perrimon,N. (2000). Localization of apical epithelial determinants by the basolateral PDZ protein Scribble. *Nature* 403, 676-680.

Bloom,G.S. and Goldstein,L.S. (1998). Cruising along microtubule highways: how membranes move through the secretory pathway. *J. Cell Biol.* 140, 1277-1280.

Boll,W., Partin,J.S., Katz,A.I., Caplan,M.J., and Jamieson,J.D. (1991). Distinct pathways for basolateral targeting of membrane and secretory proteins in polarized epithelial cells. *Proc. Natl. Acad. Sci. USA* 88, 8592-8596.

Bonifacino,J.S. and Dell'Angelica,E.C. (1999). Molecular bases for the recognition of tyrosine-based sorting signals. *J Cell Biol* 145, 923-6.

Bradbury,N.A. and Bridges,R.J. (1994). Role of membrane trafficking in plasma membrane solute transport. *Am. J. Physiol* 267, C1-24.

Breckenridge,L.J. and Almers,W. (1987). Currents through the fusion pore that forms during exocytosis of a secretory vesicle. *Nature* 328, 814-817.

Breitfeld,P.P., McKinnon,W.C., and Mostov,K.E. (1990). Effect of nocodazole on vesicular traffic to the apical and basolateral surfaces of polarized MDCK cells. *J. Cell Biol.* 111, 2365-2373.

Bretscher,M.S. (1996). Getting membrane flow and the cytoskeleton to cooperate in moving cells. *Cell* 87, 601-606.

Brown,S.S. (1999). Cooperation between microtubule- and actin-based motor proteins. *Annu. Rev. Cell Dev. Biol.* 15, 63-80.

Cannon,C., van Adelsberg,J., Kelly,S., and Al-Awqati,Q. (1985). Carbon-dioxide-induced exocytotic insertion of H⁺ pumps in turtle-bladder luminal membrane: role of cell pH and calcium. *Nature* 314, 443-446.

Chen,Y.A. and Scheller,R.H. (2001). SNARE-mediated membrane fusion. *Nat. Rev. Mol. Cell Biol.* 2, 98-106.

Chow,R.H., Klingauf,J., and Neher,E. (1994). Time course of Ca²⁺ concentration triggering exocytosis in neuroendocrine cells. *Proc. Natl. Acad. Sci. U. S. A* 91, 12765-12769.

Chuang,J.Z. and Sung,C.H. (1998). The cytoplasmic tail of rhodopsin acts as a novel apical sorting signal in polarized MDCK cells. *J Cell Biol.* 142, 1245-1256.

Cole,N.B., Sciaky,N., Marotta,A., Song,J., and Lippincott-Schwartz,J. (1996). Golgi dispersal during microtubule disruption: regeneration of Golgi stacks at peripheral endoplasmic reticulum exit sites. *Mol. Biol. Cell* 7, 631-650.

Cramer,L.P. and Mitchison,T.J. (1995). Myosin is involved in postmitotic cell spreading. *J. Cell Biol.* 131, 179-189.

Crank,J. (1995). *The Mathematics of Diffusion.* Oxford University Press).

- Czech, M.P. (1995). Molecular actions of insulin on glucose transport. *Annu Rev Nutr* 15, 441-71.
- de Almeida, J.B. and Stow, J.L. (1991). Disruption of microtubules alters polarity of basement membrane proteoglycan secretion in epithelial cells. *Am J Physiol* 261, C691-C700.
- Del Castillo, J. and Katz, B. (1954). Quantal components of the end-plate potential. *Journal of Physiology* 124, 560-573.
- Dell'Angelica, E.C., Klumperman, J., Stoorvogel, W., and Bonifacino, J.S. (1998). Association of the AP-3 adaptor complex with clathrin. *Science* 280, 431-4.
- Eilers, U., Klumperman, J., and Hauri, H.P. (1989). Nocodazole, a microtubule-active drug, interferes with apical protein delivery in cultured intestinal epithelial cells (Caco-2). *J Cell Biol.* 108, 13-22.
- Fatt, P. and Katz, B. (1952). Spontaneous subthreshold activity at motor nerve endings. *J. Physiol (Lond)* 117, 109-128.
- Fernandez, J.M., Neher, E., and Gomperts, B.D. (1984). Capacitance measurements reveal stepwise fusion events in degranulating mast cells. *Nature* 312, 453-455.
- Ferro-Novick, S. and Jahn, R. (1994). Vesicle fusion from yeast to man. *Nature* 370, 191-193.
- Fesce, R. and Meldolesi, J. (1999). Peeping at the vesicle kiss. *Nat. Cell Biol.* 1, E3-E4.
- Foletti, D.L., Lin, R., Finley, M.A., and Scheller, R.H. (2000). Phosphorylated syntaxin 1 is localized to discrete domains along a subset of axons. *J Neurosci.* 20, 4535-4544.
- Forte, J.G. and Yao, X. (1996). The membrane-recruitment-and-recycling hypothesis of gastric HCl secretion. *Trends Cell Biol* 6, 45-48.
- Fukuda, R., McNew, J.A., Weber, T., Parlati, F., Engel, T., Nickel, W., Rothman, J.E., and Sollner, T.H. (2000). Functional architecture of an intracellular membrane t-SNARE. *Nature* 407, 198-202.
- Funatsu, T., Harada, Y., Tokunaga, M., Saito, K., and Yanagida, T. (1995). Imaging of single fluorescent molecules and individual ATP turnovers by single myosin molecules in aqueous solution. *Nature* 374, 555-559.
- Futter, C.E., Gibson, A., Allchin, E.H., Maxwell, S., Ruddock, L.J., Odorizzi, G., Domingo, D., Trowbridge, I.S., and Hopkins, C.R. (1998). In polarized MDCK cells basolateral vesicles arise from clathrin-gamma-adaptin-coated domains on endosomal tubules. *J. Cell Biol.* 141, 611-623.
- Garcia, E.P., McPherson, P.S., Chilcote, T.J., Takei, K., and De Camilli, P. (1995). rbSec1A and B colocalize with syntaxin 1 and SNAP-25 throughout the axon, but are not in a stable complex with syntaxin. *J Cell Biol.* 129, 105-120.
- Garza, L. and Birnbaum, M. (2000). Insulin-responsive aminopeptidase trafficking in 3T3-L1 adipocytes. *J. Biol. Chem.* 275, 2560-2567.
- Gerdes, H.H. and Kaether, C. (1996). Green fluorescent protein: applications in cell biology. *FEBS Lett.* 389, 44-47.
- Ghosh, R.N., Mallet, W.G., Soe, T.T., McGraw, T.E., and Maxfield, F.R. (1998). An endocytosed TGN38 chimeric protein is delivered to the TGN after trafficking through the endocytic recycling compartment in CHO cells. *J. Cell Biol.* 142, 923-36.

Gibson,A., Futter,C.E., Maxwell,S., Allchin,E.H., Shipman,M., Kraehenbuhl,J.P., Domingo,D., Odorizzi,G., Trowbridge,I.S., and Hopkins,C.R. (1998). Sorting mechanisms regulating membrane protein traffic in the apical transcytotic pathway of polarized MDCK cells. *J Cell Biol* 143, 81-94.

Gilbert,T., Le Bivic,A., Quaroni,A., and Rodriguez-Boulan,E. (1991). Microtubular organization and its involvement in the biogenetic pathways of plasma membrane proteins in Caco-2 intestinal epithelial cells. *J. Cell Biol.* 113, 275-288.

Gillis,K.D., Pun,R.Y., and Mislis,S. (1991). Single cell assay of exocytosis from adrenal chromaffin cells using "perforated patch recording". *Pflugers Arch.* 418, 611-613.

Gingell,D. (1981). The interpretation of interference-reflection images of spread cells: significant contributions from thin peripheral cytoplasm. *J Cell Sci.* 49, 237-247.

Gingell,D. and Todd,I. (1979). Interference reflection microscopy. A quantitative theory for image interpretation and its application to cell-substratum separation measurement. *Biophys. J* 26, 507-526.

Goulian,M. and Simon,S.M. (2000). Tracking single proteins within cells. *Biophys. J.* 79, 2188-2198.

Grindstaff,K.K., Bacallao,R.L., and Nelson,W.J. (1998a). Apiconuclear organization of microtubules does not specify protein delivery from the trans-Golgi network to different membrane domains in polarized epithelial cells. *Mol. Biol. Cell* 9, 685-699.

Grindstaff,K.K., Yeaman,C., Anandasabapathy,N., Hsu,S.C., Rodriguez-Boulan,E., Scheller,R.H., and Nelson,W.J. (1998b). Sec6/8 complex is recruited to cell-cell contacts and specifies transport vesicle delivery to the basal-lateral membrane in epithelial cells. *Cell* 93, 731-740.

Hazuka,C.D., Foletti,D.L., Hsu,S.C., Kee,Y., Hopf,F.W., and Scheller,R.H. (1999). The sec6/8 complex is located at neurite outgrowth and axonal synapse- assembly domains. *J Neurosci.* 19, 1324-1334.

Hinshaw,J.E. (2000). DYNAMIN AND ITS ROLE IN MEMBRANE FISSION. *Annu. Rev. Cell Dev. Biol.* 16, 483-519.

Hirschberg,K., Miller,C.M., Ellenberg,J., Presley,J.F., Siggia,E.D., Phair,R.D., and Lippincott-Schwartz,J. (1998). Kinetic analysis of secretory protein traffic and characterization of golgi to plasma membrane transport intermediates in living cells. *J. Cell Biol.* 143, 1485-1503.

Hirschfeld,T. (1965). Total Reflection Fluorescence. *Canadian Journal of Spectroscopy* 10, 128.

Hsu,S.C., Ting,A.E., Hazuka,C.D., Davanger,S., Kenny,J.W., Kee,Y., and Scheller,R.H. (1996). The mammalian brain rsec6/8 complex. *Neuron* 17, 1209-1219.

Hugon,J.S., Bennett,G., Pothier,P., and Ngoma,Z. (1987). Loss of microtubules and alteration of glycoprotein migration in organ cultures of mouse intestine exposed to nocodazole or colchicine. *Cell Tissue Res.* 248, 653-662.

Humeau,Y., Doussau,F., Vitiello,F., Greengard,P., Benfenati,F., and Poulain,B. (2001). Synapsin controls both reserve and releasable synaptic vesicle pools during neuronal activity and short-term plasticity in Aplysia. *J. Neurosci.* 21, 4195-4206.

Hunt,J.M., Bommert,K., Charlton,M.P., Kistner,A., Habermann,E., Augustine,G.J., and Betz,H.

- (1994). A post-docking role for synaptobrevin in synaptic vesicle fusion. *Neuron* 12, 1269-1279.
- Ikonen,E. and Simons,K. (1998). Protein and lipid sorting from the trans-Golgi network to the plasma membrane in polarized cells. *Semin Cell Dev Biol* 9, 503-9.
- Inouye,S. and Spring,K.R. (1997). *Video Microscopy : The Fundamentals*. (New York: Plenum), pp. 1-764.
- Ishijima,A. and Yanagida,T. (2001). Single molecule nanobioscience. *Trends Biochem. Sci.* 26, 438-444.
- Jacob,R. and Naim,H.Y. (2001). Apical membrane proteins are transported in distinct vesicular carriers. *Curr. Biol.* 11, 1444-1450.
- Jahn,R. and Sudhof,T.C. (1999). Membrane fusion and exocytosis. *Annu. Rev. Biochem.* 68, 863-911.
- Jhun,B.H., Rampal,A.L., Liu,H., Lachaal,M., and Jung,C.Y. (1992). Effects of insulin on steady state kinetics of GLUT4 subcellular distribution in rat adipocytes. Evidence of constitutive GLUT4 recycling. *J Biol Chem* 267, 17710-5.
- Johnson,A.O., Lampson,M.A., and McGraw,T.E. (2001). A Di-Leucine Sequence and a Cluster of Acidic Amino Acids Are Required for Dynamic Retention in the Endosomal Recycling Compartment of Fibroblasts. *Mol Biol Cell* 12, 367-381.
- Johnson,A.O., Subtil,A., Petrush,R., Kobylarz,K., Keller,S.R., and McGraw,T.E. (1998). Identification of an insulin-responsive, slow endocytic recycling mechanism in Chinese hamster ovary cells. *J Biol Chem* 273, 17968-77.
- Kaether,C. and Gerdes,H.H. (1995). Visualization of protein transport along the secretory pathway using green fluorescent protein. *FEBS Letters* 369, 267-271.
- Kanai,F., Nishioka,Y., Hayashi,H., Kamohara,S., Todaka,M., and Ebina,Y. (1993). Direct demonstration of insulin-induced GLUT4 translocation to the surface of intact cells by insertion of a c-myc epitope into an exofacial GLUT4 domain. *J Biol Chem* 268, 14523-6.
- Kandror,K.V. and Pilch,P.F. (1994). gp160, a tissue-specific marker for insulin-activated glucose transport. *Proc Natl Acad Sci U S A* 91, 8017-21.
- Keller,P. and Simons,K. (1997). Post-Golgi biosynthetic trafficking. *J. Cell Sci.* 110, 3001-3009.
- Keller,P., Toomre,D., Diaz,E., White,J., and Simons,K. (2001). Multicolour imaging of post-Golgi sorting and trafficking in live cells. *Nat. Cell Biol.* 3, 140-149.
- Keller,S.R., Scott,H.M., Mastick,C.C., Aebersold,R., and Lienhard,G.E. (1995). Cloning and characterization of a novel insulin-regulated membrane aminopeptidase from Glut4 vesicles [published erratum appears in *J Biol Chem* 1995 Dec 15; 270(50):30236]. *J Biol Chem* 270, 23612-8.
- Kirchhausen,T., Bonifacino,J.S., and Riezman,H. (1997). Linking cargo to vesicle formation: receptor tail interactions with coat proteins. *Curr Opin Cell Biol* 9, 488-95.
- Knepper,M.A. and Inoue,T. (1997). Regulation of aquaporin-2 water channel trafficking by vasopressin. *Curr. Opin. Cell Biol.* 9, 560-564.

Kreitzer,G., Marmorstein,A., Okamoto,P., Vallee,R., and Rodriguez-Boulan,E. (2000). Kinesin and dynamin are required for post-Golgi transport of a plasma- membrane protein. *Nat. Cell Biol.* 2, 125-127.

Lafont,F., Burkhardt,J.K., and Simons,K. (1994). Involvement of microtubule motors in basolateral and apical transport in kidney cells. *Nature* 372, 801-803.

Lafont,F., Verkade,P., Galli,T., Wimmer,C., Louvard,D., and Simons,K. (1999). Raft association of SNAP receptors acting in apical trafficking in Madin-Darby canine kidney cells. *Proc. Natl. Acad. Sci. U. S. A* 96, 3734-3738.

Lampson,M.A., Racz,A., Cushman,S.W., and McGraw,T.E. (2000). Demonstration of insulin-responsive trafficking of GLUT4 and vpTR in fibroblasts. [Record Supplied By Publisher]. *J Cell Sci* 113, 4065-4076.

Lampson,M.A., Schmoranzer,J., Zeigerer,A., Simon,S.M., and McGraw,T.E. (2001). Insulin-regulated Release from the Endosomal Recycling Compartment Is Regulated by Budding of Specialized Vesicles. *Mol. Biol. Cell* 12, 3489-3501.

Lang,T., Bruns,D., Wenzel,D., Riedel,D., Holroyd,P., Thiele,C., and Jahn,R. (2001). SNAREs are concentrated in cholesterol-dependent clusters that define docking and fusion sites for exocytosis. *Embo J* 20, 2202-2213.

Lang,T., Wacker,I., Steyer,J., Kaether,C., Wunderlich,I., Soldati,T., Gerdes,H.H., and Almers,W. (1997). Ca²⁺-triggered peptide secretion in single cells imaged with green fluorescent protein and evanescent-wave microscopy. *Neuron* 18, 857-863.

Lang,T., Wacker,I., Wunderlich,I., Rohrbach,A., Giese,G., Soldati,T., and Almers,W. (2000). Role of actin cortex in the subplasmalemmal transport of secretory granules in PC-12 cells. *Biophys. J.* 78, 2863-2877.

Lawson,M.A. and Maxfield,F.R. (1995). Ca²⁺- and calcineurin-dependent recycling of an integrin to the front of migrating neutrophils. *Nature* 377, 75-79.

Le Borgne,R., Griffiths,G., and Hoflack,B. (1996). Mannose 6-phosphate receptors and ADP-ribosylation factors cooperate for high affinity interaction of the AP-1 Golgi assembly proteins with membranes. *J Biol Chem* 271, 2162-70.

Le Gall,A.H., Yeaman,C., Muesch,A., and Rodriguez-Boulan,E. (1995). Epithelial cell polarity: new perspectives. *Semin. Nephrol.* 15, 272-284.

Liao,G. and Gundersen,G.G. (1998). Kinesin is a candidate for cross-bridging microtubules and intermediate filaments. Selective binding of kinesin to detyrosinated tubulin and vimentin. *J Biol. Chem.* 273, 9797-9803.

Lippincott-Schwartz,J. (2001). The secretory membrane system studied in real-time. *Histochem. Cell Biol.* 116, 97-107.

Lippincott-Schwartz,J., Roberts,T.H., and Hirschberg,K. (2000). Secretory protein trafficking and organelle dynamics in living cells. *Annu. Rev. Cell Dev. Biol.* 16, 557-589.

Lipschutz,J.H., Guo,W., O'Brien,L.E., Nguyen,Y.H., Novick,P., and Mostov,K.E. (2000). Exocyst is involved in cystogenesis and tubulogenesis and acts by modulating synthesis and delivery of basolateral plasma membrane and secretory proteins. *Mol. Biol. Cell* 11, 4259-4275.

- Lock,S.O. and Friend,J.V. (1986). Phototoxicity testing in vitro: evaluation of mammalian cell culture techniques. *Food Chem. Toxicol.* **24**, 789-793.
- Low,S.H., Chapin,S.J., Weimbs,T., Komuves,L.G., Bennett,M.K., and Mostov,K.E. (1996). Differential localization of syntaxin isoforms in polarized Madin-Darby canine kidney cells. *Mol. Biol. Cell* **7**, 2007-2018.
- Low,S.H., Chapin,S.J., Wimmer,C., Whiteheart,S.W., Komuves,L.G., Mostov,K.E., and Weimbs,T. (1998). The SNARE machinery is involved in apical plasma membrane trafficking in MDCK cells. *J. Cell Biol.* **141**, 1503-1513.
- Lowe,M. (2000). Membrane transport: tethers and TRAPPs. *Curr. Biol.* **10**, R407-R409.
- Malide,D., St-Denis,J.F., Keller,S.R., and Cushman,S.W. (1997). Vp165 and GLUT4 share similar vesicle pools along their trafficking pathways in rat adipose cells. *FEBS Lett* **409**, 461-8.
- Markosyan,R.M., Melikyan,G.B., and Cohen,F.S. (1999). Tension of membranes expressing the hemagglutinin of influenza virus inhibits fusion. *Biophys. J.* **77**, 943-952.
- Martin,S., Rice,J.E., Gould,G.W., Keller,S.R., Slot,J.W., and James,D.E. (1997). The glucose transporter GLUT4 and the aminopeptidase vp165 colocalise in tubulo-vesicular elements in adipocytes and cardiomyocytes. *J Cell Sci* **110**, 2281-91.
- Matter,K., Bucher,K., and Hauri,H.-P. (1990). Microtubule perturbation retards both the direct and the indirect apical pathway but does not affect sorting of plasma membrane proteins in intestinal epithelial cells (Caco-2). *EMBO Journal* **9**, 3163-3170.
- Mayor,S., Presley,J.F., and Maxfield,F.R. (1993). Sorting of membrane components from endosomes and subsequent recycling to the cell surface occurs by a bulk flow process. *J Cell Biol* **121**, 1257-69.
- McGraw,T.E., Greenfield,L., and Maxfield,F.R. (1987). Functional expression of the human transferrin receptor cDNA in Chinese hamster ovary cells deficient in endogenous transferrin receptor. *J Cell Biol* **105**, 207-14.
- McNew,J.A., Parlati,F., Fukuda,R., Johnston,R.J., Paz,K., Paumet,F., Sollner,T.H., and Rothman,J.E. (2000). Compartmental specificity of cellular membrane fusion encoded in SNARE proteins. *Nature* **407**, 153-159.
- Meldolesi,J. (1998). Regulated exocytosis in neurons and neurosecretory cells: structural events and expression competence. *J. Physiol Paris* **92**, 119-121.
- Mellman,I. (2000). Quo Vadis: Polarized Membrane Recycling in Motility and Phagocytosis. *J. Cell Biol.* **149**, 529-530.
- Mitchison,T. and Kirschner,M. (1984). Dynamic instability of microtubule growth. *Nature* **312**, 237-242.
- Monck,J.R., Alvarez,d.T., and Fernandez,J.M. (1990). Tension in secretory granule membranes causes extensive membrane transfer through the exocytotic fusion pore. *Proc. Natl. Acad. Sci. U. S. A.* **87**, 7804-7808.
- Morris,C.E. and Homann,U. (2001). Cell surface area regulation and membrane tension. *J. Membrane Biol.* **179**, 79-102.

- Murthy,V.N. (1999). Optical detection of synaptic vesicle exocytosis and endocytosis. *Curr. Opin. Neurobiol.* 9, 314-320.
- Musch,A., Cohen,D., and Rodriguez-Boulan,E. (1997). Myosin II is involved in the production of constitutive transport vesicles from the TGN. *J. Cell Biol.* 138, 291-306.
- Musch,A., Xu,H., Shields,D., and Rodriguez-Boulan,E. (1996). Transport of vesicular stomatitis virus G protein to the cell surface is signal mediated in polarized and nonpolarized cells. *J Cell Biol* 133, 543-58.
- Nagasaki,T., Chapin,C.J., and Gundersen,G.G. (1992). Distribution of detyrosinated microtubules in motile NRK fibroblasts is rapidly altered upon cell-cell contact: implications for contact inhibition of locomotion. *Cell Motil. Cytoskeleton* 23, 45-60.
- Nakagawa,T., Setou,M., Seog,D., Ogasawara,K., Dohmae,N., Takio,K., and Hirokawa,N. (2000). A novel motor, KIF13A, transports mannose-6-phosphate receptor to plasma membrane through direct interaction with AP-1 complex. *Cell* 103, 569-581.
- Neher,E. and Marty,A. (1982). Discrete changes of cell membrane capacitance observed under conditions of enhanced secretion in bovine adrenal chromaffin cells. *Proc. Natl. Acad. Sci. U. S. A.* 79, 6712-6716.
- Noda,Y., Okada,Y., Saito,N., Setou,M., Xu,Y., Zhang,Z., and Hirokawa,N. (2001). KIFC3, a microtubule minus end-directed motor for the apical transport of annexin XIIIb-associated Triton-insoluble membranes. *J Cell Biol.* 155, 77-88.
- Nusse,O. and Lindau,M. (1988). The dynamics of exocytosis in human neutrophils. *J. Cell Biol.* 107, 2117-2123.
- Oheim,M., Loerke,D., Stühmer,W., and Chow,R.H. (1998). The last few milliseconds in the life of a secretory granule - Docking, dynamics and fusion visualized by total internal reflection fluorescence microscopy (TIRFM). *Eur. Biophys. J. Biophys. Lett.* 27, 83-98.
- Ohno,H., Aguilar,R.C., Yeh,D., Taura,D., Saito,T., and Bonifacino,J.S. (1998). The medium subunits of adaptor complexes recognize distinct but overlapping sets of tyrosine-based sorting signals. *J Biol Chem* 273, 25915-21.
- Omann,G.M. and Axelrod,D. (1996). Membrane-proximal calcium transients in stimulated neutrophils detected by total internal reflection fluorescence. *Biophys. J.* 71, 2885-2891.
- Orzech,E., Cohen,S., Weiss,A., and Aroeti,B. (2000). Interactions between the exocytic and endocytic pathways in polarized Madin-Darby canine kidney cells. *J Biol Chem* 275, 15207-19.
- Palade,G.E. (1975). Intracellular aspects of the process of protein secretion. *Science* 189, 347-358.
- Palazzo,A.F., Joseph,H.L., Chen,Y., Dujardin,D.L., Alberts,A.S., Pfister,K.K., Vallee,R.B., and Gundersen,G.G. (2001). Cdc42, dynein, and dynactin regulate MTOC reorientation independent of Rho-regulated microtubule stabilization. *Curr. Biol.* 11, 1536-1541.
- Palfrey,H.C. and Artalejo,C.R. (1998). Vesicle recycling revisited: rapid endocytosis may be the first step. *Neuroscience* 83, 969-989.
- Parlati,F., McNew,J.A., Fukuda,R., Miller,R., Sollner,T.H., and Rothman,J.E. (2000). Topological restriction of SNARE-dependent membrane fusion. *Nature* 407, 194-198.

- Pelham,H.R. (2001). SNAREs and the specificity of membrane fusion. *Trends Cell Biol.* 11, 99-101.
- Pessin,J.E., Thurmond,D.C., Elmendorf,J.S., Coker,K.J., and Okada,S. (1999). Molecular basis of insulin-stimulated GLUT4 vesicle trafficking. *Location! Location! Location! J. Biol. Chem.* 274, 2593-2596.
- Polishchuk,R.S., Polishchuk,E.V., Marra,P., Alberti,S., Buccione,R., Luini,A., and ironov,A.A. (2000). Correlative light-electron microscopy reveals the tubular-saccular ultrastructure of carriers operating between Golgi apparatus and plasma membrane. *J. Cell Biol.* 148, 45-58.
- Prasher,D.C., Eckenrode,V.K., Ward,W.W., Prendergast,F.G., and Cormier,M.J. (1992). Primary structure of the *Aequorea victoria* green-fluorescent protein. *Gene* 111, 229-233.
- Presley,J.F., Cole,N.B., Schroer,T.A., Hirschberg,K., Zaal,K.J., and Lippincott-Schwartz,J. (1997). ER-to-Golgi transport visualized in living cells. *Nature* 389, 81-85.
- Rea,S. and James,D.E. (1997). Moving GLUT4: the biogenesis and trafficking of GLUT4 storage vesicles. *Diabetes* 46, 1667-1677.
- Rindler,M.J., Ivanov,I.E., and Sabatini,D.D. (1987). Microtubule-acting drugs lead to the nonpolarized delivery of the influenza hemagglutinin to the cell surface of polarized Madin-Darby canine kidney cells. *J. Cell Biol.* 104, 231-241.
- Rodionov,V.I., Gyoeva,F.K., Tanaka,E., Bershadsky,A.D., Vasiliev,J.M., and Gelfand,V.I. (1993). Microtubule-dependent control of cell shape and pseudopodial activity is inhibited by the antibody to kinesin motor domain. *J. Cell Biol.* 123, 1811-1820.
- Rodionov,V.I., Hope,A.J., Svitkina,T.M., and Borisy,G.G. (1998). Functional coordination of microtubule-based and actin-based motility in melanophores. *Curr. Biol.* 8, 165-168.
- Rodriguez-Boulan,E. and Gonzalez,A. (1999). Glycans in post-Golgi apical targeting: sorting signals or structural props? *Trends Cell Biol.* 9, 291-294.
- Rodriguez-Boulan,E. and Nelson,W.J. (1989). Morphogenesis of the polarized epithelial cell phenotype. *Science* 245, 718-725.
- Rogalski,A.A. and Singer,S.J. (1984). Associations of elements of the Golgi apparatus with microtubules. *J. Cell Biol.* 99, 1092-1100.
- Rogers,S.L. and Gelfand,V.I. (1998). Myosin cooperates with microtubule motors during organelle transport in melanophores. *Curr. Biol.* 8, 161-164.
- Ross,S.A., Scott,H.M., Morris,N.J., Leung,W.Y., Mao,F., Lienhard,G.E., and Keller,S.R. (1996). Characterization of the insulin-regulated membrane aminopeptidase in 3T3-L1 adipocytes. *J Biol Chem* 271, 3328-32.
- Rothman,J.E. (1994). Intracellular membrane fusion. *Adv. Second Messenger Phosphoprotein Res.* 29, 81-96.
- Rothman,J.E. and Wieland,F.T. (1996). Protein sorting by transport vesicles. *Science* 272, 227-234.
- Rudolf,R., Salm,T., Rustom,A., and Gerdes,H.H. (2001). Dynamics of immature secretory granules: role of cytoskeletal elements during transport, cortical restriction, and F-actin-

dependent tethering. *Mol. Biol. Cell* 12, 1353-1365.

Rusan,N.M., Fagerstrom,C.J., Yvon,A.M., and Wadsworth,P. (2001). Cell cycle-dependent changes in microtubule dynamics in living cells expressing green fluorescent protein-alpha tubulin. *Mol. Biol. Cell* 12, 971-980.

Ryan,T.A. (1999). Inhibitors of myosin light chain kinase block synaptic vesicle pool mobilization during action potential firing. *J. Neurosci.* 19, 1317-1323.

Ryan,T.A., Reuter,H., and Smith,S.J. (1997). Optical detection of a quantal presynaptic membrane turnover. *Nature* 388, 478-482.

Sako,Y., Minoghchi,S., and Yanagida,T. (2000). Single-molecule imaging of EGFR signalling on the surface of living cells. *Nat. Cell Biol.* 2, 168-172.

Sammak,P.J. and Borisy,G.G. (1988). Direct observation of microtubule dynamics in living cells. *Nature* 332, 724-726.

Satoh,S., Nishimura,H., Clark,A.E., Kozka,I.J., Vannucci,S.J., Simpson,I.A., Quon,M.J., Cushman,S.W., and Holman,G.D. (1993). Use of bismannose photolabel to elucidate insulin-regulated GLUT4 subcellular trafficking kinetics in rat adipose cells. Evidence that exocytosis is a critical site of hormone action. *J Biol Chem* 268, 17820-9.

Saunders,C. and Limbird,L.E. (1997). Disruption of microtubules reveals two independent apical targeting mechanisms for G-protein-coupled receptors in polarized renal epithelial cells. *J Biol. Chem.* 272, 19035-19045.

Saxton,W.M., Stemple,D.L., Leslie,R.J., Salmon,E.D., Zavortink,M., and McIntosh,J.R. (1984). Tubulin dynamics in cultured mammalian cells. *J. Cell Biol.* 99, 2175-2186.

Schekman,R. and Orci,L. (1996). Coat proteins and vesicle budding. *Science* 271, 1526-1533.

Schmoranzer,J., Goulian,M., Axelrod,D., and Simon,S.M. (2000). Imaging constitutive exocytosis with total internal reflection fluorescence microscopy. *J. Cell Biol.* 149, 23-32.

Schulze,E. and Kirschner,M. (1986). Microtubule dynamics in interphase cells. *J. Cell Biol.* 102, 1020-1031.

Setou,M., Nakagawa,T., Seog,D.H., and Hirokawa,N. (2000). Kinesin superfamily motor protein KIF17 and mLin-10 in NMDA receptor- containing vesicle transport. *Science* 288, 1796-1802.

Siegel,D.P. (1999). The modified stalk mechanism of lamellar/inverted phase transitions and its implications for membrane fusion. *Biophys. J.* 76, 291-313.

Simons,K. and Wandering-Ness,A. (1990). Polarized sorting in epithelia. *Cell* 62, 207-210.

Solsona,C., Innocenti,B., and Fernandez,J.M. (1998). Regulation of exocytotic fusion by cell inflation. *Biophys. J.* 74, 1061-1073.

Sonnichsen,B., De Renzis,S., Nielsen,E., Rietdorf,J., and Zerial,M. (2000). Distinct membrane domains on endosomes in the recycling pathway visualized by multicolor imaging of Rab4, Rab5, and Rab11. *J Cell Biol* 149, 901-14.

Spruce,A.E., Breckenridge,L.J., Lee,A.K., and Almers,W. (1990). Properties of the fusion pore that forms during exocytosis of a mast cell secretory vesicle. *Neuron* 4, 643-654.

- Stephens,D.J. and Pepperkok,R. (2001). Illuminating the secretory pathway: when do we need vesicles? *J. Cell Sci.* *114*, 1053-1059.
- Steyer,J.A. and Almers,W. (1999). Tracking single secretory granules in live chromaffin cells by evanescent-field fluorescence microscopy. *Biophys. J.* *76*, 2262-2271.
- Steyer,J.A. and Almers,W. (2001). A real-time view of life within 100 nm of the plasma membrane. *Nat. Rev. Mol. Cell Biol.* *2*, 268-275.
- Steyer,J.A., Horstmann,H., and Almers,W. (1997). Transport, docking and exocytosis of single secretory granules in live chromaffin cells. *Nature* *388*, 474-478.
- Stoorvogel,W., Oorschot,V., and Geuze,H.J. (1996). A novel class of clathrin-coated vesicles budding from endosomes. *J Cell Biol* *132*, 21-33.
- Subtil,A., Gaidarov,I., Kobylarz,K., Lampson,M.A., Keen,J.H., and McGraw,T.E. (1999). Acute cholesterol depletion inhibits clathrin-coated pit budding. *Proc. Natl. Acad. Sci. U. S. A.* *96*, 6775-6780.
- Sumitani,S., Ramlal,T., Somwar,R., Keller,S.R., and Klip,A. (1997). Insulin regulation and selective segregation with glucose transporter-4 of the membrane aminopeptidase vp165 in rat skeletal muscle cells. *Endocrinology* *138*, 1029-34.
- Sund,S.E. and Axelrod,D. (2000). Actin dynamics at the living cell submembrane imaged by total internal reflection fluorescence photobleaching [In Process Citation]. *Biophys. J.* *79*, 1655-1669.
- Sund,S.E., Swanson,J.A., and Axelrod,D. (1999). Cell membrane orientation visualized by polarized total internal reflection fluorescence. *Biophys. J.* *77*, 2266-2283.
- Terakawa,S., Sakurai,T., and Abe,K. (1997). Development of an objective lens with a high numerical aperture for light microscopy. *Bioimages* *5*, 24.
- Thompson,N.L. and Lagerholm,B.C. (1997). Total internal reflection fluorescence: applications in cellular biophysics. *Current Opinion in Biotechnology* *8*, 58-64.
- Toomre,D., Keller,P., White,J., Olivo,J.C., and Simons,K. (1999). Dual-color visualization of trans-Golgi network to plasma membrane traffic along microtubules in living cells. *J. Cell Sci.* *112 (Pt 1)*, 21-33.
- Toomre,D., Steyer,J.A., Keller,P., Almers,W., and Simons,K. (2000). Fusion of constitutive membrane traffic with the cell surface observed by evanescent wave microscopy. *J. Cell Biol.* *149*, 33-40.
- Trinczek,B., Ebner,A., Mandelkow,E.M., and Mandelkow,E. (1999). Tau regulates the attachment/detachment but not the speed of motors in microtubule-dependent transport of single vesicles and organelles. *J. Cell Sci.* *112 (Pt 14)*, 2355-2367.
- Tsien,R.Y. (1998). The green fluorescent protein. *Annu Rev Biochem* *67*, 509-544.
- Tsuboi,T., Zhao,C., Terakawa,S., and Rutter,G.A. (2000). Simultaneous evanescent wave imaging of insulin vesicle membrane and cargo during a single exocytotic event. *Curr. Biol.* *10*, 1307-1310.
- Vega,I.E. and Hsu,S.C. (2001). The exocyst complex associates with microtubules to mediate vesicle targeting and neurite outgrowth. *J. Neurosci.* *21*, 3839-3848.

- Wacker,I., Kaether,C., Kromer,A., Migala,A., Almers,W., and Gerdes,H.H. (1997). Microtubule-dependent transport of secretory vesicles visualized in real time with a GFP-tagged secretory protein. *J. Cell Sci.* 110 (Pt 13), 1453-1463.
- Wang,E., Brown,P.S., Aroeti,B., Chapin,S.J., Mostov,K.E., and Dunn,K.W. (2000). Apical and basolateral endocytic pathways of MDCK cells meet in acidic common endosomes distinct from a nearly-neutral apical recycling endosome. *Traffic* 1, 480-493.
- Wang,M.D. and Axelrod,D. (1994). Time-lapse total internal reflection fluorescence video of acetylcholine receptor cluster formation on myotubes. *Developmental Dynamics* 201, 29-40.
- Ward,D.T., Hammond,T.G., and Harris,H.W. (1999). Modulation of vasopressin-elicited water transport by trafficking of aquaporin2-containing vesicles. *Annu Rev Physiol* 61, 683-97.
- Waters,M.G. and Pfeffer,S.R. (1999). Membrane tethering in intracellular transport. *Curr. Opin. Cell Biol.* 11, 453-459.
- Wehland,J., Willingham,M.C., Gallo,M.G., and Pastan,I. (1982). The morphologic pathway of exocytosis of the vesicular stomatitis virus G protein in cultured fibroblasts. *Cell* 28, 831-841.
- Weis,R.M., Balakrishnan,K., Smith,B.A., and McConnell,H.M. (1982). Stimulation of fluorescence in a small contact region between rat basophil leukemia cells and planar lipid membrane targets by coherent evanescent radiation. *J Biol. Chem.* 257, 6440-6445.
- Whitney,J.A., Gomez,M., Sheff,D., Kreis,T.E., and Mellman,I. (1995). Cytoplasmic coat proteins involved in endosome function [see comments]. *Cell* 83, 703-713.
- Yang,J. and Holman,G.D. (1993). Comparison of GLUT4 and GLUT1 subcellular trafficking in basal and insulin-stimulated 3T3-L1 cells. *J Biol Chem* 268, 4600-3.
- Yoshimori,T., Keller,P., Roth,M.G., and Simons,K. (1996). Different biosynthetic transport routes to the plasma membrane in BHK and CHO cells. *J. Cell Biol.* 133, 247-256.
- Zakharenko,S. and Popov,S. (1998). Dynamics of axonal microtubules regulate the topology of new membrane insertion into the growing neurites. *J. Cell Biol.* 143, 1077-1086.
- Zhang,F., Crise,B., Su,B., Hou,Y., Rose,J.K., Bothwell,A., and Jacobson,K. (1991). Lateral diffusion of membrane-spanning and glycosylphosphatidylinositol- linked proteins: Towards establishing rules governing the lateral mobility of membrane proteins. *J. Cell Biol.* 115, 75-84.
- Zhou,Z. and Mislser,S. (1995). Amperometric detection of stimulus-induced quantal release of catecholamines from cultured superior cervical ganglion neurons. *Proc. Natl. Acad. Sci. U. S. A.* 92, 6938-6942.
- Zimmerberg,J., Blumenthal,R., Sarkar,D.P., Curran,M., and Morris,S.J. (1994). Restricted movement of lipid and aqueous dyes through pores formed by influenza hemagglutinin during cell fusion. *J. Cell Biol.* 127, 1885-1894.
- Zimmerberg,J., Curran,M., Cohen,F.S., and Brodwick,M. (1987). Simultaneous electrical and optical measurements show that membrane fusion precedes secretory granule swelling during exocytosis of beige mouse mast cells. *Proc. Natl. Acad. Sci. USA* 84, 1585-1589.

13. Appendix

13.1. Curriculum Vitae

Name: Jan Schmoranzer
Address: 500 E 63rd, Apt. 20C
New York, NY 10021
Phone: (212) 421-0853 (home)
(212) 327-8150 (work)
E-mail: schmorj@rockefeller.edu

Education

Apr. 3, 1969 Born in Berlin (West), Germany

Jun. 1988 Highschool degree 'Abitur' at 'Staatliches Gymnasium am Rittersberg', Kaiserslautern, Germany

Aug. '88 – Oct. '89 Military service in Germany (obligatory)

Mar. '95 Degree of 'Diplom' in Physics at 'Rheinisch Westphälisch Technische Hochschule Aachen', Aachen, Gemany

June '95 – present Appointment as "Guest Investigator" and "Visiting Student" at the Laboratory of Cellular Biophysics, Rockefeller University, New York

2002 Prospective Graduation to Ph.D (Dr. rer. nat.),
"Fachbereich für Biologie, Chemie und Pharmazie", Freie Universität Berlin
(Department of Biology, Chemistry and Pharmacology), Free University, Berlin, Germany

Publications

Biology (Rockefeller University, NY)

- 1. Imaging Constitutive Exocytosis with Total Internal Reflection Fluorescence Microscopy**
Jan Schmoranzer, Mark Goulian, Dan Axelrod, Sanford M. Simon
J. Cell Biology 149(1):23-31, April 3, 2000
- 2. Insulin-regulated Release from the Endosomal Recycling Compartment is Regulated by Budding of Specialized Vesicles**

Michael A. Lampson, Jan Schmoranzer, Anja Zeigerer, Sanford M. Simon, and Timothy E. McGraw
Molecular Biology of the Cell, 12(11):3489-501, Nov. 2001

3. Role of Microtubules in Delivery and Fusion of post-Golgi Transport Intermediates

Jan Schmoranzer, Geri Kreitzer, Sanford M. Simon
Submitted to Journal of Cell Biology

4. Targeted Exocytosis of Apical Proteins and Distribution Syntaxin 3 in Polarized Epithelial Cells Depend on Microtubules

Geri Kreitzer, Jan Schmoranzer, Yunbo Gan, Seng Hui Low, Zhizhou Zhang, Thomas Weimbs, Sanford M Simon and Enrique Rodriguez-Boulan
In preparation

Physics – Material/Semiconductor Science (at RWTH, Aachen, Germany)

1. Homogeneity of ZnSSe/ZnSe multiquantum wells grown by metalorganic vapour phase epitaxy
J. Soellner, M. Scholl, J. Schmoranzer, A. Wahid, M. Heuken, J. Woitok, J. Hermans, W. Schiffers, J. Geurts., J. Crystal Growth 145 (1-4): 609-615 DEC 1994
2. ZnMgSSe/ZnSSe/ZnSe-heterostructures grown by metalorganic vapour phase epitaxy
J. Soellner, J. Schmoranzer, H. Hamadeh, B. Bollig, E. Kubalek, M. Heuken
Journal of Electronic Materials 24(11): 1557-1561 Nov 1995
3. Low-pressure metal-organic-vapor-phase-epitaxy (MOVPE) of ZnSSe with different precursors
J. Soellner, J. Schmoranzer, A. Wahid, H. Hamadeh, M. Heuken, Materials Science Forum Vols. 182-184 (1995) 419-422, 1995 Trans Tech Publications, Switzerland
4. Quantum yield of band-edge emission between 77 and 300 K of undoped and nitrogen doped ZnSe epilayers grown by MOVPE
A. L. Gurskii, A. N. Gavrilenko, E. V. Lutsenko, G. P. Yablonskii, W. Taudt, B. Wachtendorf, J. Soellner, J. Schmoranzer, M. Heuken,
Materials Science Forum Vols. 182-184 (1995) 243-245
1995 Trans Tech Publications, Switzerland
5. Characterization of $Zn(1-y)Mg(y)S(x)Se(1-x)$ epilayers grown by low-pressure metalorganic vapour phase epitaxy
H. Hamadeh, J. Soellner, J. Schmoranzer, M. Heuken
J. Crystal Growth 158(1-2):89-96 Jan 1996

13.2. Acknowledgements

Many people helped and supported me over the last six years at Rockefeller University. As it is impossible to thank all of them directly, I would like to express my gratitude to all those who made my scientific life at Rockefeller University not only possible, but also enjoyable.

Personally, I would like to thank Dr. Günter Blobel, who initially, by giving me the opportunity to join Rockefeller University as a guest investigator, helped further my career. His enthusiasm for scientific research encouraged me to make the step from Germany to the United States. Especially, he encouraged me - being a pure physicist who was interested in biology at this time - to join a complete new (biological) lab environment.

Many thanks to my advisor Dr. Sanford M. Simon who, by employing me in his lab at Rockefeller University as a guest investigator, gave me the chance to pursue high-level research in an excellently funded environment over many years. His creative and unconventional way of approaching scientific questions was a great source of inspiration and played an important role in the development of my personal way of thinking about scientific problems.

I would like to thank Prof. Dr. Ralf Erdmann for showing interest in my work and spending his time for the evaluation.

Over the last years, the Simon lab developed towards a high-end microscopy laboratory. This was possible because of both the excellent financial funding and the growing technical expertise in the lab. As core of this technical expertise I would like to thank Mark Goulian, Yu Chen and Nihal Altan for many fruitful discussions about the stepwise development of functional microscopy equipment. Further, I would like to thank all current/former members of the Simon lab for their support during the last years. Especially, I would like to thank:

Natalie de Souza, who is largely responsible for my scientific integration into the new 'biological' environment.

Mark Goulian, a former post-doctoral fellow, was not only a constant source of scientific advice to me. His enthusiasm for research in general was inspiring and sometimes a crucial source of motivation to "go on and do it". In addition, as a theoretical physicist who went straight into Biology, he was a great source of mathematical tools, which we used for quantitative video analysis.

I would like to thank Doris Peter, a former post-doctoral fellow of Simon lab, both personally and scientifically. She added significant experience to the young lab and proved to be more than helpful in many ways.

Yu Chen deserves a special thanks, mainly for offering his technical expertise. He wrote image acquisition software for the whole lab and solved innumerable computer problems.

Dan Axelrod, as one of the pioneers in the application of TIR to biology, was very encouraging while we were deciding whether to start doing TIR-FM

ourselves. The initial pilot project, showing that it was feasible to detect constitutive exocytosis with TIR-FM was performed in his laboratory. Many thanks for that. In addition, he was an excellent source of technical information as well as an inspiring discussion partner.

Many people in Dr. Libchaber's Biophysics lab at RU, especially Gregoire Bonnet, Didier Chatenay, Jun Zhang, Olek Krichevsky, Roy Bar-Ziv, Benoit Dubertret, GV Shivashankar and others, were a reliable source of technical information about tools and equipment needed for microscopy. Thanks to all of them.

It was great fun working with Geri Kreitzer, a post-doctoral fellow in E. Rodriguez-Boulan lab (Cornell), and Mike Lampson, currently a senior graduate student in McGraw lab (Cornell) on joint projects. We shared many exciting as well as frustrating hours in front of the 'scope, trying to catch "events" in live cells. I thank both Geri and Mike for their endurance and their professional as well as positive attitude.

I would like to thank Stefan Hoth, Mathias Zeidler and Daniel Besser for last minute corrections on the manuscript.

On the more personal level, I would like to thank the people who 'equipped' me with the genetic 'capabilities' to pursue academic studies, my dear parents, Vera and Hans Schmoranzler. They personify the strong and steady "homebase", which I think has been necessary for a healthy personal development. Both of them, having gone through academic education themselves, encouraged me to devote most of my time to higher education. Also, they were a great support during times of doubt about this choice.

It is extremely hard, if not impossible, to find the right words of gratitude for someone who is actually an integral part of ones life. My dear friend, Natalie de Souza, was many things to me during the period of this work. Over the years she was not only a reliable scientific "soundingboard", always ready to analyze and troubleshoot problems, but also taught me many practical as well as theoretical aspects of biology. And, most importantly, she was a great source of confidence and motivation during the tougher periods of this work. Lastly, she applied her brilliant editorial skills to my thesis, surely a reason why it sounds more "English" than "Gerglish".

I would like to thank W. A. Mozart and Kruder&Dorfmeister, whose acoustic spirit made endless analysis sessions on the computer more enjoyable.

13.3. Photo of multi-color TIR-FM system

